UNIVERSIDADE FEDERAL DO CEARÁ

CENTRO DE TECNOLOGIA

DEPARTAMENTO DE ENGENHARIA METALÚRGICA E DE MATERIAIS

PROGRAMA DE PÓS-GRADUAÇÃO EM ENGENHARIA E CIÊNCIA DE MATERIAIS

MATEUS ANDRADE DE SOUSA COSTA

THERMOMECHANICAL MODELING AND SIMULATION OF AN ELECTRIC ARC WELDING PROCESS: A COMPUTATIONAL ANALYSIS OF THE INFLUENCE OF THE ELEMENT BIRTH AND DEATH TECHNIQUE

FORTALEZA

2025

MATEUS ANDRADE DE SOUSA COSTA

THERMOMECHANICAL MODELING AND SIMULATION OF AN ELECTRIC ARC WELDING PROCESS: A COMPUTATIONAL ANALYSIS OF THE INFLUENCE OF THE ELEMENT BIRTH AND DEATH TECHNIQUE

Dissertation submitted to the Programa de Pós-Graduação em Engenharia e Ciência de Materiais, do Departamento de Engenharia de Materiais e Metalúrgica of the Universidade Federal do Ceará, as a partial requirement for obtaining the title of Master in Materials Science and Engineering. Concentration area: Transformation and Degradation Processes of Materials.

Advisor: Prof. Dr. Francisco Marcondes

Co-advisor: Prof. Dr. Yuri Cruz da Silva

FORTALEZA
2025

Dados Internacionais de Catalogação na Publicação
Universidade Federal do Ceará
Sistema de Bibliotecas
Gerada automaticamente pelo módulo Catalog, mediante os dados fornecidos pelo(a) autor(a)

C874t Costa, Mateus Andrade de Sousa.
Thermomechanical modeling and simulation of an electric arc welding process: a computational analysis of the influence of the element birth and death technique / Mateus Andrade de Sousa Costa. – 2025.
105 f. : il. color.

Dissertação (mestrado) – Universidade Federal do Ceará, 1, Fortaleza, 2025.
Orientação: Prof. Dr. Francisco Marcondes.
Coorientação: Prof. Dr. Yuri Cruz da Silva.

1. Arc Welding. 2. Thermomechanical Simulation. 3. Finite Element Method. 4. Residual Stresses. 5. Element Birth and Death Technique. I. Título.

CDD

MATEUS ANDRADE DE SOUSA COSTA

THERMOMECHANICAL MODELING AND SIMULATION OF AN ELECTRIC ARC WELDING PROCESS: A COMPUTATIONAL ANALYSIS OF THE INFLUENCE OF THE ELEMENT BIRTH AND DEATH TECHNIQUE

Dissertation submitted to the Programa de Pós-Graduação em Engenharia e Ciência de Materiais, do Departamento de Engenharia de Materiais e Metalúrgica of the Universidade Federal do Ceará, as a partial requirement for obtaining the title of Master in Materials Science and Engineering. Concentration area: Transformation and Degradation Processes of Materials.

Advisor: Prof. Dr. Francisco Marcondes

Co-advisor: Prof. Dr. Yuri Cruz da Silva

Approved on: January 27, 2025.

EXAMINING BOARD

_____
Prof. Dr. Francisco Marcondes (Advisor)
Universidade Federal do Ceará (UFC)

_____
Prof. Dr. Yuri Cruz da Silva (Co-advisor)
Instituto Federal de Educação, Ciência e Tecnologia do Ceará (IFCE)

_____
Prof. Dr. Emerson Mendonça Miná
Universidade Federal do Ceará (UFC)

_____
Prof. Dr. Willys Machado Aguiar
Instituto Federal de Educação, Ciência e Tecnologia do Ceará (IFCE)

To God.

To my parents, Antonio e Lucirene.

ACKNOWLEDGMENTS

I would like to express my heartfelt gratitude to my family, especially my parents, Antonio and Lucirene, for their unwavering support throughout my years at the Federal University of Ceará. Their guidance and wise advice have been invaluable in helping me succeed in every step of my journey.

I am deeply grateful to all the professors who taught me during the two years of the Master's Program in Engineering and Material Science. I truly appreciate their dedication and effort in imparting essential knowledge to us. Among them, I would like to extend my special thanks to my advisor, Francisco Marcondes, and my co-advisor, Yuri Cruz. Their expertise, guidance, and insightful feedback were pivotal to the development of this study. I particularly acknowledge their invaluable contributions, from their helpful suggestions and reviews to their unwavering support throughout the process of completing this dissertation. I also want to thank the committee members for their willingness to be part of this work and for their time and valuable input.

A special thanks goes to my classmates and friends, whose companionship and shared experiences made this challenging journey enjoyable and enriching. I am particularly grateful for the advice, feedback, and meaningful discussions shared with my colleagues at the Computational Fluid Dynamics Laboratory (LDFC). My deepest appreciation goes to Ivens, whose early guidance significantly contributed to the successful completion of this research.

To everyone who supported me along the way, thank you for your encouragement and inspiration.

"*Technology is nothing. What's important is that you have a faith in people, that they're basically good and smart, and if you give them tools, they'll do wonderful things with them*".

Steve Jobs

RESUMO

A soldagem a arco desempenha um papel crucial na indústria moderna, especialmente na fabricação de estruturas e componentes complexos. Embora o processo seja amplamente utilizado e relativamente simples, não está isento de desafios. A soldagem pode introduzir tensões residuais, distorções e defeitos no material, comprometendo potencialmente a integridade estrutural, aumentando custos e exigindo retrabalho. Para enfrentar esses desafios, este estudo realiza uma análise termomecânica detalhada do processo de soldagem, explorando a modelagem computacional como alternativa viável aos métodos experimentais tradicionais. A pesquisa utiliza o software ANSYS® e o Método dos Elementos Finitos (MEF) para simular o comportamento térmico e mecânico de materiais sob condições específicas de soldagem. O estudo concentra-se na soldagem de topo de passe único em chapas e tubos, incorporando metais de adição e utilizando a Técnica de Elemento Vivo Morto (TEVM) para simular a adição de material durante a soldagem. Ao examinar diferentes ordens de elementos de malha (lineares e quadráticos), a análise avalia distribuições de temperatura, tensões residuais e deformações, considerando também a eficiência computacional. Os resultados revelaram que a TEVM aumentou a duração total do teste em 16,5%, com uma diferença significativa de temperatura (665ºC com TEVM vs. 348ºC sem TEVM) durante a passagem da fonte de calor. A ordem dos elementos de malha influenciou consideravelmente os resultados: elementos quadráticos reduziram o número de elementos em 85%, equilibrando precisão e eficiência computacional, enquanto elementos lineares refinados aumentaram o tempo de execução em até 90%. Para a zona afetada pelo calor (ZAC), simulações sem TEVM podem ser suficientes, mas a análise do cordão de solda exige validação adicional, especialmente em soldagem multipasse, onde o reaquecimento altera as distribuições de tensões. A metodologia foi validada por meio de comparações com dados analíticos, numéricos e experimentais disponíveis na literatura, confirmando sua robustez para análise estrutural e otimização de processos. Esta pesquisa contribui para o entendimento teórico da soldagem a arco, oferecendo um arcabouço computacional que equilibra eficazmente precisão e custo. O estudo estabelece uma base sólida para investigações futuras, sobretudo na exploração das complexidades da soldagem multipasse.

Palavras-chave: soldagem a arco; simulação termomecânica; método de elementos finitos; tensões residuais; técnica de elemento vivo morto.

ABSTRACT

Arc welding plays a vital role in modern industry, particularly in the fabrication of complex structures and components. While the process is widely employed and relatively straightforward, it is not without challenges. Welding can introduce residual stresses, distortions, and defects into the material, potentially compromising structural integrity, increasing costs, and necessitating rework. To address these challenges, this study conducts a detailed thermomechanical analysis of the welding process, exploring computational modeling as a viable alternative to traditional experimental methods. The research employs ANSYS® software and the Finite Element Method (FEM) to simulate the thermal and mechanical behavior of materials under specific welding conditions. The study focuses on single-pass butt welding of plates and pipes, incorporating filler metals and utilizing the Element Birth and Death Technique (EBDT) to simulate material addition during welding. By examining different mesh element orders (linear and quadratic), the analysis evaluates temperature distributions, residual stresses, and deformations while also considering computational efficiency. The results revealed that EBDT increased test duration by 16.5%, and a significantly temperature difference (665ºC with EBDT vs. 348ºC without) during heat source passage. Mesh element order notably influenced outcomes: quadratic elements reduced the element count by 85%, balancing accuracy and computational efficiency, while refined linear elements increased execution time by up to 90%. For the heat-affected zone (HAZ), simulations without EBDT may suffice, but weld bead analysis requires further validation, particularly in multi-pass welding, where reheating alters stress distributions. The methodology was validated through comparisons with analytical, numerical, and experimental data available in the literature, confirming its robustness for structural analysis and process optimization. This research contributes to the theoretical understanding of arc welding, offering a computational framework that effectively balances precision and cost. The study lays a strong foundation for future investigations, especially in exploring the complexities of multi-pass welding.

Keywords: arc welding; thermomechanical simulation; finite element method; residual stresses; element birth and death technique.

LIST OF FIGURES

LIST OF TABLES

LIST OF ABBREVIATIONS AND ACRONYMS

APDL	Ansys Parametric Design Language
EBDT	Element Birth and Death Technique
EbFVM	Element based Finite Volume Method
FEM	Finite Element Method
MAG	Metal Active Gas
MIG	Metal Inert Gas
GMAW	Gas Metal Arc Welding
GTAW	Gas Tungsten Arc Welding
HAZ	Heat-affected zone
PAW	Plasma Arc Welding
TIG	Tungsten Inert Gas
SAW	Submerged Arc Welding
SMAW	Shielded Metal Arc Welding
TEVM	Técnica de Elemento Vivo Morto

LIST OF SYMBOLS

T	Temperature
C	Carbon
Mn	Manganese
Si	Silicon
Cr	Chromium
Cu	Copper
k	Thermal conductivity of the material
ρ	Density
c	Coefficient of specific heat
q	Heat source power
T_0	Initial temperature
η	Yield
α	Thermal diffusivity
P	Power
Q	Heat source intensity
W	Watt
ºC	Celsius
®	Trademark
mm	Milimeter
s	Second
%	Percentage

CONTENTS

1 INTRODUCTION

Arc welding is one of the most fundamental and widely utilized processes in modern industry, playing a crucial role in the fabrication of highly complex structures and components. It is employed in various applications, such as onshore and offshore oil production platforms, aircraft, nuclear reactors, and other processes. Consequently, the effective understanding and control of the thermomechanical phenomena involved in this process are essential to ensure the structural integrity and quality of the produced joints.

Over time, the welding process has diversified to encompass specific applications. From the use of shielded metal arc welding, which relies on a consumable electrode to join two pieces, to processes such as TIG (Tungsten Inert Gas), which can also utilize the heat generated by the electric arc without requiring a consumable electrode, various methods have been developed to optimize cost-effectiveness. However, each process has its own specific characteristics and challenges to overcome. In fusion welding, due to localized heating and cooling, residual stresses and distortions are induced in the welded component (Ganesh et al., 2014).

Modenesi (2012) observed that, although welding is a straightforward process, it is important to recognize that it can cause damage to the material due to the application of a large amount of energy in a small area, resulting in significant alterations to the structure and properties near the weld region. The issue of distortions induced by the welding process during large steel fabrications is always a major concern in such operations, as it leads to dimensional inaccuracies and potential structural problems, which may result in costly expenses and rework in the production process (Chen et al., 2011).

Based on the potential issues encountered during the welding process, efforts have been directed toward analyzing these impacts, leading to the development of new investigative methods over time. In this context, thermomechanical modeling and simulation emerge as indispensable tools for analyzing the physical behavior of materials during arc welding, enabling the precise prediction of critical parameters and the optimization of the process.

The intrinsic complexity of the interaction between the heat generated by the electric arc, heat fluxes, and the deformations of the materials during welding requires advanced approaches for analysis. In this regard, computational modeling and numerical simulation have played a pivotal role, offering a virtual platform to investigate thermomechanical phenomena at both micro and macro scales. The application of these

techniques not only allows for the prediction of temperature and stress distributions but also facilitates an in-depth understanding of the underlying physical mechanisms governing the process.

Furthermore, computational simulations also enable the prediction of the material deposition process over time, bringing the simulation closer to the real process.

In this context, the present study proposes an integrated approach to thermomechanical modeling and simulation applied to an arc welding process. The main objective is to provide a detailed analysis of the thermomechanical interactions in different regions of the material, considering factors such as the geometry of the analyzed piece (e.g., plate or pipe), the material's physical properties, welding operation parameters, among other aspects. Additionally, the study aims to evaluate the impact of welding conditions based on the obtained numerical results and the formation of possible defects, residual stresses, and deformations.

This research seeks to perform a comparative analysis with existing numerical methods in the literature, utilizing computational simulation software. The integration of computational modeling and numerical simulation techniques provides an opportunity to explore a wide range of operational scenarios, enabling the identification of optimal conditions for producing high-quality, high-performance weld joints.

Through this study, the goal is not only to contribute to the advancement of theoretical knowledge in the field of arc welding but also to provide guidelines and an alternative methodology to traditional analyses based on experimental methods. The results of the simulations aim to offer similar efficacy for the thermomechanical study of welding within academia.

1.1 Objectives

1.1.1 General objective

The present study aims to analyze the phenomena involved in the welding process using the computational tool ANSYS to perform a thermomechanical simulation of the welding joint and the material's behavior around the heat-affected zone. This is achieved by incorporating its physical and mechanical properties, as well as the welding parameters associated with the process. The study also aims to assess the impact of computational techniques, such as the Element Birth and Death Technique (EBDT) and varying mesh element orders, on the accuracy and efficiency of simulations. The obtained data are validated against analytical, numerical, and experimental analyses from the literature. Through this approach, the simulation predicts temperature profiles, residual stresses, and displacements, providing insights into material behavior, residual stress distribution, and distortions post-process.

1.1.2 Specific objectives

- Determine the temperature gradient resulting from the welding process in metallic plates and tubes, considering an ellipsoidal heat source with parameters adjusted to the process conditions;
- Analyze the residual stresses and mechanical deformations generated from the obtained thermal data, evaluating the impact of the thermal gradient on the structural results of the material;
- Investigate the effect of the Element Birth and Death Technique (EBDT) on the welding process by simulating the progressive addition of material to the weld bead and assessing its influence on the stress and deformation results;
- Compare the effects of linear and quadratic mesh element orders in thermal and mechanical analyses, evaluating their contributions to results and computational efficiency;
- Evaluate the thermal distribution and residual stress profiles along the longitudinal walls of the tube during the welding process, with a focus on the heat-affected zone (HAZ).

2 LITERATURE REVIEW

2.1 Welding process

Welding is a vital process in the manufacturing and assembly of structures and products across various industries. Essentially, it is a technique for joining materials, predominantly metals and thermoplastics, through the application of heat, pressure, or both. According to Tesfaye and Getaneh (2023), welding is the process of combining two or more metals, either similar or dissimilar, by heating them to an appropriate temperature and then joining them with or without the use of pressure, filler material, and flux. The heat required for this process can be supplied by an electric arc (in arc welding), gas combustion (in gas welding), electrical resistance (in resistance welding), or forge fire (in forge welding).

Among the types of operations mentioned by the authors, arc welding refers to a set of welding processes in which the electric arc generated by electrical energy melts both the electrode and the weld pool material, enabling the joining of workpieces. For example, in operations such as shielded metal arc welding (GMAW), Bracarense (2003) states that the welding arc is formed by the continuous feeding of filler metal and the weld pool. A schematic diagram of a TIG welding arc with filler metal deposition is shown in Figure 1 below, based on the work of Kalita et al (2022).

Figure 1 – Illustrative representation of the TIG welding process.

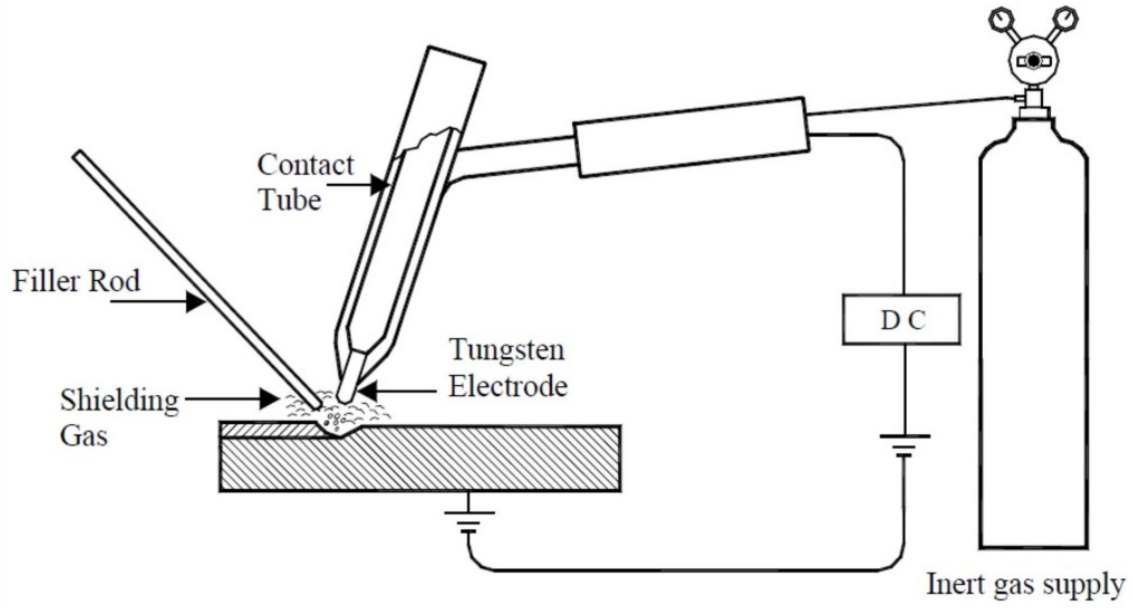

Source: Kalita et al (2022).

Furthermore, a representation of an arc welding process can also be visualized in Figure 2 below, based on the work of Wu et al. (2014), comparing autogenous TIG (Tungsten Inert Gas) welding and Plasma Arc Welding (PAW). The difference between autogenous TIG and PAW welding processes, when compared to GMAW, lies in the use of a non-consumable tungsten electrode and a shielding gas, such as argon. These processes rely on the fusion of the base metals to facilitate the filling of the weld pool.

Figure 2 - Representation of arc welding processes: autogenous TIG and plasma.

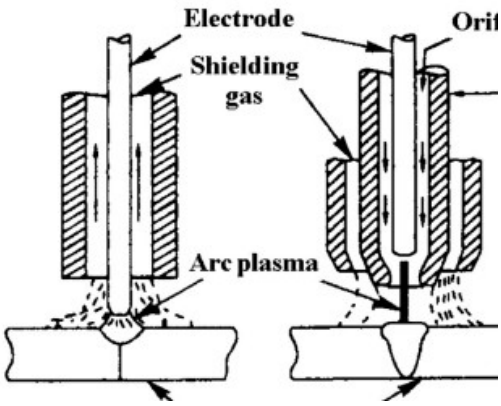

Source: Wu, et al. (2014).

2.1.1 Weld bead geometry

Thus, after initially understanding the primary welding methods, it is also important to mention the geometry involved in the welding process, which can be initially illustrated in the base metal region of Figure 2.

Chen (2011) states that, in the welding process, a liquid weld pool formed by intense heat melts and solidifies the substrates, eliminating the interface between them and creating a solid joint, while transformations in microstructure and properties occur both in the fusion zone and the heat-affected zone. Cho et al. (2014) also emphasize that a detailed understanding of temperature and fluid flow is essential for the successful application of welding processes, as they directly influence the dimensions of the weld pool, cooling rates, and, consequently, the microstructure and mechanical properties of the final weld. Kou (1985) mention that the dynamics of fluid flow in weld pools play a crucial role in determining weld quality, influencing factors such as penetration, undercutting, surface finish, segregation patterns, gas porosity, and solidification structure.

Panwisawas et al. (2018) support Cho et al. (2014) and mention that fusion welding modeling also requires a detailed understanding of the complex physical phenomena of the process, including phase changes such as melting and vaporization that occur during the interaction between the heat source and the workpieces, along with the resulting mechanical forces. Tümer et al. (2022) add that, to understand the impact of welding on the final part's properties, a detailed analysis of the material changes in the heat-affected zone (HAZ) and the weld metal are required.

The illustration of fusion welding, detailing the fusion zone, heat-affected zone (HAZ), and weld pool, as well as the heat source, can be clearly seen in Figure 3 below, from Cho (2011).

Figure 3 - Illustrative example of a fusion weld.

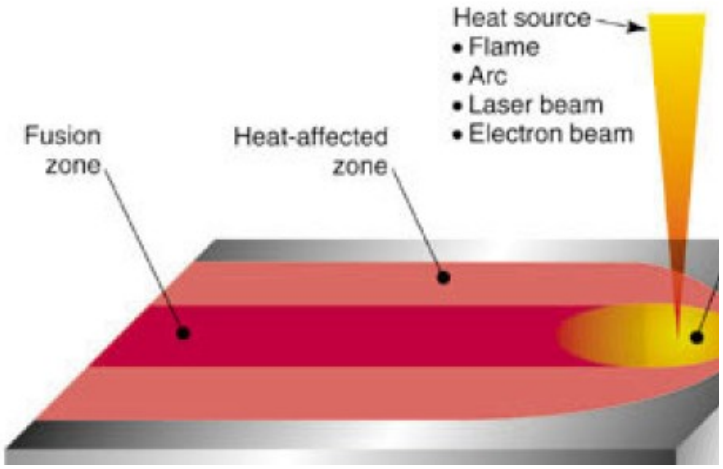

Source: Cho (2011).

In arc welding operations, whether or not filler metals are used, the behavior of the weld bead depends on the initial process parameters. According to DebRoy and David (1995), "the resulting heat and fluid flow affect the size and shape of the weld pool, as well as the cooling rate, kinetics, and extent of various solid-state transformation reactions in the fusion zone and heat-affected zone."

Additionally, Modenesi (2011) observed that the way metal is transferred during welding varies according to several factors, including the electrical characteristics of the arc, such as current, voltage, and polarity, as well as the size and type of filler metal, the nature of the shielding gas, and the length of the electrode. He illustrates this with an example in Figure 4, which shows the relationship between electric current and weld bead shape, where it can be seen that the depth increases and the width decreases as the intensity of the electrical source increases.

Figure 4 – Schematic relationship between the intensity of the electrical source and the weld bead shape.

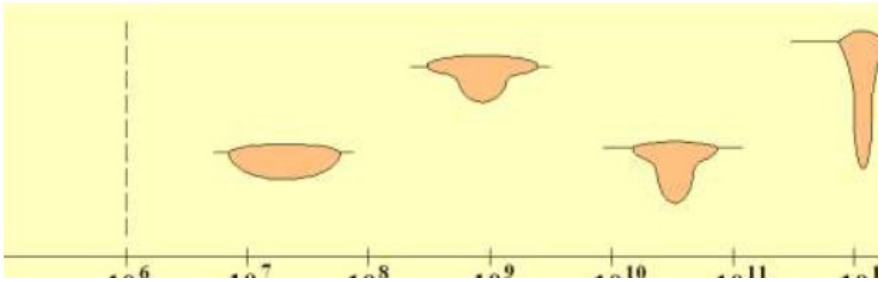

Source: Modenesi (2011)

2.1.2 Shielding gas in the welding process

Another important topic that should be mentioned, as it is a crucial part of the welding process, is the shielding gas used in the electric arc. Mvola and Kah (2017) report that the shielding gas in welding not only protects the molten droplet and the weld bead but also influences metal transfer, penetration, bead width, and spatter control, in addition to affecting the metallurgical and mechanical characteristics of the weld.

Kah and Martikainen (2013) also mention that oxygen, nitrogen, and water vapor present in the environment can contaminate the process, and thus, shielding gases prevent the harmful effects on the molten metal.

2.2 TIG welding process

TIG welding is one of the most important and popular welding manufacturing processes. Kumar et al. (2021) states that TIG welding is an arc welding method where the union of materials is made through the heat produced by an electric arc formed between a non-consumable tungsten electrode and the workpiece being welded. According to Olson et al. (1993), this welding process can be carried out with or without the use of a filler metal, and Jeyaprakash et al. (2015) mentions that if a filler metal is used, it is inserted by dipping the tip of a filler rod into the front edge of the molten weld pool.

Modenesi et al. (2000) commented that the area around the electric arc is protected by an inert gas or a combination of gases, and for the arc to work, the tungsten electrode is heated until it reaches a high temperature, which allows the release of the necessary electrons.

Regarding the use of shielding gas during the TIG welding process, Durtuglu (2003) reports that in TIG welding, the use of shielding gas is essential, and the choice of components in the gas mixture used in arc welding mainly depends on the material being welded.

In this regard, Schwedersky et al. (2011) investigated the impact of different shielding gases on the efficiency and quality of TIG welding and found that the use of argon-hydrogen mixtures allowed speeds comparable to the MIG/MAG process. The author shows that the addition of hydrogen, for example, often contributes to welding failures such as cracks and porosity, especially in the case of steel welding.

The TIG welding process has been studied with various base metals. Yan et al. (2010) conducted studies on microstructure and mechanical properties in AISI 304 stainless steels, comparing laser welding and hybrid laser-TIG welding. In this case, lower tensile strength and larger grain size were observed, as well as a transition zone and a heat-affected zone.

Karpagaraj et al. (2015) conducted similar studies on thin titanium sheets, varying different welding parameters such as current and speed. They found that increased heat input and decreased cooling rate led to higher hardness in the fusion zone, suggesting a finer and stronger microstructure.

Furthermore, Krishna et al. (2016) performed an analysis of TIG welding on Inconel 625 nickel-based alloy with varying parameters such as current, voltage, speed, and fusion efficiency using finite element analysis, which will be discussed in the next section. The authors were able to analyze the temperature distribution at different locations from the weld center and evaluate the extent of the heat-affected zone in function of welding parameter variations.

Thus, it can be observed that joining different materials has been a challenge in recent years, and many tests have been conducted, including computational aspects, which will be explored further, to obtain more precise data that reflect the practical situation.

2.3 Thermal and mechanical models

2.3.1 Thermal analysis and heat source models

One of the main challenges involved in simulating temperature fields of a welding process is the modeling of the heat source. Kik (2020) states that, prior to any attempt at

computational simulation of welding processes, the representation of temperature and stress fields during welding relies exclusively on analytical techniques.

Based on this, Rosenthal (1946) was one of the pioneering researchers in creating an analytical solution to understand heat transfer in the welding processes, on heat conduction. His work enabled the prediction of the weld pool shape in both two-dimensional and three-dimensional contexts. He utilized Fourier's partial differential equation for heat conduction and innovated by introducing a moving coordinate system. He developed solutions for both point and line heat sources. Rosenthal's (1946) work was fundamental in addressing challenges related to welding, as it allowed for the analysis of the process through parameters such as current, voltage, welding speed, and weld configuration.

Rocha (2022) mentions that the analytical solutions, in this case, are initially obtained from the heat conduction equation, Eq. 2.1:

$$\rho c \frac{dT}{dt} = k\nabla^2 T + q \tag{2.1}$$

in which T represents the temperature, k is the thermal conductivity of the material, ρ denotes the material density, c stands for the specific heat coefficient, and q represents the heat source generated by the electric arc.

Based on this equation, Rosenthal (1941) developed in his pioneering work an equation in a moving coordinate system for three-dimensional heat transfer domains, which is given by Eq. 2.2 below:

$$T = T_0 + \frac{P}{2\pi kR}\exp\left[-\frac{v}{2\alpha}(x+R)\right] \tag{2.2}$$

in which, T_0 denotes the initial temperature of the system, $P = \eta UI$ represents the net power supplied by the arc welding process, U stands for the voltage, I denotes the electric current, η is the process efficiency, v is the welding speed during the operation, α is the thermal diffusivity. Finally, $R = \sqrt{x^2 + y^2 + z^2}$ represents the distance from the heat source to the specific point of application.

Flint et al. (2017) mention that this method provided acceptable estimates for the temperature variation in areas further from the heat source; however, the predictions were less accurate near the fusion zone.

Building on the works published by Rosenthal, Friedman (1978) advanced the studies by considering the distortion of the weld pool due to the pressure of the welding arc and the gravitational forces on the pool. The goal was to evaluate the combined effects of heat flow in the workpiece and the changes in the shape of the pool on the weld penetration. Thus, the expression for the heat source obtained in the electric arc is applied as a Gaussian normal distribution function, which can be expressed by

$$q(r) = \left[\frac{3Q}{\pi r_h^{\,2}}\right] \exp\left[-3\left(\frac{r}{r_h}\right)^2\right] \tag{2.3}$$

where, *q(r)* is the heat flux acting on the surface, Q is the intensity of the source (obtained by the product of arc current, voltage drop, and arc efficiency), r is defined as the distance from the center of the weld,, and r_h is a dimensional parameter that defines the region where 95% of the arc heat is deposited. Figure 5 highlights the Gaussian distributed heat source, as illustrated in the work of Chen (2011).

Figure 5 – Gaussian distributed heat source.

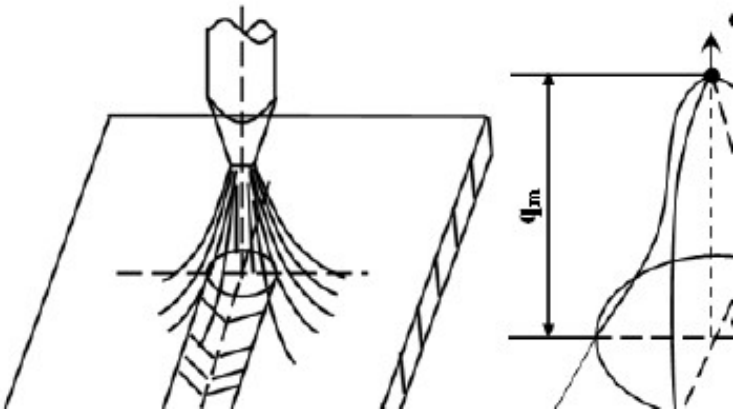

Source: Chen (2011)

Thus, new studies on heat sources were conducted with the objective of not only obtaining a volumetric distribution in the arc profile but also seeking a better representation of welding heat sources to reflect the reality of the process.

Through Goldak's work (1984), a mathematical model with a Gaussian distribution is proposed, but with the suggestion of a non-symmetric double ellipsoidal geometry, allowing simple adjustments in the size and shape of the heat source to enable the simulation of arc welding processes with surface penetration (such as SMAW and GTAW), as well as processes with deeper penetration, such as laser or electron beam welding.

Among Goldak's main contributions (1984), the semi-ellipsoidal heat source model which is given by

$$q(x,y,z) = q_{máx} \exp(-Ax^2 - By^2 - Cz^2) \tag{2.4}$$

and the double ellipsoidal distribution model, with distinct expressions for the heat source in the front and rear quadrants, given by Eq. 2.5 and Eq. 2.6

$$q_f(x,y,z) = \frac{6\sqrt{3}(f_f Q)}{abc_f \pi\sqrt{\pi}} \exp\left(-\frac{3x^2}{a^2} - \frac{3y^2}{b^2} - \frac{3z^2}{c_f{}^2}\right), x \geq 0 \tag{2.5}$$

$$q_r(x,y,z) = \frac{6\sqrt{3}(f_r Q)}{abc_r \pi\sqrt{\pi}} \exp\left(-\frac{3x^2}{a^2} - \frac{3y^2}{b^2} - \frac{3z^2}{c_r{}^2}\right), x \geq 0 \tag{2.6}$$

in which, in Equations 2.4, 2.5 and 2.6, a, b, c, c$_f$ and c$_r$ are the semi-axes of the ellipsoid in the x, y, z directions; and $q_{máx}$ is the maximum value of the heat flux at the center of this geometry. In Eq. 2.5, f_f and f_r are the fractions of the heat source deposited in the front and rear quadrants, where $f_f + f_r = 2$.

Thus, Flint et al. (2017) highlights that the methodology suggested by Goldak proved to be highly effective in representing the electric arc as a heat source, and due to its effectiveness, Farias et al. (2022) emphasizes that this method is currently the most widely used in welding simulations.

2.3.2 Thermal analysis using Finite Element Analysis (FEM)

In the context of welding simulation, Chen (2011) reports that the modeling of a moving heat source is characteristic of a transient process and that while this source moves, the amount of thermal energy it emits remains the same, but the position of the center where this energy is emitted changes over time, as can be seen in Figure 6 taken from Rocha (2022).

Figure 6 – Goldak's double-ellipsoidal model.

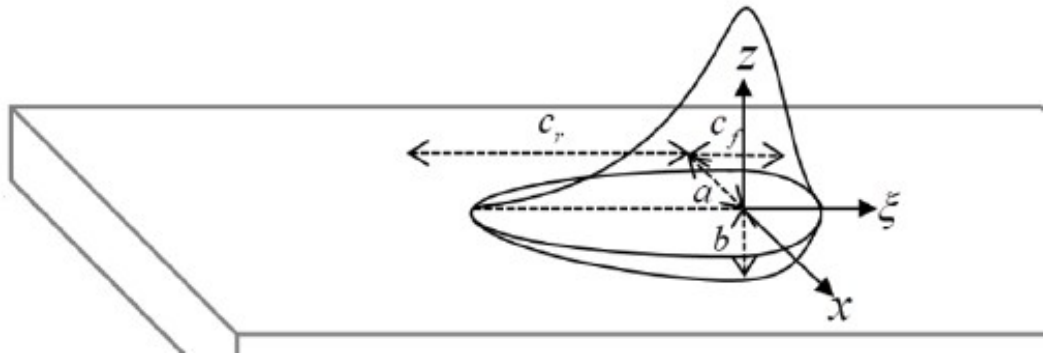

Source: Rocha (2022).

Initially, among the various traditional numerical solutions, Manurung et al. (2013) highlights the Finite Element Method (FEM) as the most widely used technique for modeling and analyzing welding processes, as it is recognized as an auxiliary tool to experimental techniques and understanding the behavior governing the process. Jiang et al. (2016) adds that this is an effective method for studying welding processes, and this type of simulation is extensively employed in computational simulations.

According to Moaveni (1999), the resolution of any finite element method involves the steps of preprocessing, solution, and postprocessing. Initially, in the preprocessing stage, the author details that this phase involves discretizing the problem domain into finite elements (nodes and elements), choosing a shape function that represents the physical behavior of the element, developing the equations for each element, and then assembling the elements to form the global stiffness matrix and applying the initial boundary conditions and loading. In the solution stage, the same author highlights the resolution of the linear or nonlinear system matrix to obtain results at the nodes, such as temperatures and displacements at different points in the model. Finally, in the postprocessing stage, additional

information is obtained, such as principal stresses, heat fluxes, or other variables of interest related to the problem being analyzed.

Thus, highlighting the welding process in a finite element analysis (FEM), Marques et al. (2020) describes that a simulation should be conducted through the following stages: 1) transient heat transfer simulation, thus obtaining the temperature data; 2) the temperature field obtained is inserted into the simulation, and a static mechanical analysis is performed; 3) this results in thermal expansion causing deformation; and 4) finally, when the temperature reaches the initial values, the residual stress field is obtained.

In the work of Vemanaboina et al. (2014), the author briefly explains that heat transfer equations, such as the one presented in Eq. 2.1, can be represented by the following system of equations presented in Eq. 2.7

$$\left[K(T)\right]\{T\}+[C(T)]\{T\}=\{Q(T)\} \tag{2.7}$$

in which K is the thermal conductivity matrix, C is the capacitance matrix, Q represents the heat source, and T is the temperature vector at each node of the mesh.

Vemanaboina et al. (2014) further emphasizes that Eq. 2.7 is solved through numerical methods using iterative models, such as Euler and Crank-Nicholson. In the work of Rocha (2022), the iterative Newton-Raphson method is used, which employs a residual vector R for iterative corrections i to increment the variable to be calculated, and A represents the coefficients matrix, according to Eq. 2.8:

$$A_{i+1}^{n+1}T_{i+1}^{n+1}-B_{i+1}^{n}=R_{i+1}^{n+1} \tag{2.8}$$

Among the studies conducted in the literature, Keivani et al. (2014) conducted a study using FEM with the aim of predicting the influence of welding sequences on the generation of residual stresses and distortions in T-joints, as shown in Figure 7. This study involved dividing the workpiece into small geometric elements known as a mesh and applying the steps described by Marques et al. (2020), thus obtaining acceptable results when compared to experimental measurements.

Figure 7 - T-joint with mesh pattern used in simulation and obtained residual stresses.

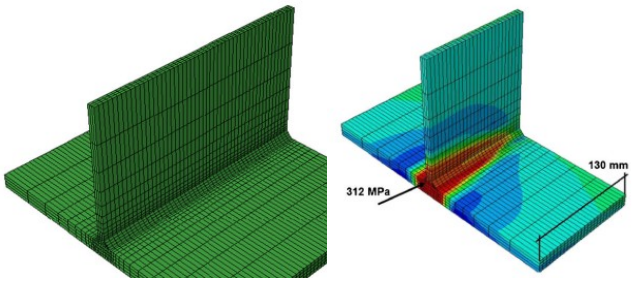

Source: Adapted from Keivani et al (2014)

Another example of a study is the one conducted by Nezamdost et al. (2016), which also performs an analysis of temperature and residual stresses in submerged arc welding (SAW) using Goldak's heat source in an APIX65 steel tube. The problem-solving method aligns with the works of Marques et al. (2020) and Keivani et al. (2014), and the results found in the model were also acceptable when compared to experimental measurements.

2.3.3 Mechanical analysis

In mechanical analysis, it is important to first understand how the relationship between the loads acting on a body and its deformation behaves. Thus, as shown in Figure 8, the stress-strain curve for a typical ductile material under tension can be observed.

Figure 8 – Conventional representation of the stress-strain behavior for ductile materials.

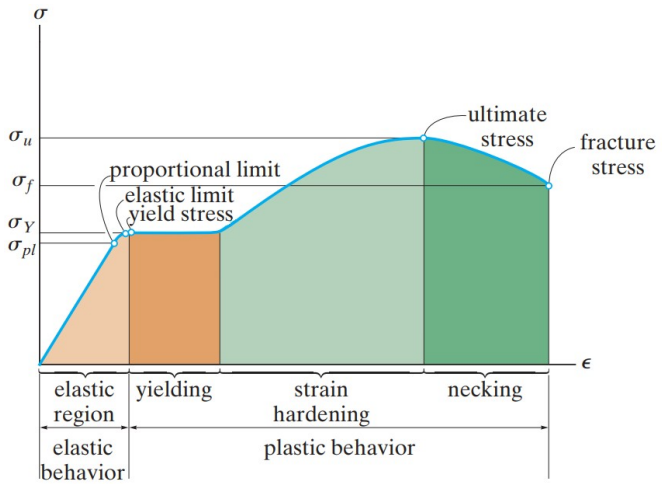

Source: Adapted from Hibbeler (2010, p. 84).

For the curve shown in Figure 8, the behavior of the uniaxial body can be observed initially through the elastic region and its elastic limit, which corresponds to the region where stress does not result in permanent deformation when the force is released from the body. Additionally, there is the proportional limit, which is the maximum point of proportionality between stress and strain. Beyond this, there is the yield stress, which, according to Kim (2015), is the stress required for a 0.2% plastic deformation to occur. In the strain hardening region, more stress is needed for material deformation until the body reaches the ultimate stress, or the maximum stress the material can withstand. Finally, the uniaxial body undergoes the necking process, where the cross-sectional area of the body is reduced during deformation until fracture occurs.

For mechanical testing, Kohnke (1999) presents the solution of the matrix for the linear system in mechanical tests through Eq. 2.9, involving stress and strain through Hooke's Law, relating each stress component through a linear combination of strain for elastic materials, according to the definition by Peric et al. (2011).

$$\sigma = E\,(\varepsilon - \varepsilon^{pl}) \tag{2.9}$$

in this context, σ describes the stress tensor, i.e., the stresses $[\sigma_x\ \sigma_y\ \sigma_z\ \sigma_{xy}\ \sigma_{yz}\ \sigma_{xz}]$, E is the Young's modulus of the material, later defined by [D] or stiffness matrix, $\{\varepsilon\}$ corresponds to the total strain vector, subtracted by the plastic strain vector., $\{\varepsilon^{pl}\}$.

Rocha (2022) details Eq. 2.9 in matrix form, considering an isotropic and elastic material, using the Voigt notation. The author explains that this notation treats the fourth-order tensor as pseudo-two-dimensional matrices and the second-order tensors as pseudo-vectors, as represented in Eq. 2.10 below:

$$\begin{bmatrix} \sigma xx \\ \sigma yy \\ \sigma zz \\ \sigma xy \\ \sigma yz \\ \sigma zx \end{bmatrix} = \begin{bmatrix} \lambda+2\mu & \lambda & \lambda & 0 & 0 & 0 \\ \lambda & \lambda+2\mu & \lambda & 0 & 0 & 0 \\ \lambda & \lambda & \lambda+2\mu & 0 & 0 & 0 \\ 0 & 0 & 0 & \mu & 0 & 0 \\ 0 & 0 & 0 & 0 & \mu & 0 \\ 0 & 0 & 0 & 0 & 0 & \mu \end{bmatrix} \begin{bmatrix} \varepsilon xx \\ \varepsilon yy \\ \varepsilon zz \\ 2\varepsilon xy \\ 2\varepsilon yz \\ 2\varepsilon zx \end{bmatrix} \quad (2.10)$$

where λ e μ are denoted as the Lamé constants, which are related to Young's modulus E and Poisson's ratio ν, both of which are contained in the stiffness matrix [D].

For nonlinear relationships between stress and strain, according to Kohnke (1999), the definition of elastic strain proposed in Eq. 2.9, complementing the definition by Peric et al. (2011), is expressed in the following form as shown in Eq. 2.11.

$$\{\varepsilon^{el}\} = \{\varepsilon\} - \{\varepsilon^{th}\} - \{\varepsilon^{pl}\} - \{\varepsilon^{cr}\} - \{\varepsilon^{sw}\} \quad (2.11)$$

In this context, ε^{th} corresponds to the thermal strain vector, ε^{pl} represents the plastic deformation vector, ε^{cr} refers to the creep strain vector, and ε^{sw} corresponds to the swelling strain vector, with ε representing the total strain vector of the system.

ANSYS Inc. (2024) also emphasizes that plasticity occurs independently of time. In this case, it is defined by the irreversible deformation that takes place in a material when a certain stress level is reached, known as the yield stress, and this plastic deformation occurs instantaneously, without being dependent on time. Thus, the yield criterion defines the stress level at which the material begins to deform plastically. ANSYS Inc. (2024) further explains that, for stresses with multiple components, this is expressed as a function of the individual components, $f(\{\sigma\})$, which can be interpreted as an equivalent stress, denoted by σ_e, as shown in Eq. 2.12.

$$\sigma_e = f(\{\sigma\}) \quad (2.12)$$

where $f(\{\sigma\})$ represents the stress vector. Finally, when the equivalent stress equals the material's yield parameter σ_y, the material will undergo plastic deformation; if σ_e is less than σ_y, the material behaves elastically, and the stresses will develop according to the elastic stress-strain relations. The relationship described can be seen in Eq. 2.13 below:

$$f(\{\sigma\}) = \sigma_y \tag{2.13}$$

According to Peric et al. (2011), complementing on previous definitions, the yield criterion can be expressed as follows, according to the relation below in Eq. 2.14:

$$\begin{aligned} &\text{If } f(\{\sigma\}) < 0 \rightarrow \varepsilon^{pl} = 0, \\ &\text{If } f(\{\sigma\}) = 0 \rightarrow \varepsilon^{pl} = 0, \text{ for elastic unloading,} \\ &\qquad\qquad \varepsilon^{pl} \neq 0, \text{ for plastic unloading.} \end{aligned} \tag{2.14}$$

For conducting tests within the ANSYS program, according to ANSYS Inc. (2024), there are several material behavior options available for each type of plasticity model, with the main ones including bilinear and multilinear isotropic stress-strain analysis, as shown in Figure 9 below, which will be mentioned in the methodology section of this work.

Figure 9 - Stress-strain behavior for each plasticity model in the ANSYS program.

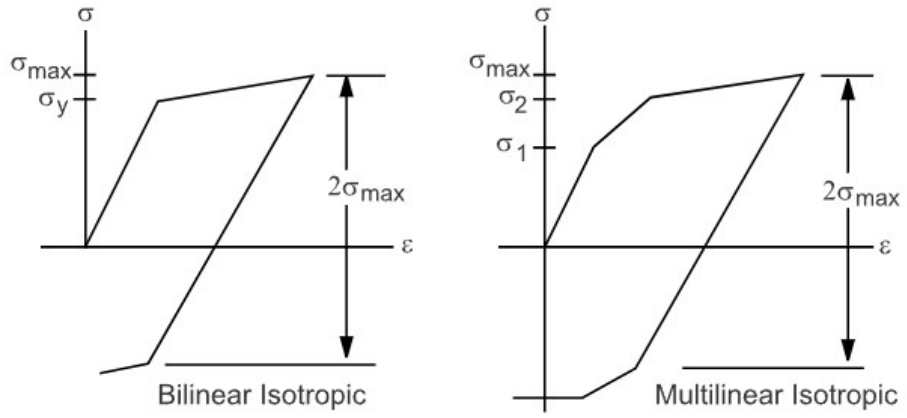

Source: ANSYS Inc. (2024).

2.3.4 The element birth and death technique

As discussed in the previous section, heat source models have been developed over time to achieve results that closely align with experimental tests, using the finite element method. Moreover, other methods have been applied to further enhance the accuracy of the results and to gain an exact understanding of the process and its actual impacts on the final outcomes, such as temperature gradients or residual stresses, for instance.

Thus, one of the features that began to be implemented in simulation softwares is the element birth and death technique. According to ANSYS Inc. (2024), if a given material is added to or removed from a part, certain elements that are part of that component may start to exist or cease to exist. Through this approach, the element birth and death technique is used to activate or deactivate these elements, as necessary.

ANSYS Inc. (2024) further explains how the deactivation of elements is performed by multiplying their stiffness matrix, or conductivity matrix, as shown in Eq. 2.7, by a severe reduction factor. Similarly, when elements "come to life," they are not newly added to the part but rather reactivated in the main equation. Consequently, when an element is reactivated, its stiffness matrix, mass, etc., return to their original values.

The representation of the element birth and death technique can be understood through Figure 10, as detailed by Fallahi et al. (2010). As illustrated below in a welding process, it is observed that during the passage of the heat source, the elements in the molten zone are activated, while the remaining elements will only be activated in the same manner once the heat source reaches the corresponding region in its fusion zone.

Figure 10 – Representation of the element birth and death technique in a welding process.

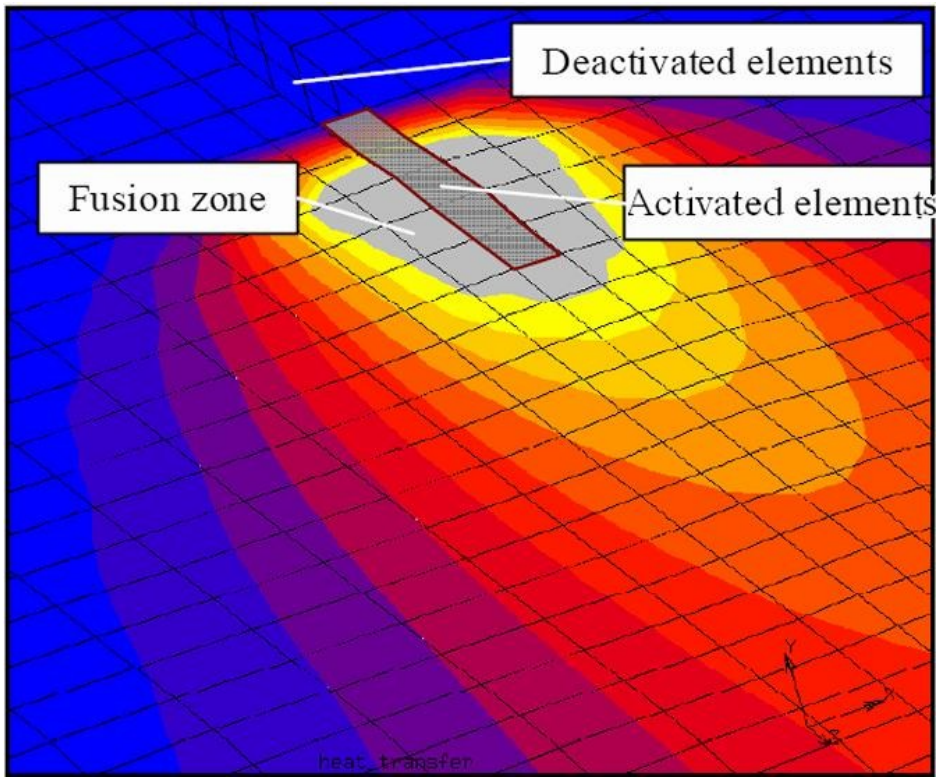

Source: Fallahi et al (2010).

In the literature, a number of studies have been carried out on different applications using this technique. Tchuindjang et al (2021) performs an analysis aiming to understand the evolution of the microstructure during additive manufacturing process of Ti6Al4V alloy, employing the element birth and death technique to simulate material deposition.

Roberts et al. (2009) employs this technique to model a three-dimensional temperature field in multiple layers during a powder bed fusion process, demonstrating the effects through temperature peaks observed in previous layers, achieving results similar to published experimental measurements.

In addition, to highlight the variety of applications of the technique, Li and Chen (2023) employ the element birth and death using ABAQUS® finite element software to develop a pipe-soil nonlinear coupling model, analyzing the impact of sensitive factors on stress response in buried gas pipelines in karst areas. The findings provide valuable insights for the design and safety of polyethylene gas pipelines subjected to ground displacement and surface damage.

3 METHODOLOGY

This work consists of a thermal and a sequentially coupled thermomechanical analysis. The simulations will be carried out using the computational software ANSYS, which utilizes the Finite Element Method (FEM) as the numerical resolution framework. The objective of this study is to develop an analysis method using this computational tool, in which it can describe the thermal and mechanical behavior during the welding process. The validation of this model will be carried out using numerical and experimental data from studies available in the literature. Thus, the temperature profile of the workpiece will be evaluated, using the data obtained from the thermal analysis as loading for the mechanical analysis, and the residual stresses will be subsequently verified, as shown in Figure 11.

Figure 11 - Illustrative diagram of the transient thermomechanical model.

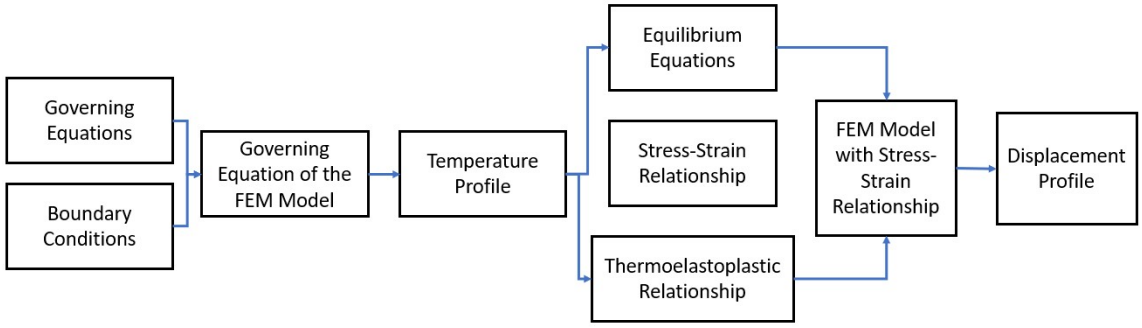

Source: Adapted from Chen (2011) and Lima et al (2022).

The study also proposes the use of a tool in the ANSYS software to simulate the insertion of a filler metal during the welding operation. This is the *Element Birth and Death* technique, which, according to Lima et al. (2022), allows for an accurate simulation of the welding gap filling process by the filler metal in the area where material is added. The three-dimensional transient analysis through FEM was developed to simulate the welding process using ANSYS APDL (Ansys Inc., 2018) (Ansys Parametric Design Language). This language allows the development of the heat source profile during the operation, whether a distributed Gaussian source or a Goldak double-ellipsoidal heat source. Thus, Figures 12 and 13 below presents the illustrative diagram of the tests to be performed, in a semi-infinite domain and in a butt welding with single pass on pipe and filler metal, respectively, including the element birth and death technique in the thermal and mechanical analyses for butt welding, as well as

variations in the types of meshes used, namely linear and quadratic, which will be detailed further.

Figure 12 – Illustrative flowchart of the tests conducted for semi-infinite domain.

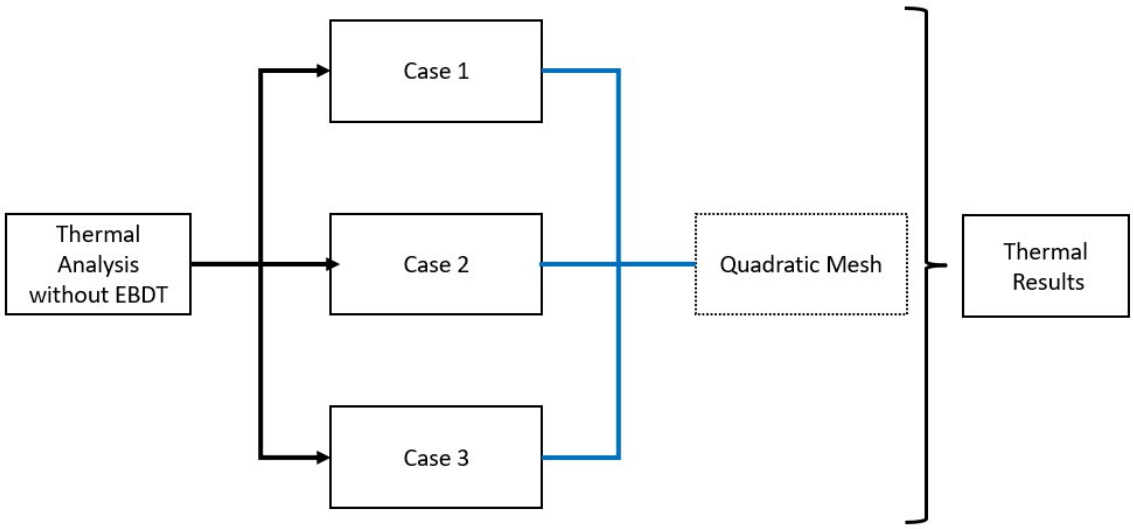

Source: Prepared by the author.

Figure 13 – Illustrative flowchart of the tests conducted for butt welding with single pass on pipe, comparing the application of the element birth and death technique in thermal and mechanical analysis, with the variations in the meshes used (linear and quadratic) for both approaches.

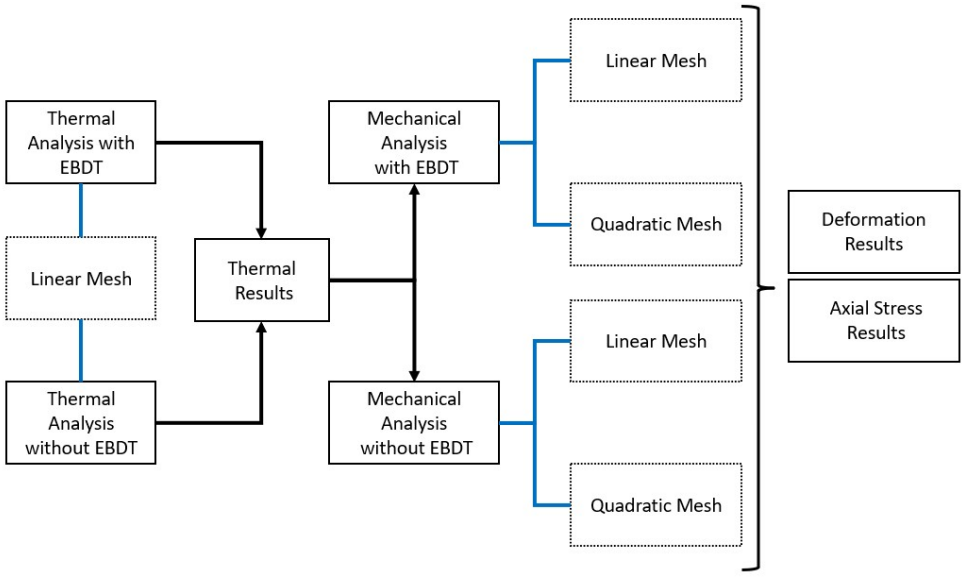

Source: Prepared by the author.

3.1 Thermal analysis

3.1.1 3D Double ellipsoidal heat source through ANSYS APDL

Initially, to model the welding environment computationally, it is necessary to develop the heat source model to be used in the process. Therefore, using ANSYS APDL, this work will focus on the development of the double-ellipsoidal heat source algorithm for plates and tubes, as per the calculations developed in the work of Goldak et al. (1984).

Thus, in Appendix A, the developed algorithm for plate welding can be consulted, and similarly, in Appendix B, the APDL algorithm for tube welding is provided.

3.1.2 3D Moving heat source in a semi-infinite domain

The case verification was conducted by comparing the current work with the analytical solutions of Fachinotti et al. (2011) and the numerical solutions from Rocha's thesis (2022). In these referenced works, the temperature profiles were calculated by moving a double-ellipsoidal heat source over a semi-infinite plate for welding processes.

The case was carried out in the ANSYS software by comparing the variation in temperature over time at a specified point, as well as the temperature profiles along a specified path, as shown in Figure 14, which will be detailed later. The study primarily focuses on the validation of the APDL code for metal plates, and the element birth and death method was not used for this verification.

Table 1 shows the geometric and physical welding parameters used in this analysis, based on the aforementioned studies. Additionally, the total time for the analysis will be set at 20 seconds, with a time step of 0.05 seconds, kept constant throughout the simulation. Appendix A provides the APDL code utilized in this study.

Figure 14 – Geometry used in the computational analysis.

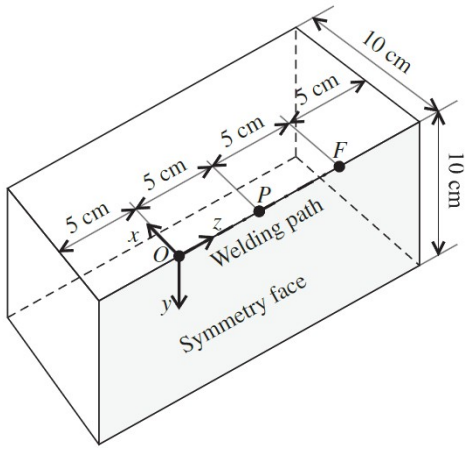

Source: Adapted from Fachinotti et al (2011).

Three different cases are considered in this work, which are highlighted as A, B, C in Table 1. There is a variation in the dimension of the heat source deposited in the front and rear regions of the double-ellipsoidal profile.

Table 1 - Physical and geometric welding parameters used.

Parameter	Case		
	A	**B**	**C**
c_f , c_r	6 mm, 24 mm	15 mm, 15 mm	24 mm, 6 mm
f_f , f_r	0.4, 1.6	1.0, 1.0	1.6, 0.4
b, a		2 mm, 10 mm	
k		29.0 W/m.K	
c		600 J/kg.K	
ρ		7820 kg/m³	
Q		5083 W	
v		5 mm/s	
T_0		20 °C	

Source: Adapted from Fachinotti et al (2011) and Rocha (2022).

3.1.3 Butt welding with single pass on pipe and filler metal

The present case was conducted on a pipe with a single-pass butt welding, comparing the finite element analysis from Karlsson and Josefson (1990) and the element based finite volume method from Rocha (2022) through the simulation of circumferential

welding and comparative analysis of the thermal profile in the welded area. The welding method used is the MIG (Metal Inert Gas) process.

The pipe's external diameter, wall thickness, and total length are 114.3 mm, 8.0 mm, and 400 mm, respectively. Due to the symmetry of the weld bead and the optimization of computational test duration, only half of the pipe will be analyzed.

In the study by the authors, filler metal is added into a V-shaped groove with a depth of 5.5 mm. To represent the analysis according to the literature, the "element birth and death" tool from the ANSYS software, coupled with the previously mentioned APDL language, will be used in the transient thermal test. Thus, the welding elements in the front region of the arc will only be activated at the point where the heat source enters the element. For comparative purposes, a test will also be performed without the material activation technique after the heat source passes.

As mentioned in the previous section, the total time for the analysis will be set to 120s, with a time step of 0.1s kept constant throughout the simulation. The material to be tested is a carbon-manganese steel alloy with a composition of 0.18% C, 1.3% Mn, 0.3% Si, 0.3% Cr, and 0.4% Cu. The considered model includes geometric and thermal properties as shown in Figure 15. TC stands for thermal conductivity, HTC denotes the heat transfer coefficient, SH-BM denotes the specific heat at the base metal, and SH-HAZ is the specific heat at the heat-affected zone.

Figure 15 – Geometry of the pipe with joint weld and thermal properties of the material.

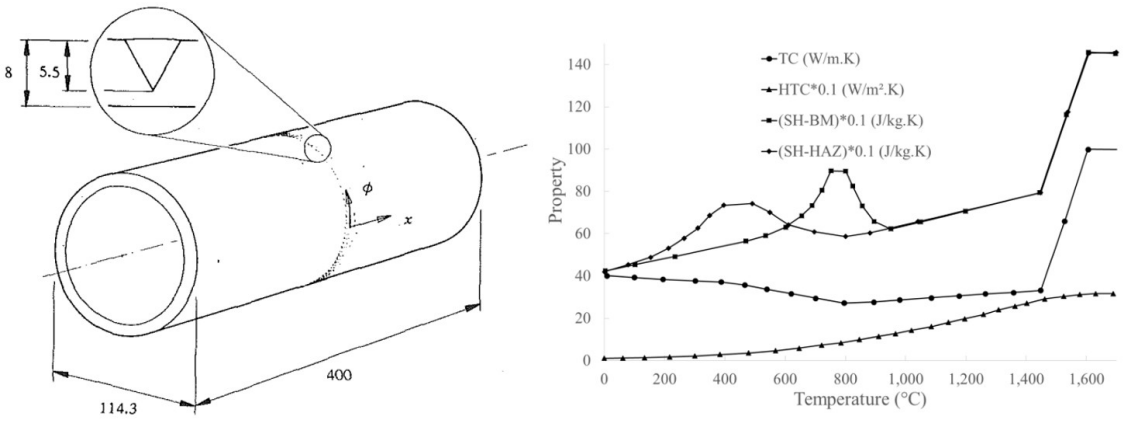

Source: Adapted from Karlsson and Josefson (1990) and Rocha (2022).

Finally, for this case, the following welding parameters will be used: a supplied power of 3780 W, an ambient temperature of 20 ºC, a source efficiency of 90%, and a welding

speed of 6 mm/s. As for the geometric parameters of the heat source, the values from case B in Table 1 will be used, since the heat source model is simple-ellipsoidal.

3.2 Thermomechanical Analysis

3.2.1 Butt welding with single pass on pipe and filler metal

Similarly to the previous section, this section aims to analyze the angular distortions and residual stresses of the welded tube with filler metal, adhering to the parameters provided in the work of Karlsson and Josefson (1990), in Section 3.1.3. The mesh created for the solid element is used in the thermomechanical analysis, and in this scenario, the "*element birth and death*" tool will also be applied during the mechanical test. Finally, the total test duration and the time step for each iteration will be maintained to preserve the methodology previously adopted.

Thus, Figure 16 presents the mechanical properties of the carbon-manganese steel alloy, all of which are temperature-dependent.

Figure 16 - Yield stress, Poisson's ratio, thermal strain, and Young's modulus as a function of temperature.

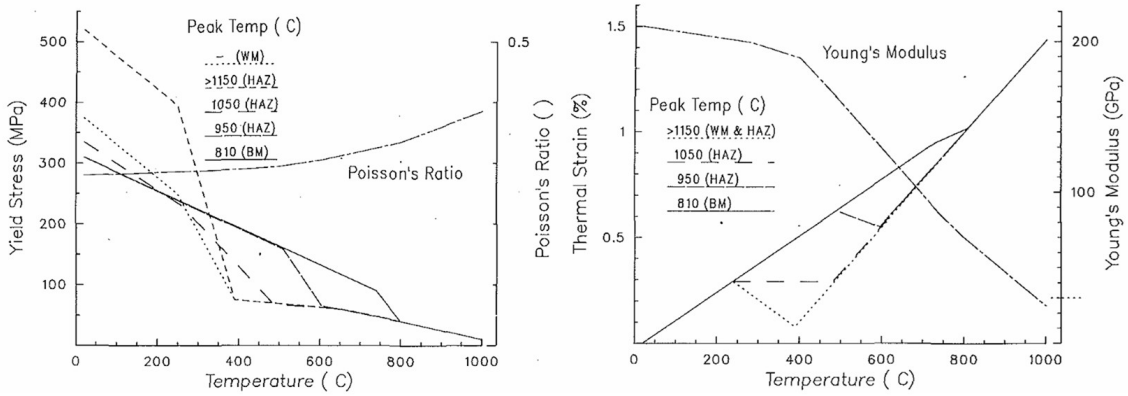

Source: Adapted from Karlsson and Josefson (1990).

3.3 Finite Element Analysis using ANSYS software

The methodology employed for conducting the thermal and mechanical studies proposed in this section was the Finite Element Method (FEM), using the ANSYS *Mechanical* software.

In the finite element method, as in any numerical procedure, the domain is subdivided into small elements and nodes. This method uses integral formulations to create a system of algebraic equations, and a continuous approximate function is determined to represent the solution for each element. Consequently, the complete solution is generated by connecting individual solutions, ensuring continuity at the boundaries between elements.

In the ANSYS program, various types of tests can be performed, including stress analysis, heat transfer, fluid dynamics, electromagnetism, among others. These tests can also involve linear and nonlinear analyses, in both steady-state and transient regimes.

For this work, efforts will focus on thermal and mechanical analyses, including elasticity and plasticity evaluation, involving transient problems, limited to a specific time period, as previously outlined in the earlier sections.

3.3.1 Moving 3D heat source in a semi-infinite domain

3.3.1.1 Definition of geometry and materials

The design of the semi-infinite domain in plate format, depicted in Figure 14, was developed using the ANSYS software, specifically with the ANSYS SpaceClaim tool. The three-dimensional representation of the design is shown in Figure 17 below, maintaining the original external dimensions defined by Fachinotti (2011) and the region designated for the heat source passage.

Figure 17 – Three-dimensional representation of the semi-infinite domain in ANSYS software in isometric perspective.

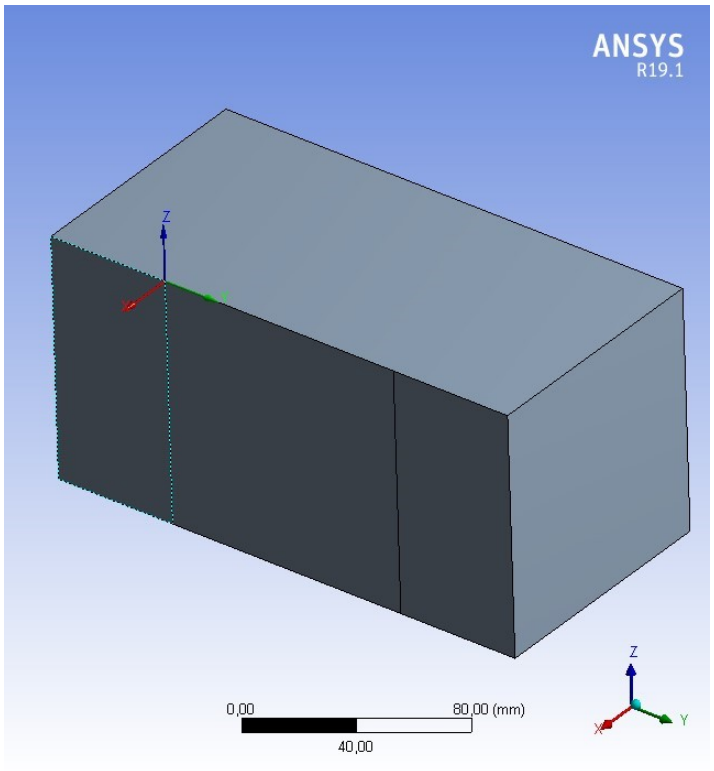

Source: Prepared by the author.

Regarding the material used, based on the properties described in Section 3.1.2, the thermal properties and welding parameters were input for the development of computational tests. For the thermal properties, as outlined in Table 1, a new material named *Fachinotti Material* was created within the Engineering Data module of ANSYS Workbench, storing data on density, thermal conductivity, and specific heat, as shown in Figure 18 below. Using these data, the material was applied throughout the entirety of the piece, encompassing the three cases described in Table 1.

Figure 18 – Thermal test properties input into the ANSYS program.

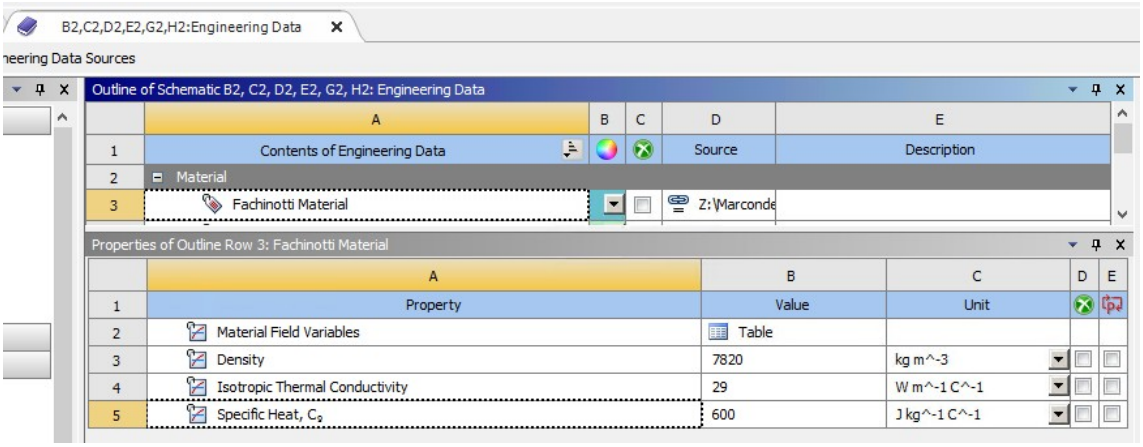

Source: Prepared by the author.

At the conclusion of the initial configurations of geometry and material properties, these data were input into the Transient Thermal analysis mode of the ANSYS software. According to ANSYS Inc. (2024), this analysis involves determining temperatures and other thermal quantities that vary over time. Thus, the representation of the analyses for the three created cases can be visualized in Figure 19 below.

Figure 19 – Transient thermal analysis for the semi-infinite domain with the cases created in the ANSYS program.

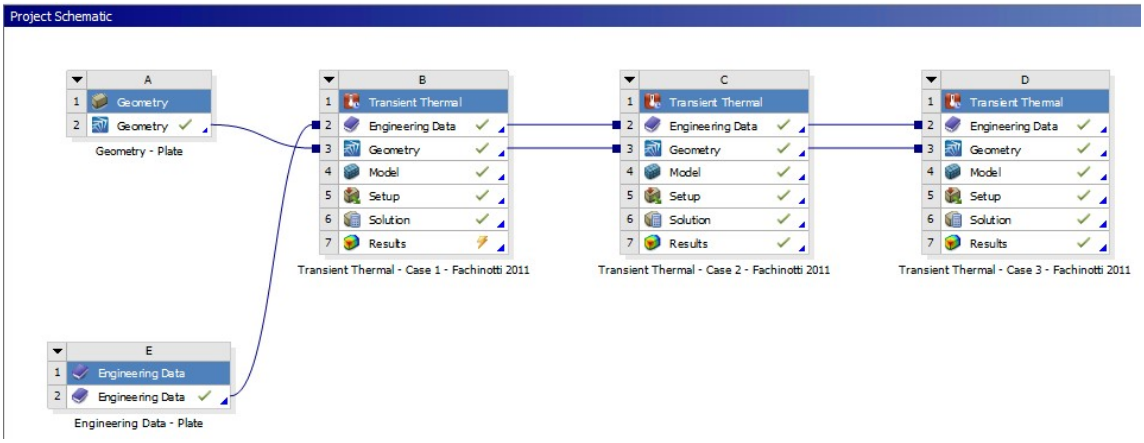

Source: Prepared by the author.

3.3.1.2 Mesh definiton

The mesh generation for the plate used in the FEM study was produced in the ANSYS Mechanical software. When creating meshes in this software, two element types can be utilized: linear and quadratic elements.

According to ANSYS Inc. (2024), the element order option allows users to control whether the meshes will include midside nodes (quadratic elements) or omit them (linear elements). By reducing the number of midside nodes, the number of degrees of freedom and the number of equations required to solve the system's linear matrix can be decreased. Figure 20 illustrates the difference between linear and quadratic elements.

Figure 20 – Types of mesh element order: linear and quadratic.

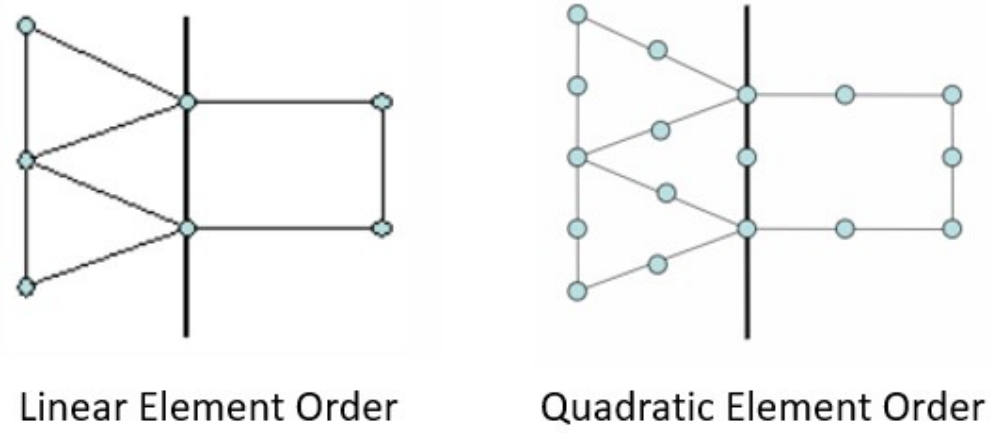

Source: Adapted from ANSYS Inc. (2024).

In this case, quadratic elements were exclusively used for the thermal analysis. For the three cases created, the mesh consisted of 168,587 elements and 238,048 nodes. In Rocha's (2022) study, a linear-order element mesh was employed, using an unstructured grid.

All mesh elements created were of the SOLID87 type, which is a tetrahedron element with 10 nodes. According to Eren (2014), this 10-node element type is suitable for modeling irregular meshes, with each tetrahedral model having one degree of freedom corresponding to temperature at each node. Additionally, this element can be used for both steady-state and transient thermal analyses. Figure 21 below shows a model of a SOLID87

element, as described by ANSYS Inc. (2024), where the midside nodes M, N, O, P, Q, and R can be observed.

Figure 21 – Representation of SOLID87 Geometry.

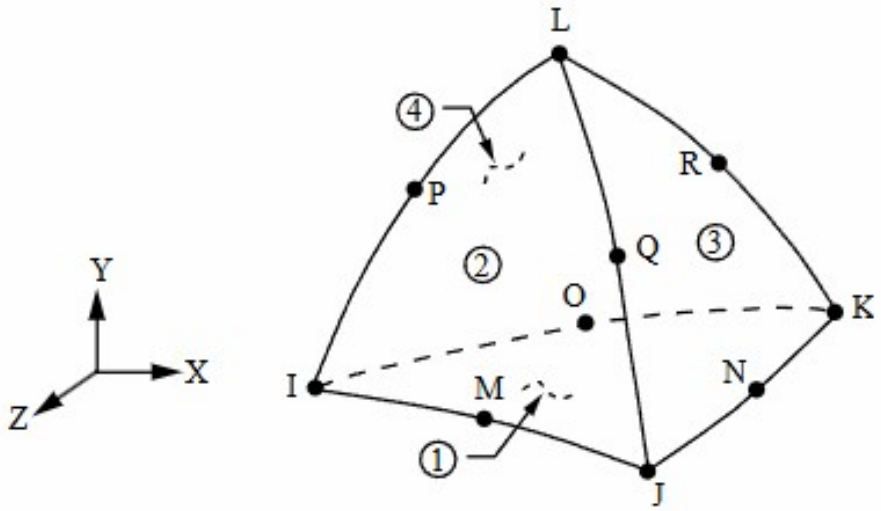

Source: ANSYS Inc. (2024).

In the mesh configuration, to achieve greater accuracy in the temperature data at the end of the test, the *Refinement* tool was applied. According to ANSYS Inc. (2024), this feature allows the user to refine a mesh from level one, representing the minimum refinement, to level three, the maximum refinement, relative to its original configuration. Thus, only the edge of the plate where the heat source would perform the welding process was selected, as this region experiences the highest concentration of temperature. Finally, a standard element size of 5 mm was defined for the entire three-dimensional profile, as represented in Figure 22 below.

Figure 22 – Final representation of the tetrahedral mesh, detailing the edge of the most refined region, using second order elements.

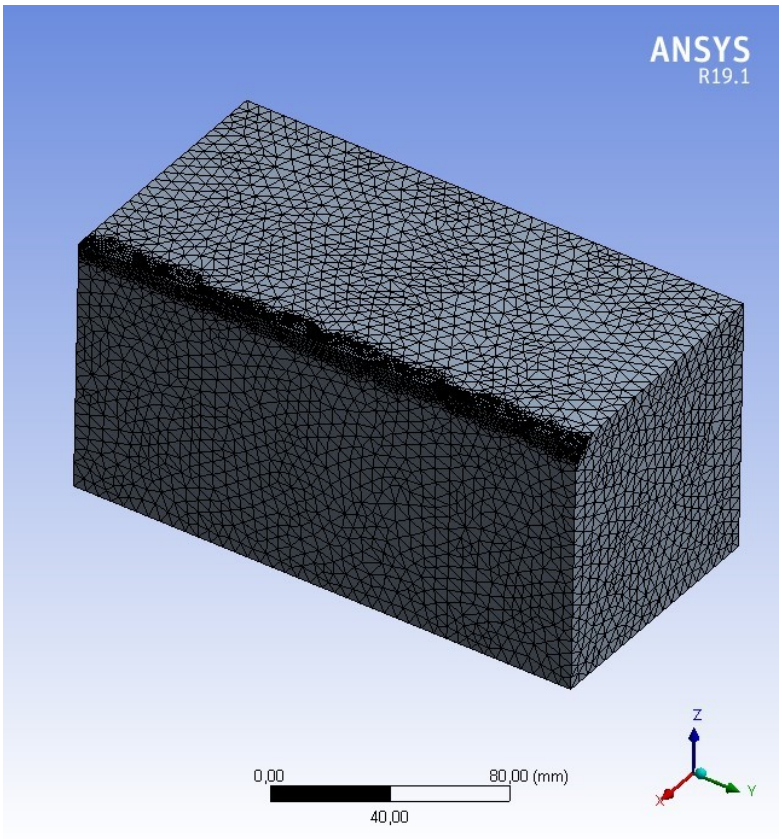

Source: Prepared by the author.

3.3.1.3 Boundary conditions

For the boundary conditions applied to the plate, heat losses due to convection and radiation were not considered. The origin of the Cartesian coordinate system was located at the beginning of the welding process to be performed by the heat source, as shown in Figure 17.

In the Goldak source model, the thermal properties were based on Table 1 and were inserted during the development of the APDL code, which can be consulted in Appendix A. The heat source moves along the y-axis for 100 mm at a speed of 0.005 m/s, completing the single welding pass in approximately 20s.

The heat source model used was the double ellipsoidal Goldak source for cases A and C, based on Eqs. 2.4 to 2.6, as the values of *cf* and *cr* differ, and with the values of *a* and *b*

presented in Table 1. In case B, a simple ellipsoidal model was considered, as *cf* and *cr* are equal, both at a distance of 15 mm.

For the creation of the Goldak heat source on the plate, the following steps were carried out. As an example, case B will be represented below, but the same considerations apply to cases A and C. Initially, the heat source parameters for case B were input, following the instructions in Table 1, through Eqs. 2.15 to 2.20.

A = 0.010 m (2.15)

B = 0.002 m (2.16)

C1 = 0.015 m (2.17)

C2 = 0.015 m (2.18)

FF = 1.0 (2.19)

FR = 1.0 (2.20)

where C1 corresponds to cf and C2 corresponds to cr.

For the welding parameters, the heat source power Q and welding speed VEL data were input, as represented by Eqs. 2.21 and 2.22, respectively.

Q = 5083 W (2.21)

VEL = 0.005 m/s (2.22)

To use the Goldak model on the plate, the following adjustments were made, as detailed below. Initially, at each iteration, the coordinates of the centroid of each element are adjusted using Eqs. 2.23 to 2.25, through the CENTRX function defined in the APDL language. From this point, the heat source moves along the y-direction, according to Eq. 2.23, advancing by each time step of 0.05s, with the variation in coordinates. The movement of the source along the y-axis is represented by Eq. 2.26.

X = CENTRX(jj) (2.23)

Y = CENTRY(jj) (2.24)

Z = CENTRZ(jj) (2.25)

CSI=Y+VEL*(TAU-WTIME) (2.26)

Therefore, adapting the Goldak source equation, as contained in Eq. 2.5, for a simple and double ellipsoidal heat source using the APDL language, the formulas described in Eqs. 2.27 to 2.29 are used to obtain the heat source power at each time step:

PART1=(6*(3**0.5)*Q*F) / (A*B*C*3.14*(3.14**0.5)) (2.27)

PART2=(EXP(-3*(X/A)**2)) * (EXP(-3*(Z/B)**2)) * (EXP(-3*((CSI/C)**2))) (2.28)

QF=PART1*PART2 (2.29)

where the values of c*f*, c*r*, f_f e f_r are adjusted at each iteration, depending on the position of the source along the y-direction and the time step iteration, as can be seen in more detail in Appendix A.

3.3.2 Single-pass butt weld in tube with filler metal and EBDT technique

For the execution of the computational test in ANSYS software for the butt weld on the tube with a single pass and the use of filler metal, the test was performed with the following structure, which will be detailed in the following sections.

3.3.2.1 Geometry and material definitions

The geometry of the tube was modeled in a three-dimensional aspect, similar to Figure 14, using one of the tools in the ANSYS program called ANSYS *SpaceClaim*. The design can be seen below in Figure 23, showing only half of the tube to optimize the total test time, as this is one of the most important factors in computational analysis.

Figure 23 – View of the symmetric three-dimensional tube in isometric perspective.

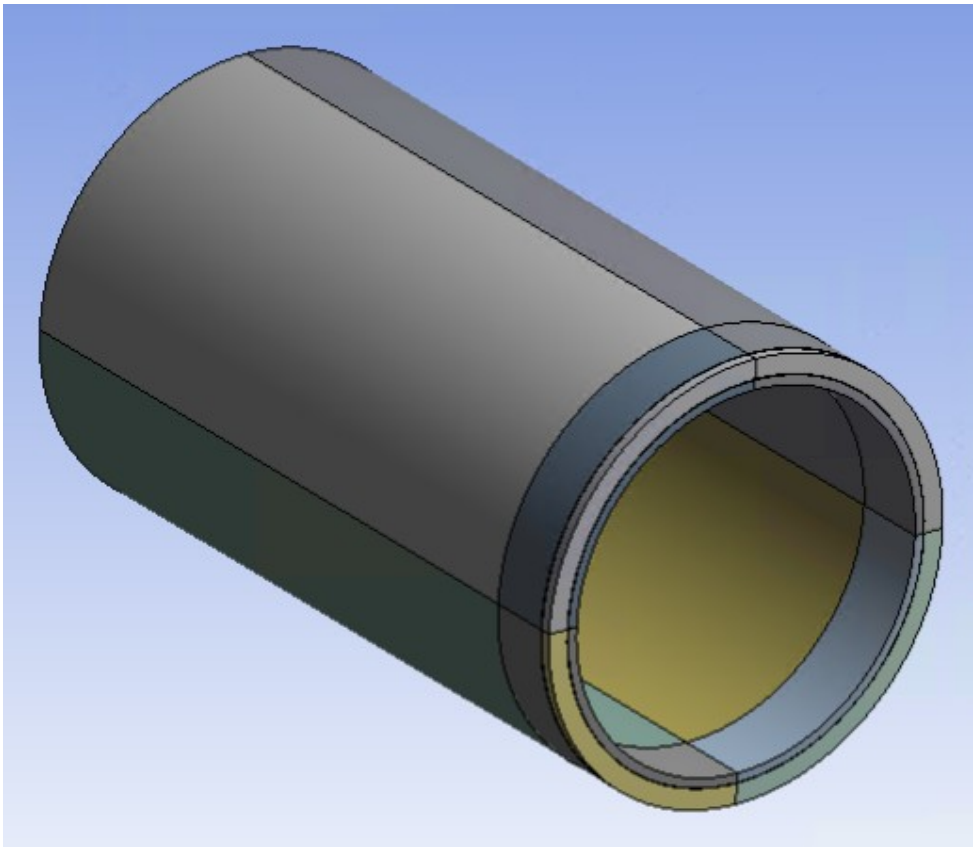

Source: Prepared by the author.

For the purpose of optimizing the calculations performed by ANSYS and improving the mesh refinement, the tube was fragmented into several parts, as shown in Figure 23, using the Share Topology feature within the ANSYS SpaceClaim tool. This way, the fragmented bodies are grouped into multi-body parts, allowing for a continuous mesh in common regions where the bodies are in contact, thus avoiding the need to define contact regions within ANSYS Mechanical, which will be discussed in the following sections.

Both for the filler metal region and the thermally affected zone, as well as for the rest of the base metal, the thermal and mechanical properties of the carbon-manganese steel alloy were used, as presented in Figures 15 and 16. This level of detail can be visualized in Figure 24 below, with green highlighting for each of the regions and their respective thermal and mechanical properties used in the tests.

Figure 24 – Details of the thermal and mechanical properties used for the manganese carbon steel alloy for the filler metal and heat-affected zone (on the left) and the base metal (on the right).

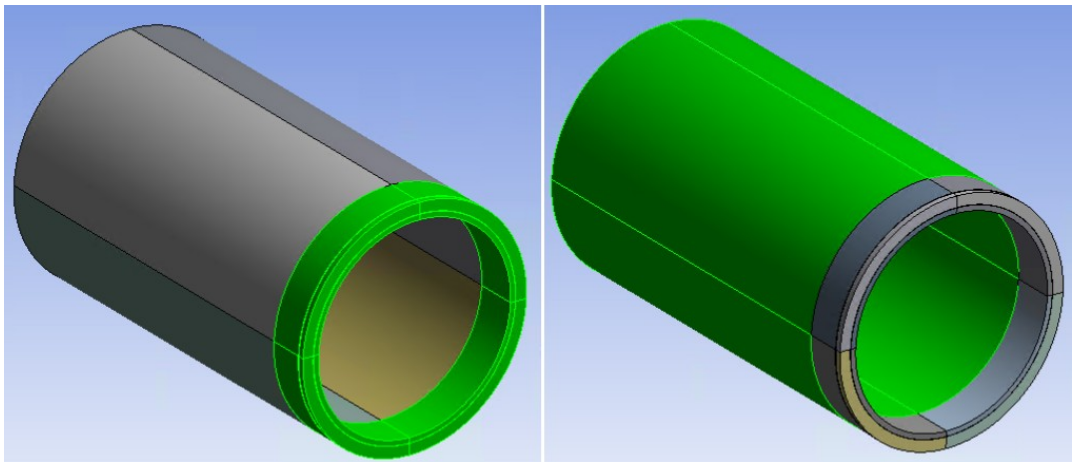

Source: Prepared by the author.

In Figure 25, the representation in the ANSYS program of the thermal conductivity for the carbon-manganese steel alloy can be seen, as initially shown in Figure 15.

Figure 25 – Thermal conductivity for carbon-manganese steel represented in Ansys program.

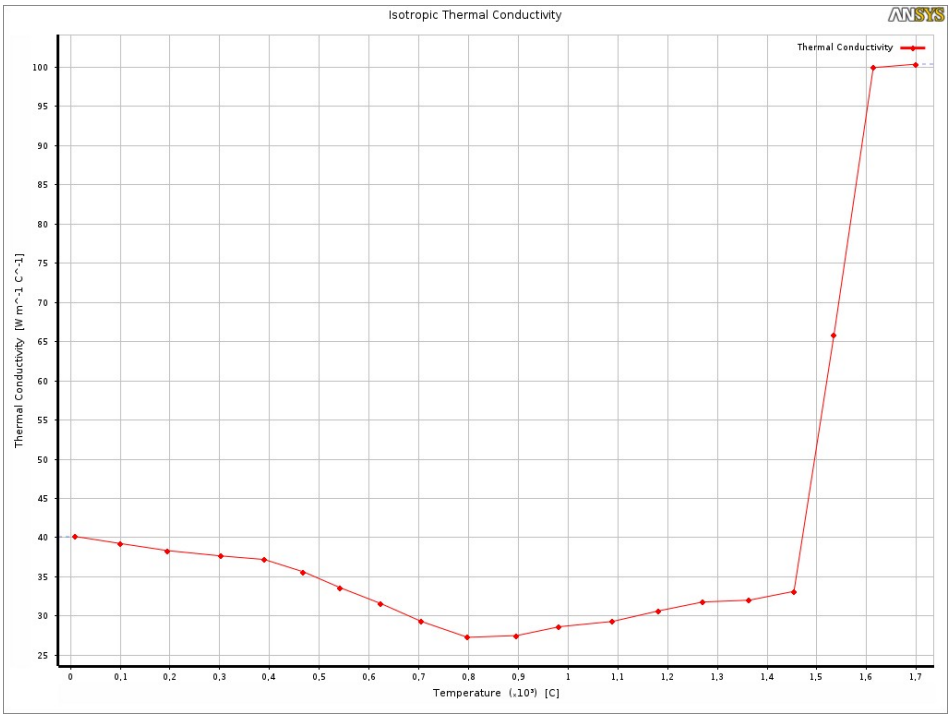

Source: Prepared by the author.

For Figure 26 below, the specific heat can be seen for both the base metal and the thermally affected zone, with the values input into the ANSYS program, similar to the original work by Karlsson and Josefson (1990), also initially presented in Figure 15.

Figure 26 – Specific heat for base metal (on the left) and filler material (on the right) for carbon-manganese steel.

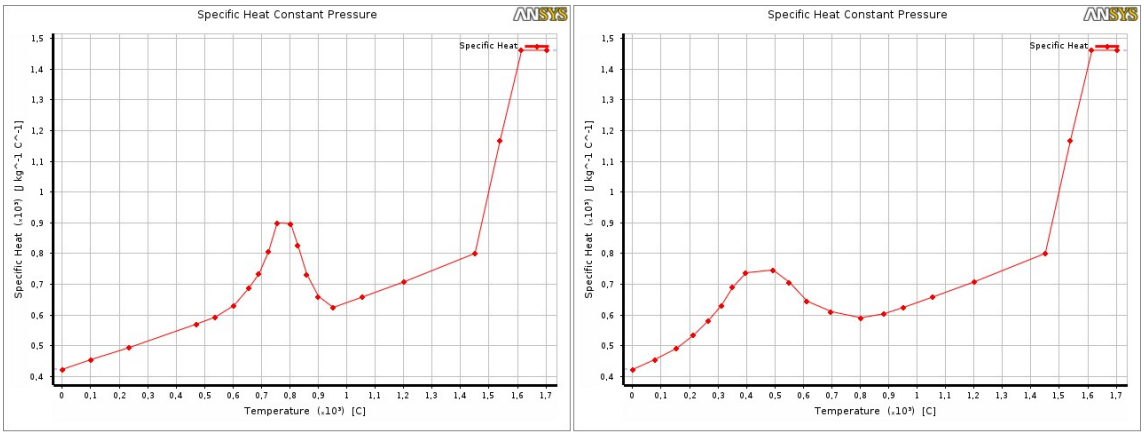

Source: Prepared by the author.

For the mechanical properties of the tube, the values initially shown in Figure 16 were input into the ANSYS program, summarized in Figures 27 and 28. In Figure 27, the elasticity parameters used for Young's Modulus and Poisson's ratio can be observed, highlighting that both vary according to the temperature of the tube. Regarding plasticity, in Figure 28, the bilinear isotropic hardening method was used, with the stress-strain profiles varying with temperature, and considering a perfectly plastic material.

Figure 27 – Elasticity parameters used for mechanical analysis.

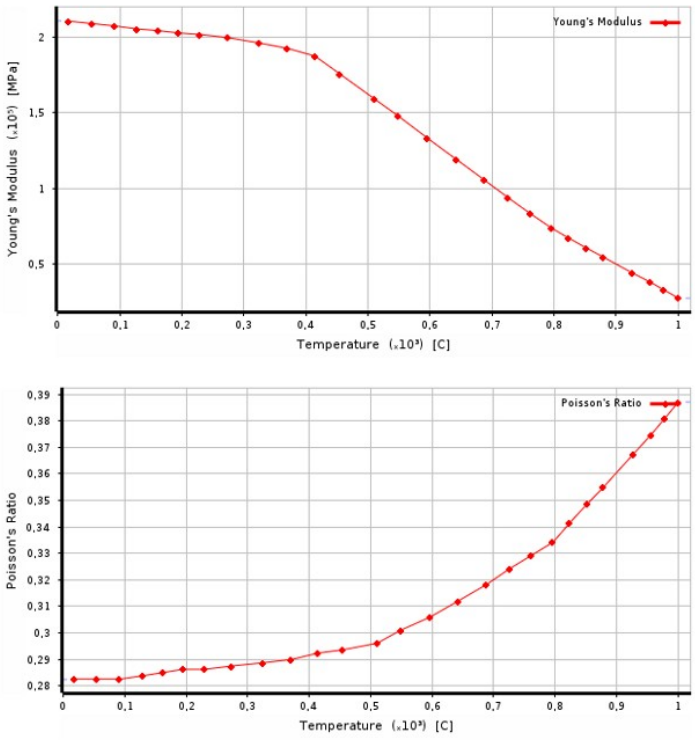

Source: Prepared by the author.

Figure 28 – Plasticity parameters used for mechanical analysis.

Base Metal

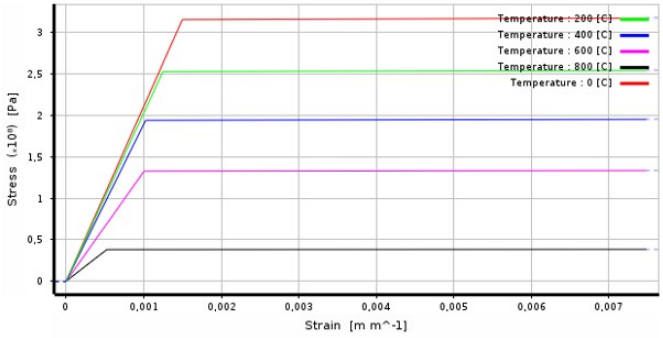

Filler Material

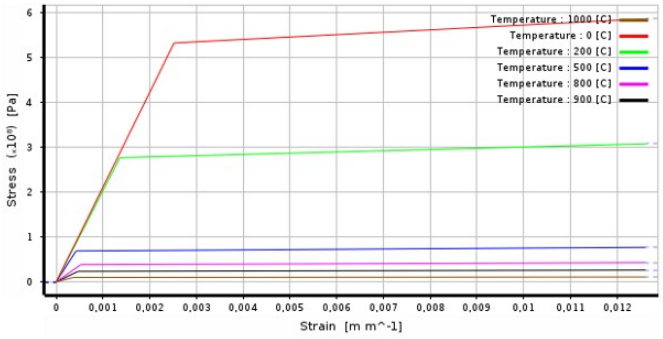

Source: Prepared by the author.

3.3.2.2 Mesh definition

The creation of the tube mesh for the FEM study was also carried out in ANSYS Mechanical. Both for the thermal and mechanical analysis, similar mesh characteristics were used, such as element size and geometric features, as well as the number of nodes.

For the transient thermal analysis, the tests were performed using mesh with first order elements. For the transient structural analysis, both mesh with linear and quadratic elements were created with the aim of evaluating the efficiency of the tests through the analysis of residual stresses and displacements.

In the meshes with linear order elements, there were 73,058 elements of type SOLID185, 7,177 elements of type CONTA174, and 7,177 elements of type TARGE170, with 74,394 nodes. According to Khare and Mittal (2017) and ANSYS Inc. (2009), a structural solid element of type SOLID85 is used for modeling three-dimensional solid structures in general, with 8 nodes in each element and 3 degrees of freedom corresponding to translations in the x, y, and z directions, as shown in Figure 29 below.

Figure 29 – Three-dimensional representation of the SOLID85 element with 8 nodes.

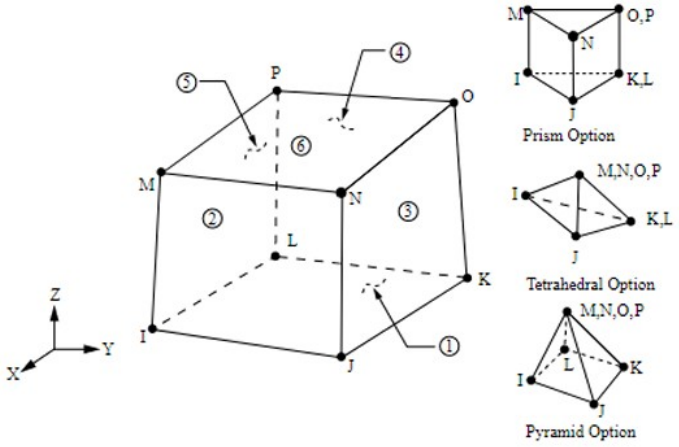

Source: ANSYS Inc. (2009).

Additionally, for the CONTA174 elements, according to ANSYS Inc. (2009), they are used to represent deformable surfaces that come into contact with a target surface, being employed in contact analyses, both in pair-based contact and general contact. For the TARGE170 elements, they are used to represent rigid target surfaces in a contact analysis. Therefore, for these two types of elements, they were used in the computational test with the purpose of fixing the contacts between each of the fragmented parts of the tube, ensuring that all sub-parts behave as a single body. Figure 30 below exemplifies the concept presented.

Figure 30 – Representation of the geometry of the CONTA174 and TARGE170 elements.

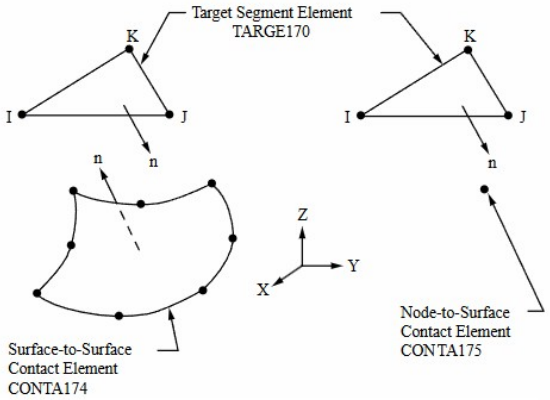

Source: ANSYS Inc. (2009).

In the meshes with quadratic order elements, 11,355 elements and 50,907 nodes were created, significantly fewer than those obtained when generating the mesh with linear order elements. Given that the test duration is one of the primary factors in performing computational tests and that quadratic order elements have nodes between vertices, which provides greater precision in results but negatively impacts the total test time, the element size in the weld bead and thermally affected zone was adjusted for this configuration. Therefore, although the mesh is coarser, the goal is to evaluate the efficiency of quadratic order elements in structural results while optimizing test time. In Rocha's (2022) study, an unstructured linear element mesh composed of 1,800 prisms, 25,920 hexahedrons, and 36,000 nodes was used — significantly fewer than in the present study, which employs approximately 75,000 nodes for the linear order element mesh and 51,000 nodes for the quadratic order element mesh.

Thus, for the filler metal, the elements used in the mesh were prismatic, with a size of 1mm for linear order elements and 2mm for quadratic order elements. For the thermally affected zone, the elements used were hexahedral, with a size of 1mm for linear order elements and 2mm for quadratic order elements as well. Finally, in the base metal, farther from the weld bead, hexahedral elements of 10mm in size were used, with a coarser mesh compared to the two previous refinements. Figure 31 below shows the mesh used for both thermal and mechanical tests.

.

Figure 31 – Representation of the tube mesh in isometric view, with refinement of linear order elements (on the left) and quadratic order elements (on the right).

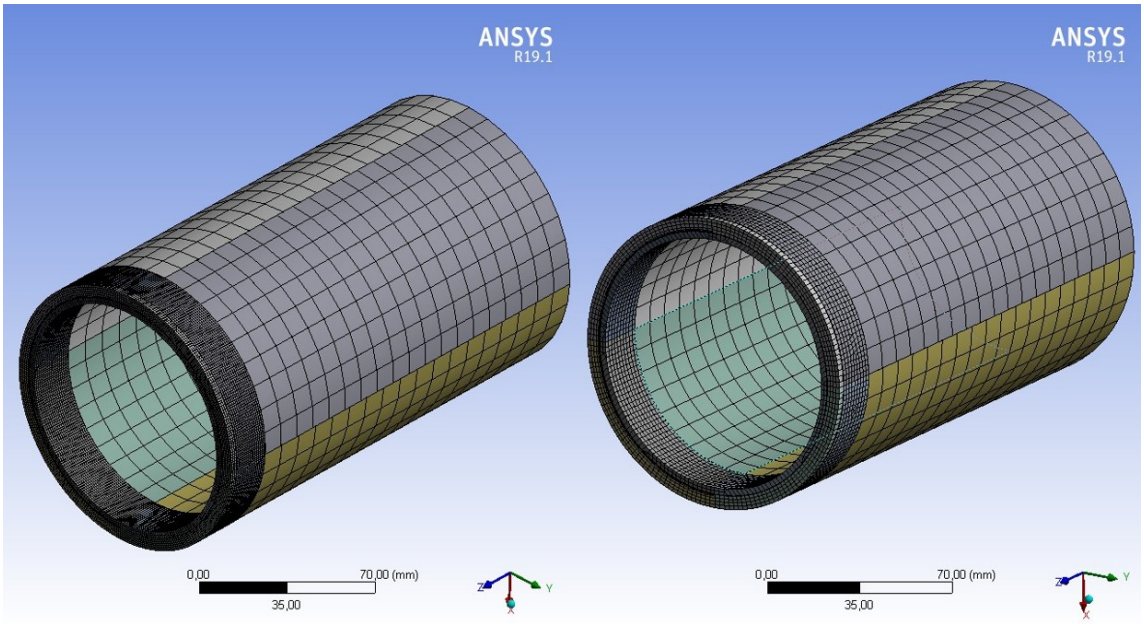

Source: Prepared by the author.

3.3.2.3 Boundary conditions

For the boundary conditions used in the tube, similarly to the work of Karlsson and Josefson (1990), heat losses by convection and radiation were considered, applying them to all faces of the tube, both internal and external, except for the symmetry surface, which was kept isolated.

The origin of the Cartesian coordinate system was located at the center of the tube, in the symmetric region near the weld bead. The heat source was positioned at a distance of 57.15mm from the origin of the coordinate system along the y-axis, which corresponds to the radius of the tube, as shown in Figure 32.

.

Figure 32 – Representation of the coordinate system origin for the tube.

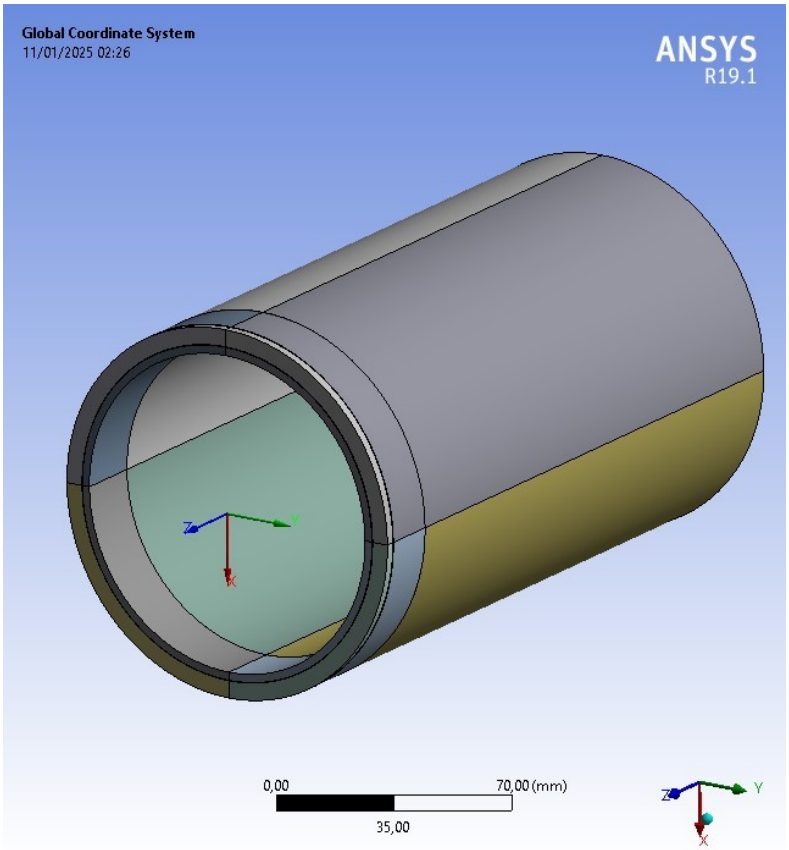

Source: Prepared by the author.

In the Goldak heat source model, the thermal properties were the same as those already defined in section 3.1.3, and they were inserted during the development of the APDL code, which can be found in Appendix B. The heat source rotates counterclockwise at a speed of 0.006 m/s, completing the single welding pass in approximately 60 seconds, followed by 60 seconds of tube cooling, totaling the 120 seconds of the test.

The heat source model used was the simple ellipsoidal Goldak source, based on Eqs. 2.4 to 2.6, since the values of c*f* e c*r* are equal, with the values of *a*, *b* e *c* represented in Eq. 2.32. To apply the Goldak model to the tube, the following modifications were implemented, detailed below. Initially, it was defined that the angle of the weld bead, denoted by alfa, is zero. Therefore, the heat source was always positioned normal to the weld bead surface, as indicated in Eq. 2.30. Since the origin of the tube's coordinate system is located at the center of the tube, in the symmetric region, the values of dx, dy, and dz, referring to the

initial position of the weld from the start of the bead, were adjusted only along the y-axis, advancing by 0.05715m, which corresponds to the radius of the tube, as detailed in Eq. 2.31.

Additionally, to create the rotation matrix of the heat source around the z-axis, it was necessary to calculate the angle between the heat source's position and the origin. This value, defined as beta, was obtained in radians, as shown in Eq. 2.33, with VEL being the welding speed in m/s and Δt being the defined time step. Finally, the final rotation matrix is detailed in Eq. 2.34.

alfa = 0 (2.30)

dx = 0 (2.31)

dy = 0.05715

dz = 0

a = 0.0035 m (2.32)

b = 0.006 m

c = 0.005 m

beta = (VEL*Δt) / R (2.33)

$$\begin{pmatrix} x' \\ y' \\ z' \end{pmatrix} = \begin{pmatrix} \cos(beta) & -sen(beta) & 0 \\ sen(beta) & \cos(beta) & 0 \\ 0 & 0 & 1 \end{pmatrix} \begin{pmatrix} x \\ y \\ z \end{pmatrix} \quad (2.34)$$

Therefore, adapting the Goldak heat source equation, contained in Eq. 2.5, for a simple ellipsoidal heat source, we have:

$$q(x,y,z,t) = \frac{6\sqrt{3}\eta Q}{abc\pi\sqrt{\pi}} e^{-3\left(\frac{x'^2}{c^2}+\frac{y'^2}{b^2}+\frac{z'^2}{a^2}\right)} \quad (2.35)$$

where:

$$x' = \{\cos(beta) * [-(x1 + R * \sin(beta))]\} + \{sen(beta) * [-(y1 + R * (1 - \cos(beta)))]\} \quad (2.36)$$

$$y' = \{-sen(beta) * [-(x1 + R * \sin(beta))]\} + \quad (2.37)$$

$$\{cos(beta) * [-(y1 + R * (1 - cos(beta)))]\}$$

$$z' = z1 \tag{2.38}$$

For the mechanical simulation, the boundary condition for the tube was defined by clamping at the rear face, farthest from the weld bead, as represented in Figure 33.

Figure 33 – Fixed support defined as the boundary condition in the mechanical analysis.

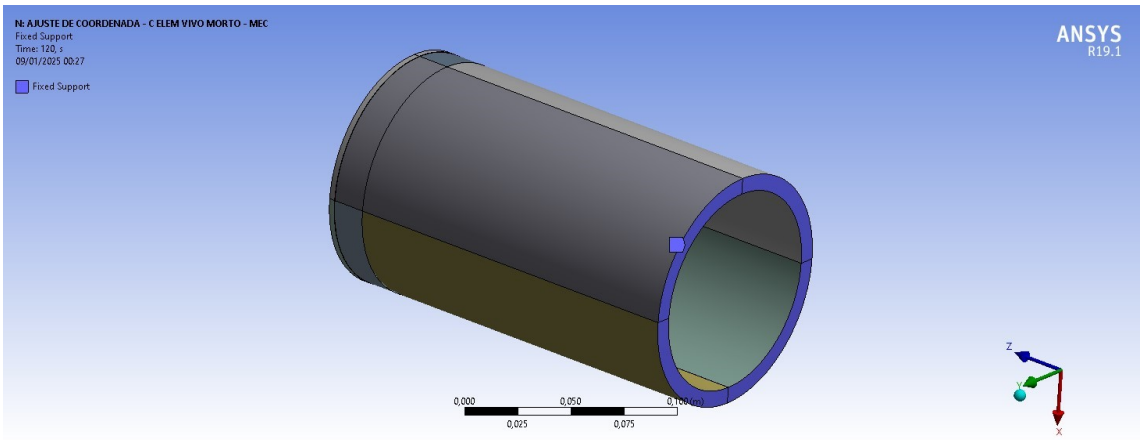

Source: Prepared by the author.

In addition, as input data for the mechanical analysis, and as previously introduced in the initial part of this methodology, the temperatures obtained from the thermal analysis were inserted into the mechanical analysis using the Imported Body Temperature tool from ANSYS Mechanical. Thus, all the results obtained at each mesh node, for all the time steps calculated in this study, were used to obtain the displacement and residual stress values, which will be discussed in the results and discussion section of this work. The representation of this tool is illustrated in Figure 34, showing the temperatures obtained in the first time step of the thermal analysis, detailing the highest and lowest value obtained for this quantity in the tube.

Figure 34 – Imported body temperature used as thermal input for mechanical analysis.

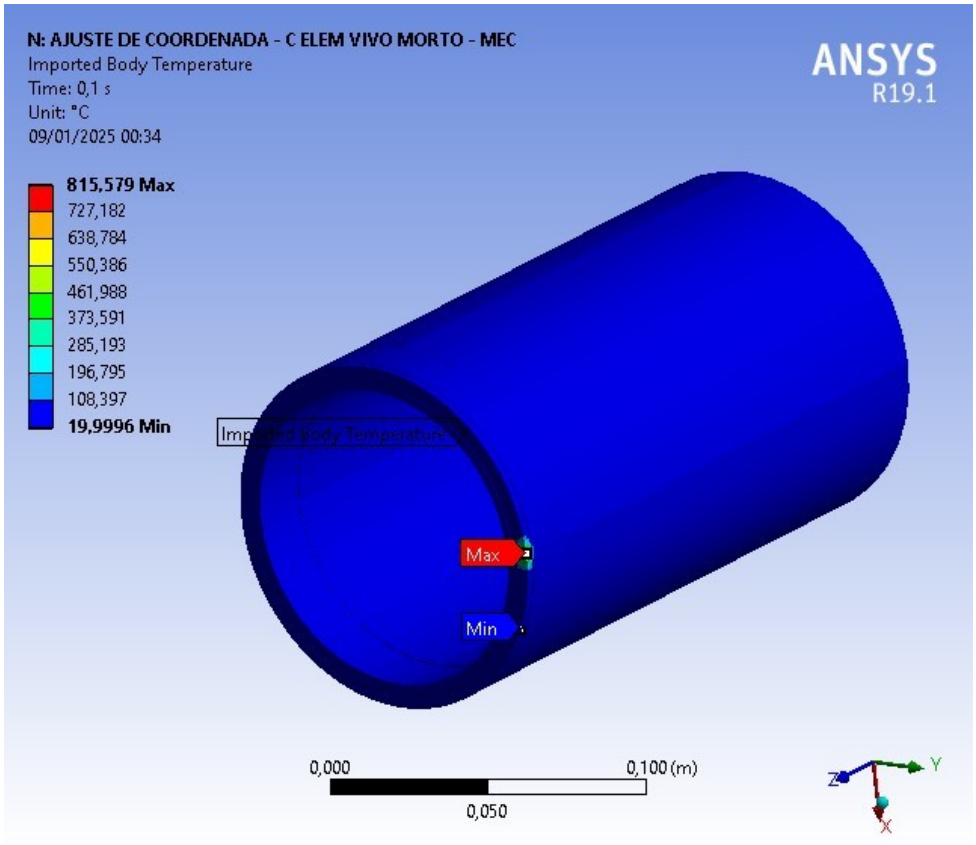

Source: Prepared by the author.

3.3.2.4 Element birth and death technique

In addition to all the points mentioned earlier, it is important to highlight the use of the element birth and death technique, which is available as an element activation tool in specific mesh during the ANSYS simulations.

In this work, therefore, both thermal and mechanical analyses were performed using this tool, summarized in Table 2, presented below.

Table 2 – Tests performed with and without the use of the element birth and death technique.

Analysis Type	Element Birth and Death Technique	Mesh Element Order	Test Index
Thermal Analysis	With EBDT	Linear Mesh	1
	Without EBDT	Linear Mesh	2
Mechanical Analysis	With EBDT	Linear Mesh	3
		Quadratic Mesh	4
	Without EBDT	Linear Mesh	5
		Quadratic Mesh	6

Source: Prepared by the author.

Thus, six tests were conducted, detailed as follows: for the thermal analysis, tests were performed both with and without the element birth and death technique, using only linear elements, due to computational problems encountered during the execution of the test with quadratic order elements, such as high fluctuations in the initial time steps including the inclusion of negative values (Versteeg; Malalasekra, 2007); for the mechanical analysis, tests were conducted with and without the element birth and death technique, considering linear and quadratic elements, with the goal of more comprehensively analyzing the residual stresses and radial displacements found at the end of the test. Regarding the configuration of the technique, it can be observed in Figure 35 the highlighted representation of the inactive element mesh, which is absent from the part at the beginning of the test, with the aim of making the test more representative of the experimental model, as the weld bead is created during the welding process.

Figure 35 – Representation of the element birth and death technique in ANSYS program.

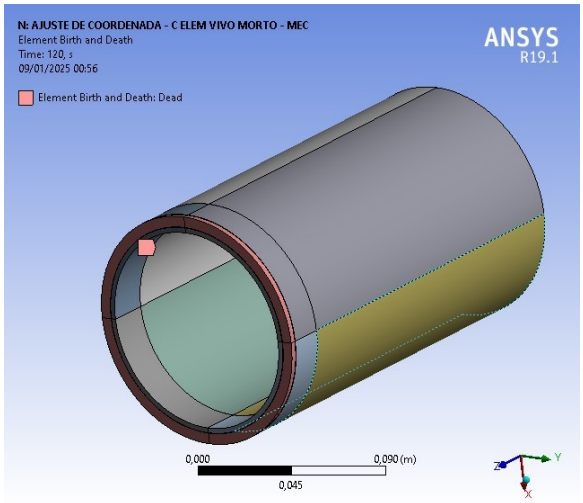

Source: Prepared by the author.

In addition, the activation of these elements during the passage of the heat source was implemented in the APDL code. As illustrated in Figure 36, which is also available in Appendix B, the element is activated only when heat is being exerted by the source, and not when the source passes through each fraction of the total perimeter of the tube, using the EALIVE function.

Figure 36 – Region of the APDL code highlighting the activation of elements through the element birth and death technique.

```
*IF,QLB,GE,QLB2,THEN
        EALIVE,JJ
*ENDIF
```

Source: Prepared by the author.

4 RESULTS AND DISCUSSIONS

4.1 Butt Welding in a Semi-Infinite Domain

The following Table 3 shows the computational times for cases 1, 2, and 3, all thermal without EBDT, with cf = 6 mm, cr = 24 mm, ff = 0.4 and fr = 1.6 in case 1; cf = 15 mm, cr = 15 mm, ff = 1.0 and fr = 1.0 in case 2; and cf = 24 mm, cr = 6 mm, ff = 1.6 and fr = 0.4 in case 3. It can be seen that each test took on average 8 and a half hours, with a total of approximately 26 hours of testing.

Table 3 – Computational times for cases 1, 2, and 3 in the semi-infinite domain.

Test Case	Elapsed time (in sec)	Elapsed time (h)
Case A	31093	8.6
Case B	30815	8.6
Case C	30872	8.6

Source: Prepared by the author.

The extended duration of the test period shown in Table 3 for each test was due to the use of quadratic tetrahedral elements during the mesh creation for the part, in addition to the refinement of the edge where the heat source acted in a single pass, so the testing time was significantly high for all cases. However, even with the goal of evaluating the heat source algorithm through the APDL language and temperature profiles for each case, which will be shown below, there was an excessive delay in obtaining the results. In this situation, a less refined mesh with fewer elements and nodes, or the use of structured mesh elements, such as hexahedra, would make the tests more computationally efficient while ensuring similar thermal results.

Regarding the results obtained, after conducting the thermal tests described in Section 3.1.2, the present work compares the temperature gradient between cases 1, 2, and 3 at a specific point in the domain, from the start of the heat source pass, alongside previous works using different numerical methods and analytical solutions.

As shown in Figure 14, the heat source begins the welding process at point O, which is the origin of the Cartesian coordinate system (0,0,0), and advances 100 mm, passing through point P (0,0,50), and finishing the welding at point F (0,0,100). The average speed of

the source is 5 mm/s, constant along the entire profile. Similar to Rocha's (2022) work, a time step of 0.05s was adopted, which can also be seen the results in Appendix A at the end of this work.

In Figure 37, the thermal cycles for cases 1, 2, and 3 are observed, comparing the analytical method from Fachinotti's (2011) work and the numerical method of EbFVM from Rocha (2022) using an unstructured grid with linear element order, with the temperature profile along the weld bead at 10 seconds, 50 mm from the start of the welding application.

Figure 37 - Thermal cycles for different heat source geometry parameters in the middle of welding path for cases A, B and C, comparing FEM and EbFVM results.

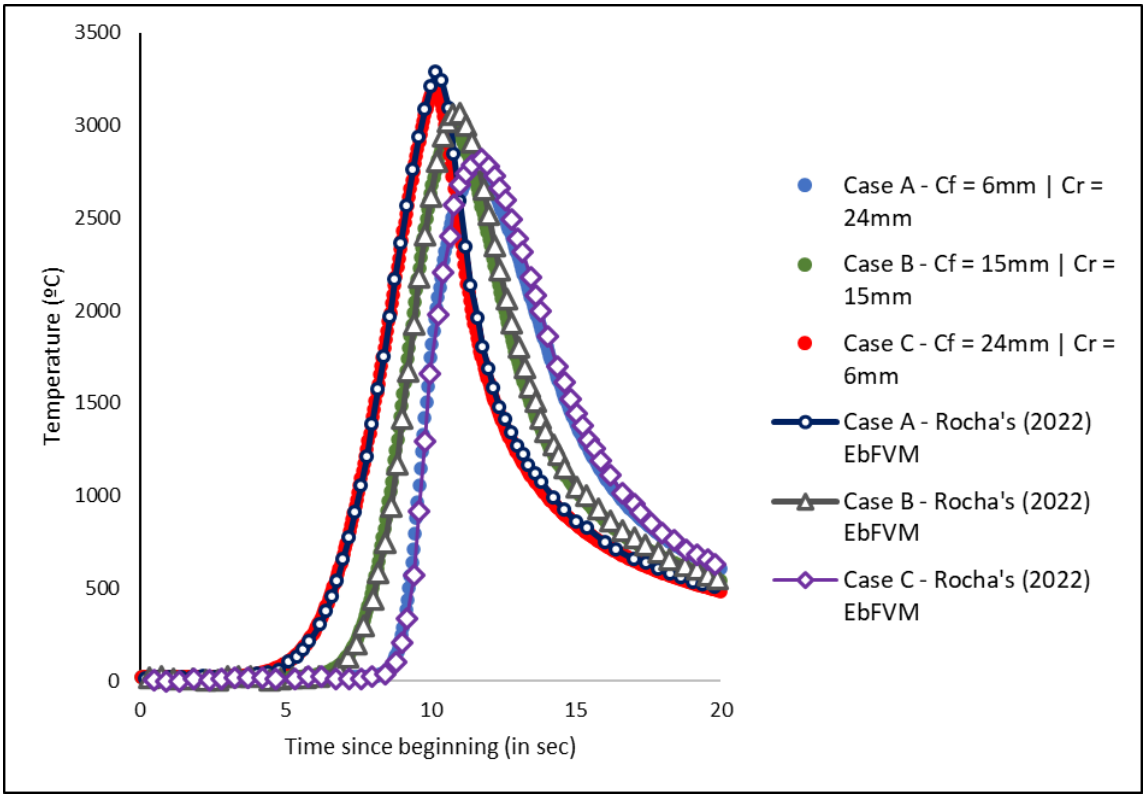

Source: Prepared by the author and adapted from Rocha (2022).

The results obtained in the present study show good agreement with those reported by Fachinotti (2011), who employed an analytical solution, and Rocha (2022), who used the Element-based Finite Volume Method (EbFVM), thereby supporting and validating the findings of previous studies. The thermal cycle with the highest temperature occurs in the double-ellipsoidal model, in the heat fraction with the cf dimension of 24 mm and cr of 6 mm, with the temperature peaking at approximately 3200 °C, corresponding to the graph with red

points. The thermal cycle with the lowest temperature occurs in the reverse profile, with the front dimension of 6 mm and rear dimension of 24 mm, reaching a maximum temperature of approximately 2700 °C, corresponding to the graph with blue points.

It can also be observed, in Figure 38, a better visualization of the molten zone, through the top view on the XY plane. Therefore, by analyzing the thermal profile behavior of the heat source, it is possible to observe the heating tendency caused by the front region, while the cooling of the molten zone is evident at the sides and posterior region, with a consequent heat loss.

Figure 38 – Advancement of the heat source in case 2, with a constant speed of 5 mm/s and its respective temperature distributions, for the following moments: (a) 0.05s, (b) 5s, (c) 10s, (d) 15s, and (e) 20s.

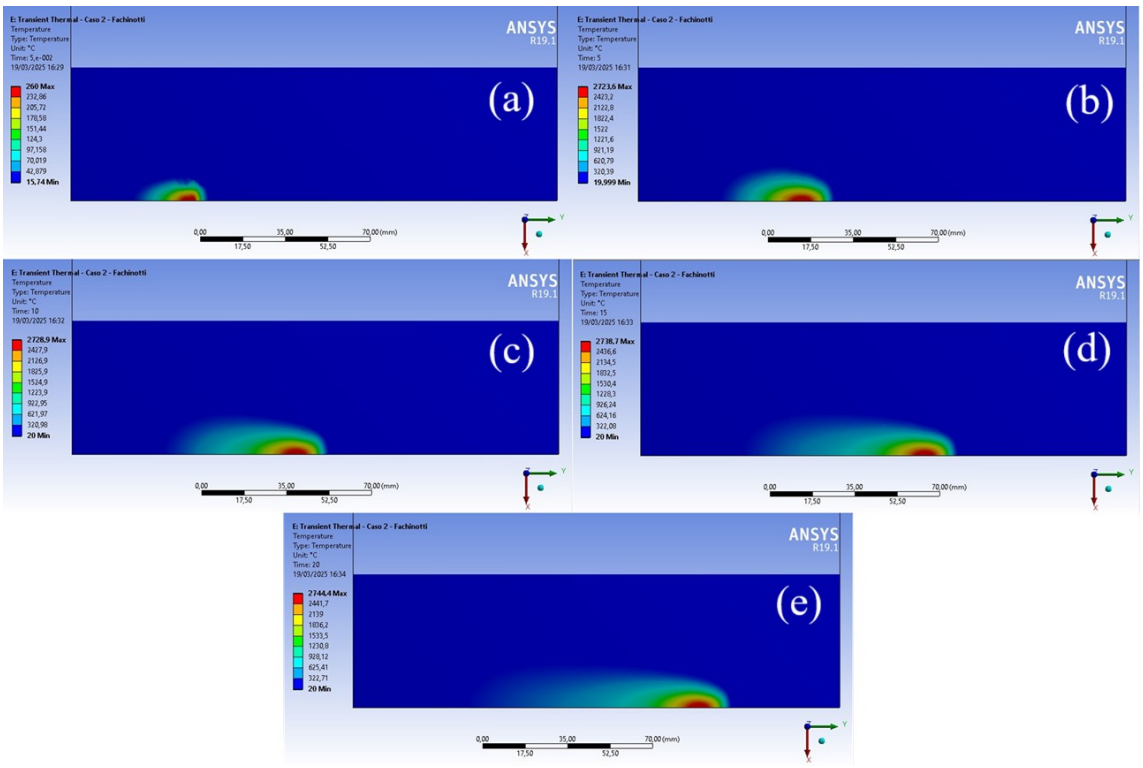

Source: Prepared by the author.

The main objective of this analysis is, therefore, the validation of the APDL code developed for the semi-infinite domain plate, by utilizing previously published and accepted works in the literature, with a high temperature gradient that could capture the precision of the results in the critical regions. Thus, the developed APDL code is capable of accurately representing the welding process through a Gaussian heat source, with its respective

dimensional variations. With this, we can proceed with the thermo-mechanical analysis and seek to validate the developed code, now for the tubes.

4.2 Butt Welding with Single Pass on Tube and Filler Metal

4.2.1 Thermal Analysis

Figure 39 presents the temperature field on the tube at the initial stage of testing, at every 90º rotation of the heat source, and at the end of the test, using the element birth and death technique. At the initial moment, at 0.1s, it is observed that due to the heat flux flowing backward from the start of the material creation and the welding path by the heat source, the adjacent regions of the end of the V-groove heat up, and consequently, their elements are activated by the computational technique. Initially, it is observed that the tube reaches a peak temperature of approximately 874 ºC, and throughout the entire path, the entire molten pool region and adjacent regions to the weld bead and the beginning of the heat-affected zone reach temperatures above 1500 ºC. Therefore, it can be concluded that the entire region has steel in a liquid state with low flow stresses, as can be corroborated by Figure 16. The maximum temperature on the inner surface, at a distance of 8 mm from the end of the weld, is around 900 ºC, differing from Karlsson and Josefson (1990), who mention that in this region, the temperature exceeds 1000 ºC. In this case, the divergence can be attributed to the author's use of a coarse mesh consisting of 420 20-node solid elements.

In approximately 60s, the elements of the previously heated weld bead are reheated again, and by the end of the test at 120s, the cooling temperature reached is 220 ºC, which corroborates the results obtained by Karlsson and Josefson (1990).

Figure 40 shows the temperature field, obtained by applying a cross-sectional cut through the middle of the tube to better represent the temperature distribution at a 90º angle. For better visualization, two situations are presented: in the first, the creation of material in the weld bead is observed, with the mesh elements being created, highlighting the mesh refinement in the regions of the weld bead and the heat-affected zone; and in the second situation, the thermal profile during the heat source's passage is simplified, with the temperatures obtained at the axial and longitudinal ends of the tube. The main objective here is to facilitate the understanding of the adopted technique with a clear and precise visualization of how the test is performed, and emphasize that, during the heat source passage,

the entire molten pool region consists of steel in the liquid state, as highlighted in the red and orange areas of the isotherm.

Figure 39 – Movement of the heat source at the initial test moment (a), at 90º angles (b), 180º (c), 270º (d), 360º (e), and at the final test moment at 120s (f).

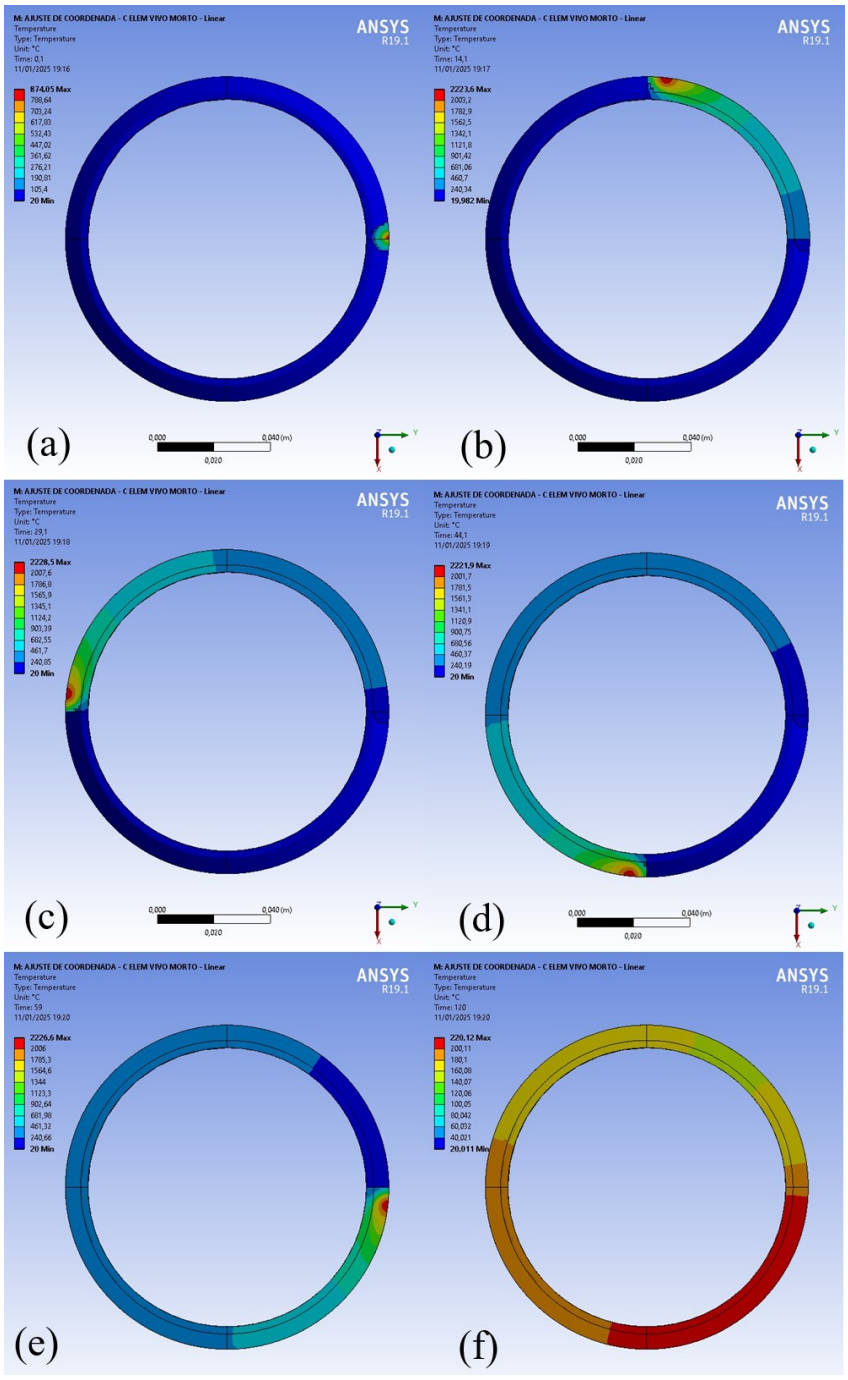

Source: Prepared by the author.

Figure 40 – Representation at 90º from the start of the heat source application, showing the weld bead with mesh elements (on the left), and in a simplified manner (on the right).

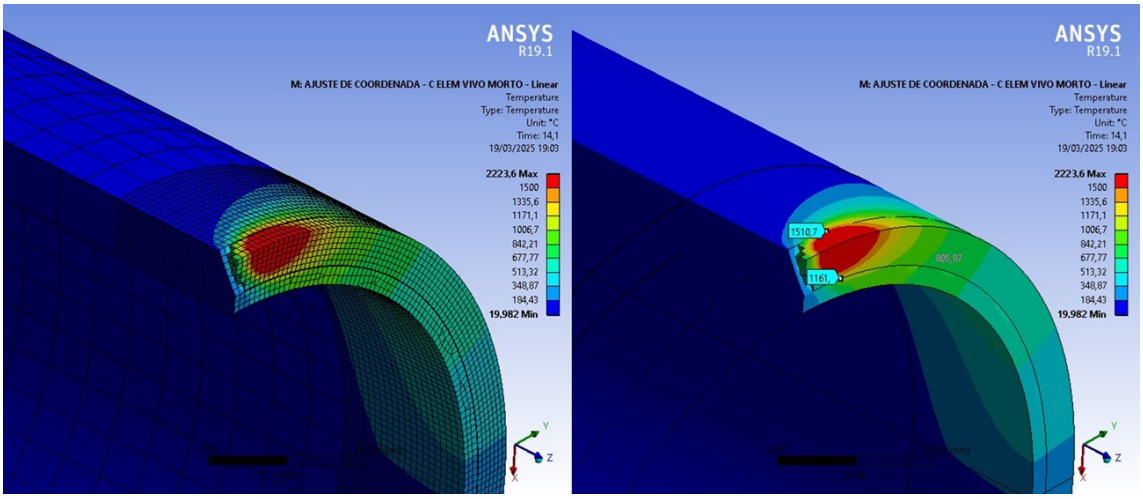

Source: Prepared by the author.

It is emphasized that initially, the material used, in this case, carbon-manganese steel (SIS 2172), has distinct specific heat in the weld bead region (up to 3mm distance from the cross-section) and in the heat-affected zone (up to 20mm distance from the cross-section), compared to the rest of the tube, based on the thermal properties presented in Figures 14 and 25, as shown in Figure 40. Therefore, the two regions were given refined meshes with element sizes of 1mm. For the rest of the tube, a coarser mesh was used (with element size of 10mm). Since temperature, stress, and displacement do not vary considerably in the analysis, a coarser mesh was preferred in the region far from the weld bead. Specifically analyzing the weld bead profile, the dimension in the transverse direction of the bead (the z-axis of the tube, as shown in Figure 34) is 3.0mm, and the dimension in the radial direction of the bead (the x-axis of the tube) is 5.5mm.

In Figure 41, the temperature profile on the outer surface after the heat source passes through the tube at various moments can be visualized. The reference used for this analysis is an angle of 150º after the front of the heat source has passed, therefore, 24.1s from the start of the welding process, considering the welding speed of 6mm/s. From this point, the analysis was carried out transversely through a distance of 20 mm from the center of the weld bead. The aim is to visualize the behavior of the temperature gradient at the following points: weld bead, heat-affected zone, and part of the remaining tube.

Figure 41 – Temperature profiles on the outer surface of the tube at an angle of 150º at various moments after the passage of the heat source front.

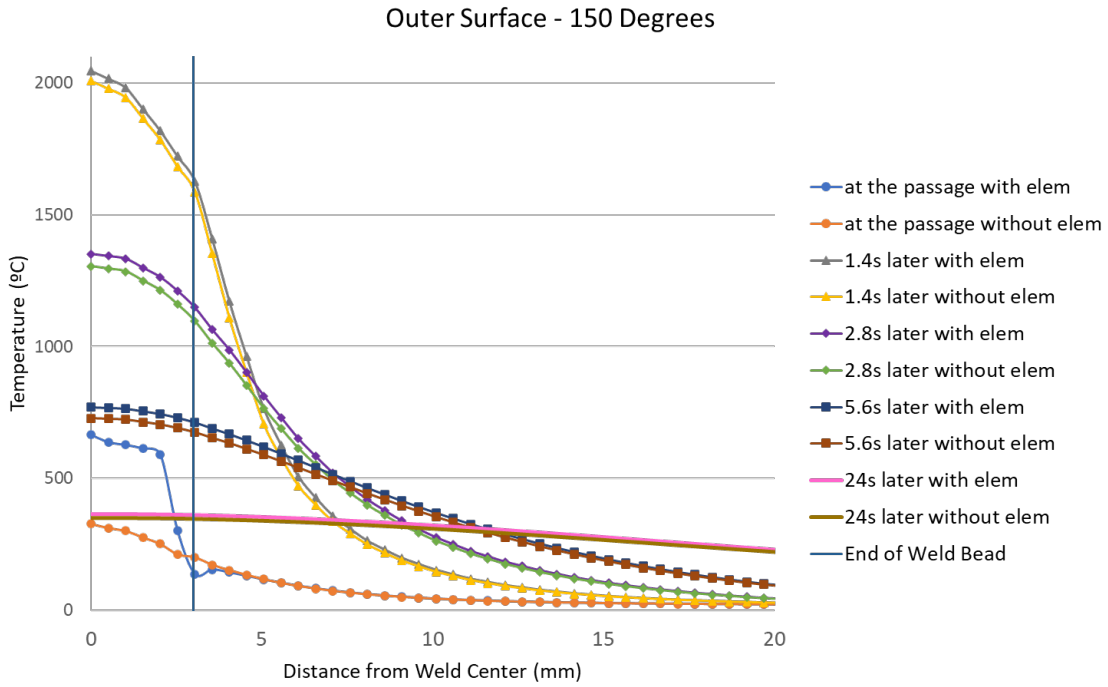

Source: Prepared by the author.

Therefore, in Figure 41, for comparison purposes, two experiments were conducted, with and without the use of the "live-dead element" technique. The goal is to understand the behavior of the temperature during the passage of the heat source front in the V-groove, delimited in the graph by the 3mm vertical line from the start of the weld bead, and around the heat-affected zone, comparing the two methods. Since the mesh is refined in the regions of the weld bead and heat-affected zone, the analysis on the x-axis was collected up to 20mm from the center of the weld bead. It can be observed that, for all the moments after the heat source reaches the 150º reference (after 1.4s, 2.8s, 5.6s, and 24s), the temperature profile is slightly higher with the addition of material at each incremental time step. At the moment t + 24s, a small difference between the temperature profiles for both methods is observed, approximately 20 ºC, and the temperature in the tube at the weld bead and heat-affected zone experiences little variation in the axial direction. In the initial phase of the heat source passage, represented by the dashed blue line (with EBDT elements) and the dashed orange line (without EBDT elements), when the heat source front starts the heating process of the region, a significant difference between the two methods and their respective temperatures is noticeable, with 665ºC using the element birth and death technique and 327ºC without this

tool. In the work of Karlsson and Josefson (1990), this higher variation in the temperature curve during the heat source passage is also presented, but no comparison with experimental values is provided, and the simulations were performed exclusively using EBDT. Finally, it can also be observed that, after the weld bead profile, delimited by the vertical line on the graph at 3mm, the temperature profiles are similar, and there are no significant divergences.

Additionally, Figure 42 shows the temperature profile, comparing the results obtained with the element birth and death technique by the Finite Element Method (FEM), and the results obtained by Rocha (2022) using the Element-Based Finite Volume Method (EbFVM) without EBDT. According to Lima et al. (2022), the EbFVM method combines the advantages of both Finite Element and Finite Volume methods, proving effective in applications involving welding processes. From this figure, it can be observed that there is excellent agreement between the two methods, even when involving calculations with different numerical procedures.

Figure 42 – Temperature profiles on the outer surface of the tube at an angle of 150º at various moments after the passage of the heat source front, comparing the FEM method with live-dead element and EbFVM.

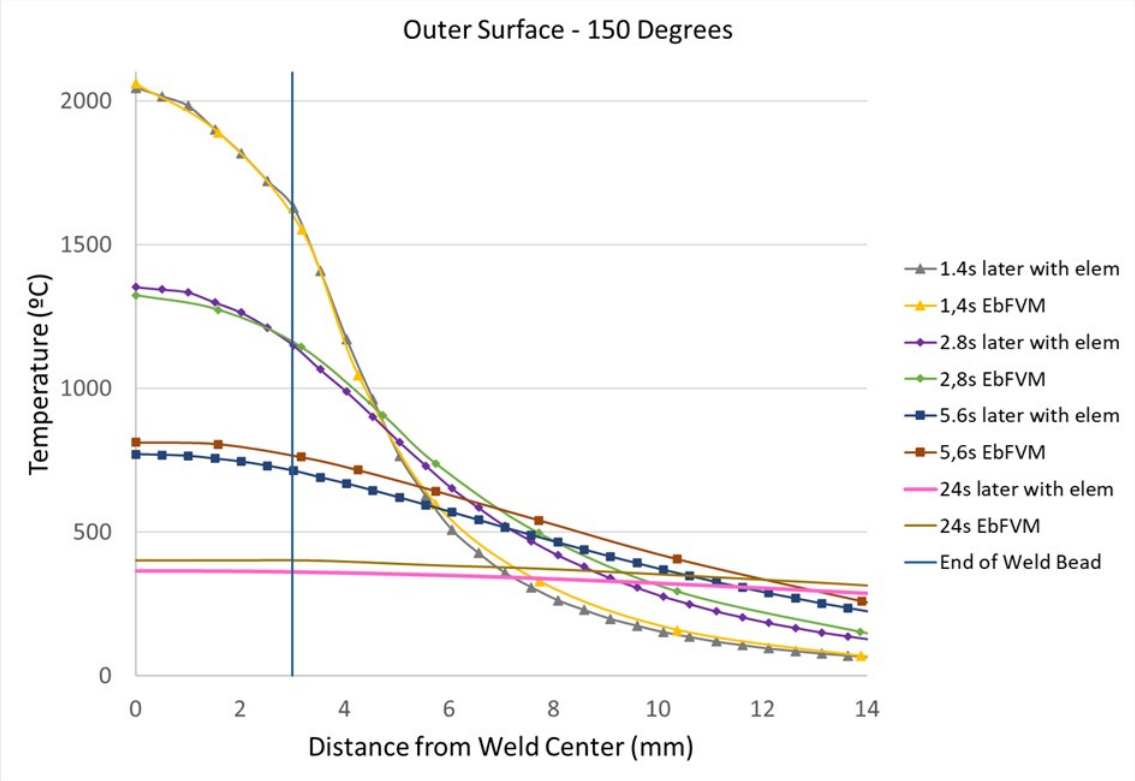

Source: Prepared by the author and adapted from Rocha (2022).

Figure 43 below shows how the temperature behaves during the passage of the heat source with and without the element birth and death technique. It can be observed that, in the upper profile of the figure, the elements are activated instantly as the heat reaches the region, while in the lower profile, all elements are already activated, resulting in a more homogeneous behavior.

Figure 43 – Temperature fields, with live-dead element (above) and without live-dead element (below), at the time step of 24.1s after the start of the welding process.

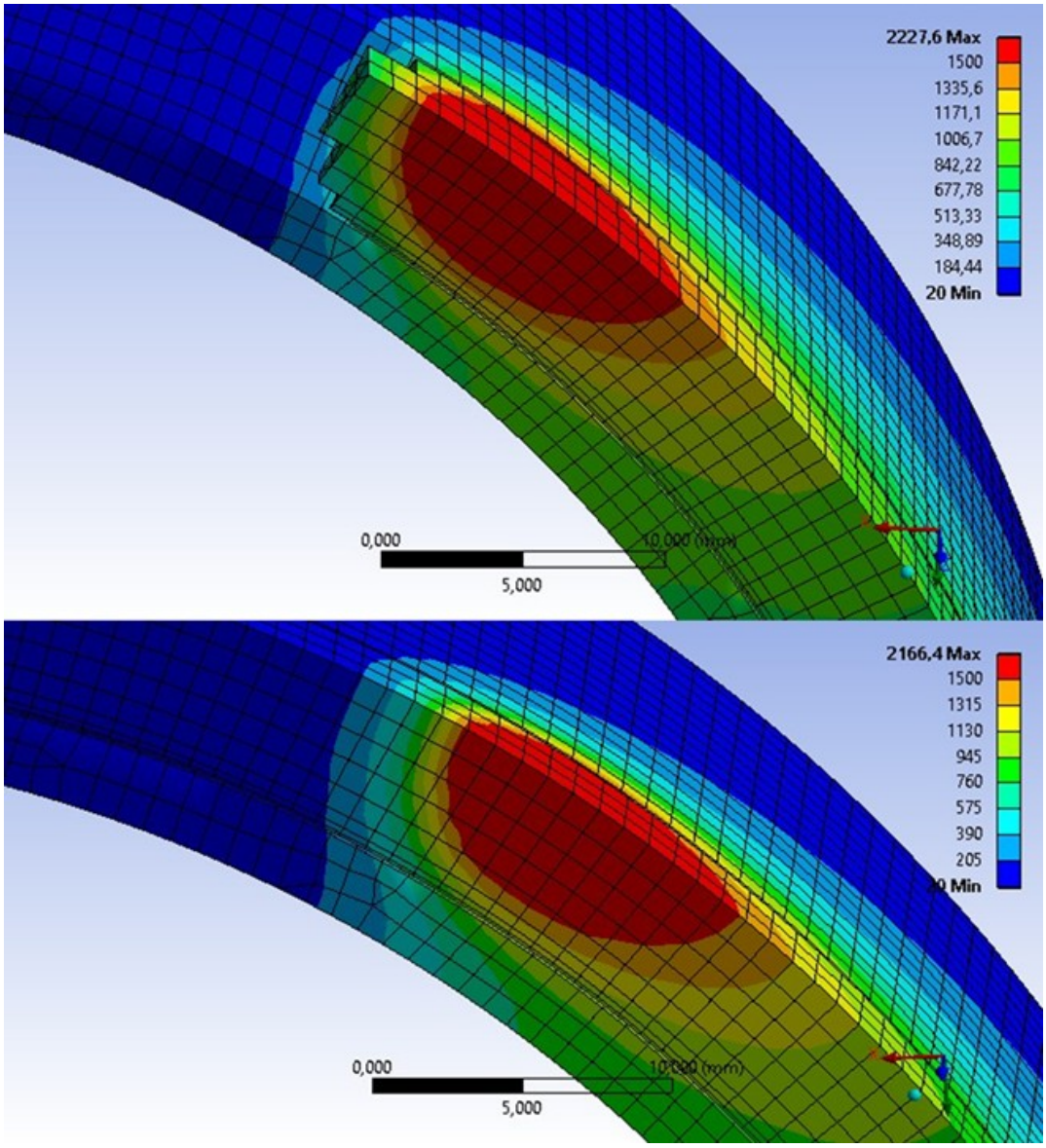

Source: Prepared by the author.

Therefore, this difference occurs because, in the element birth and death technique, the amount of energy deposited is greater in proportion to the number of active elements in the same region when compared to the conventional method, since the latter assumes that all elements are already active. As shown in Figure 43, in the upper profile, each active mesh element has a temperature value of approximately 600ºC and in the inactive regions, there's no temperature, since the heat source has not yet reached these regions.

Thus, it can be observed that the implementation of the method produces similar results when compared to the traditional technique, except during the heat source passage, an aspect that requires further investigation. These results are also important for the subsequent mechanical analysis, which will be discussed next.

4.2.2 Mechanical Analysis

After obtaining the results from the thermal analysis, where temperature values were collected from tests with and without the element birth and death technique, these data were stored in the Ansys software and incorporated as boundary conditions for the mechanical analysis. For the mechanical analysis, four tests were conducted: with and without the element birth and death technique, varying between linear and quadratic order elements in the generated mesh.

4.2.2.1 Radial displacements

Similarly to the thermal analysis, conducted at an angle of 150° from the onset of heat source application, the mechanical analysis is illustrated in Figures 44 and 45, which initially present different radial displacement values obtained at a distance of 20 mm from the weld centerline. These two figures aim to enhance data comprehension, considering the variations in time steps and the defined testing conditions.

Figure 44 – Radial displacements calculated at 150° on the external surface at the moment of heat source application (top) and 3 seconds thereafter (bottom).

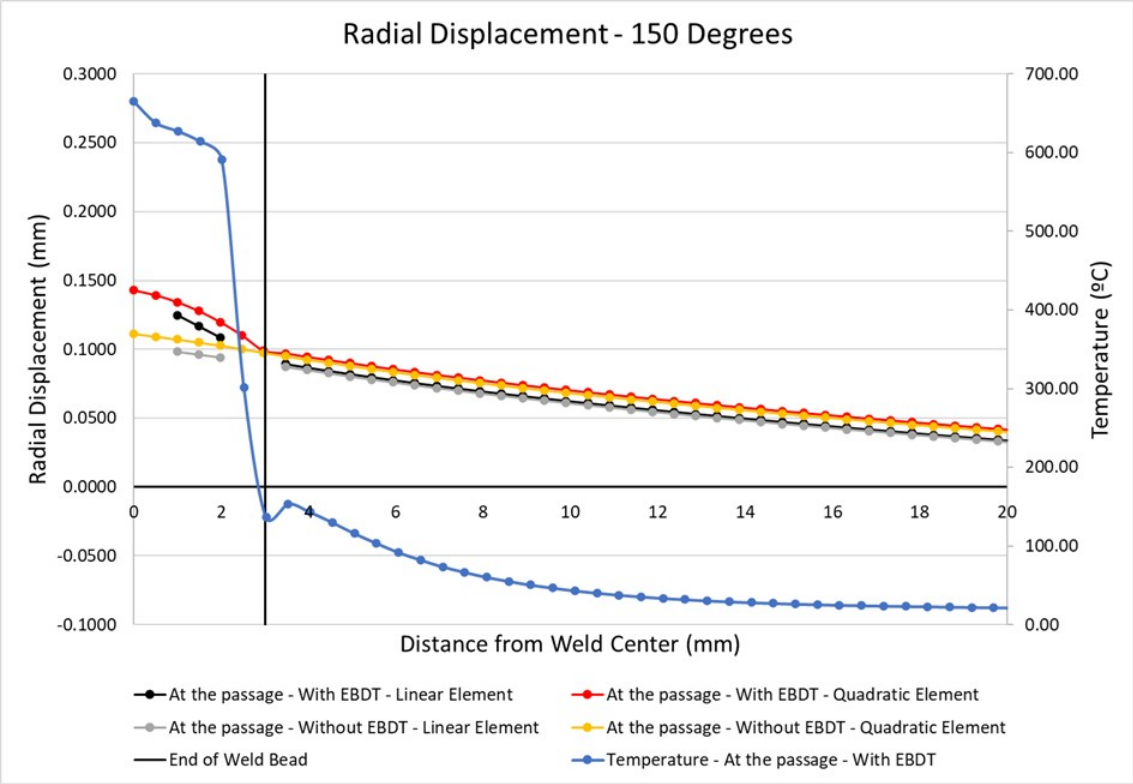

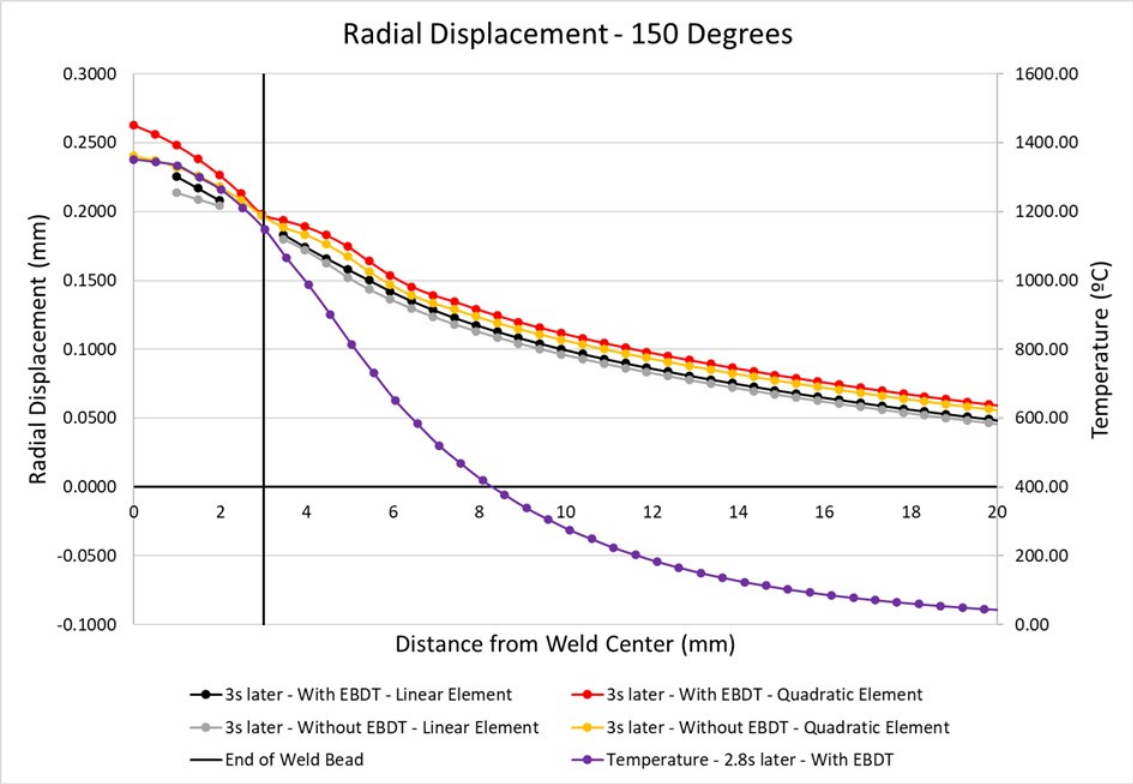

Source: Prepared by the author.

From Figure 44, it can be observed that at high temperatures, thermal expansion occurs in the tube wall thickness near the weld bead and the heat-affected zone (HAZ). After the solidification of the weld bead, a contraction in thickness begins, leading to an increase in displacement in the HAZ region. This phenomenon arises due to the plastic deformation of the weld caused by heating in the vicinity of the base metal, which expands axially from the weld pool to the HAZ. As for the effect of the different meshes used, few variations are observed among the results, with a slight divergence only in the weld bead region, due to the high temperature gradient in the initial time intervals (with temperatures approximately 1350 ºC after 3 seconds the heat source has passed through).

In Figure 45, the displacement expansion observed throughout the HAZ profile is smaller after 24 seconds (approximately 400°C) and larger after 60 seconds (approximately 250°C). This suggests a positive effect of volumetric expansion associated with the final phase transformation, which occurs within this temperature range in the most heated areas of the welded region. In Figure 46, after 120 seconds, in the residual state, negative radial displacements are observed throughout the weld bead up to the middle of the HAZ, accompanied by the contraction of the entire axial profile compared to the state after 60 seconds.

Figure 45 - Radial displacements calculated at 150° on the external surface 24 seconds (top) and 60 seconds after the heat source passage (bottom).

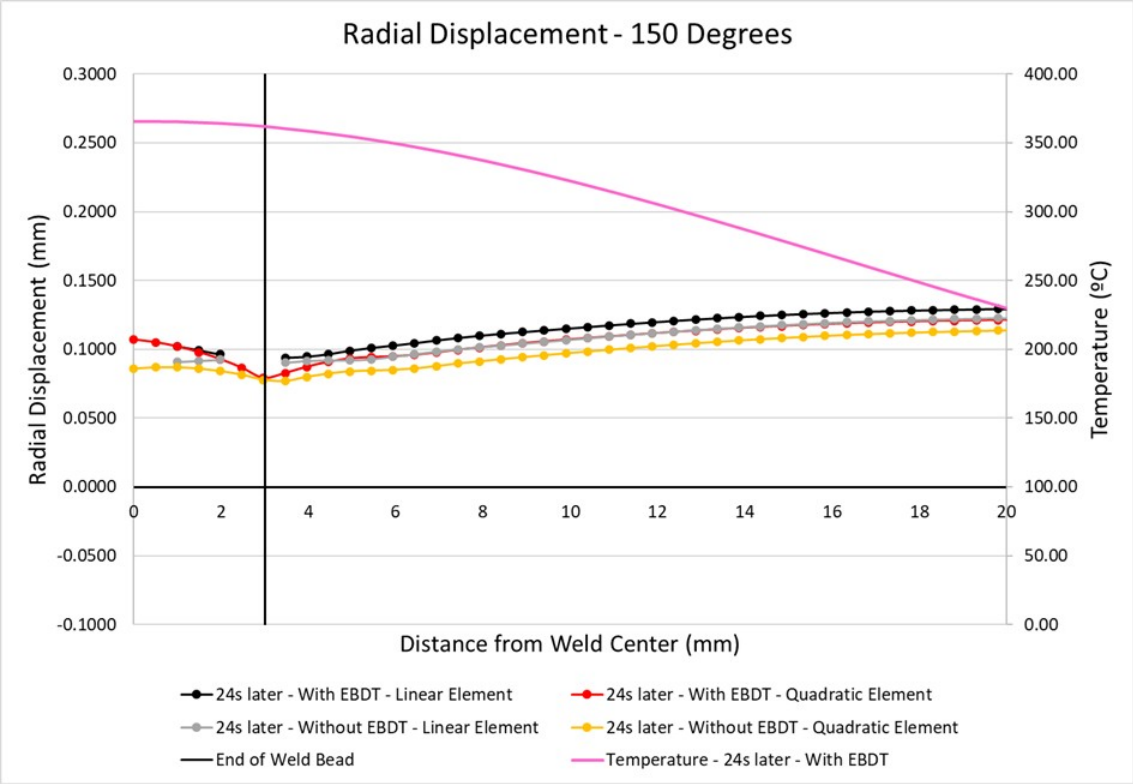

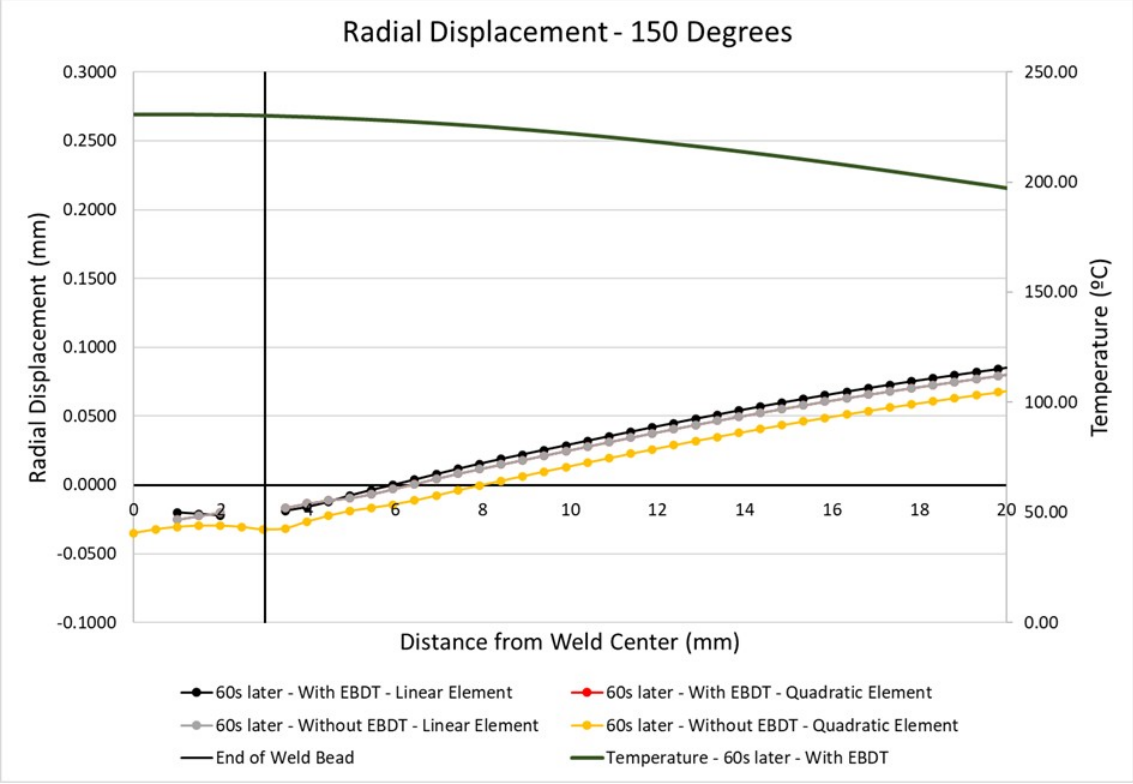

Source: Prepared by the author.

Figure 46 – Radial displacements calculated at 150º on the external surface at the end of the test (120s).

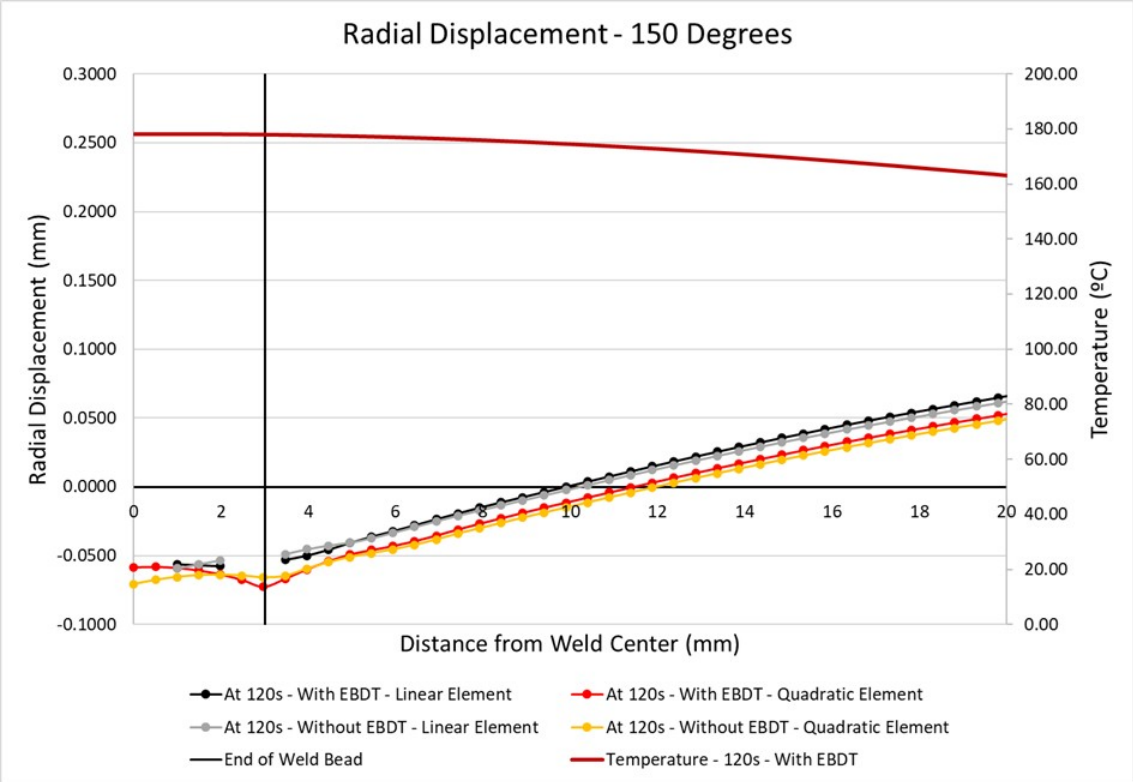

Source: Prepared by the author.

Regarding the analysis of the various methods employed, a consistent agreement between the results is observed. For all time steps, the combination of the element birth and death technique with a quadratic order element yields higher values compared to the other methods. As seen in the thermal analysis, where the deposited heat is concentrated solely in the active elements of the weld bead and the adjacent HAZ, the temperature in these elements is consequently higher, resulting in greater radial expansion in this region.

Furthermore, even when adopting a coarser mesh in the tests with quadratic element profiles, the results were satisfactory and consistent with those of the other methods. At the moment of heat source application, the HAZ exhibits closely aligned radial displacement values, showing minimal differences between tests performed with and without EBDT. This is a positive indication for the use of meshes of such order in structural analyses, demonstrating that tests can be performed with less refined meshes but with more nodes concentrated in the key regions to be analyzed, thereby reducing computational time—a point that will be highlighted at the conclusion of the results.

4.2.2.2 Axial stresses

Initially, Figure 47 presents the axial stress profiles on the external surface at an angle of 150° at various time intervals following the passage of the heat source. For lengths beyond 20 mm, the tube's mesh becomes coarser, leading to less precise data. Consequently, the primary focus of the analysis is concentrated on the weld bead and the heat-affected zone (HAZ), where the mesh refinement is greater.

At the moment the heat source passes through the region, the temperature rises significantly, reaching approximately 700ºC at the passage of the heat source and 2000°C after 1.4 seconds, according to Figure 41. In this high-temperature region, the material has low yield strength due to thermal softening, according to Figure 16, and is only able to withstand low stresses, which is consistent with the behavior of the steel at high temperatures, where its mechanical strength decreases dramatically. Compressive stresses are generated at the end of the weld bead and the beginning of the HAZ due to the high temperature gradient in this region, as shown in Figure 42. High-temperature gradients indicate that the material's strength increases rapidly to its ambient temperature value over a short distance from the weld pool. In Figure 42, it is evident that the temperature at the center of the weld pool ranges from approximately 2000°C at the center of the bead to 1600°C at the start of the HAZ, which can be identified from the vertical line positioned 3 mm from the center of the weld bead.

In the region behind the heat source, there is a gradual decrease in temperature as the weld bead cools. This cooling process, along with the solidification and contraction of the weld pool, contributes to the formation of residual stresses in the HAZ. Therefore, in Figure 47, this behavior can be observed, with low axial stresses in the HAZ during the heat source passage. Following the tube's cooling at time intervals of 24 seconds, 60 seconds, and 120 seconds, as shown in Figures 49 to 51, the entire HAZ region experiences residual tensile stresses.

Figure 47 – Axial stresses calculated on the external surface at 150° at the passage of the heat source.

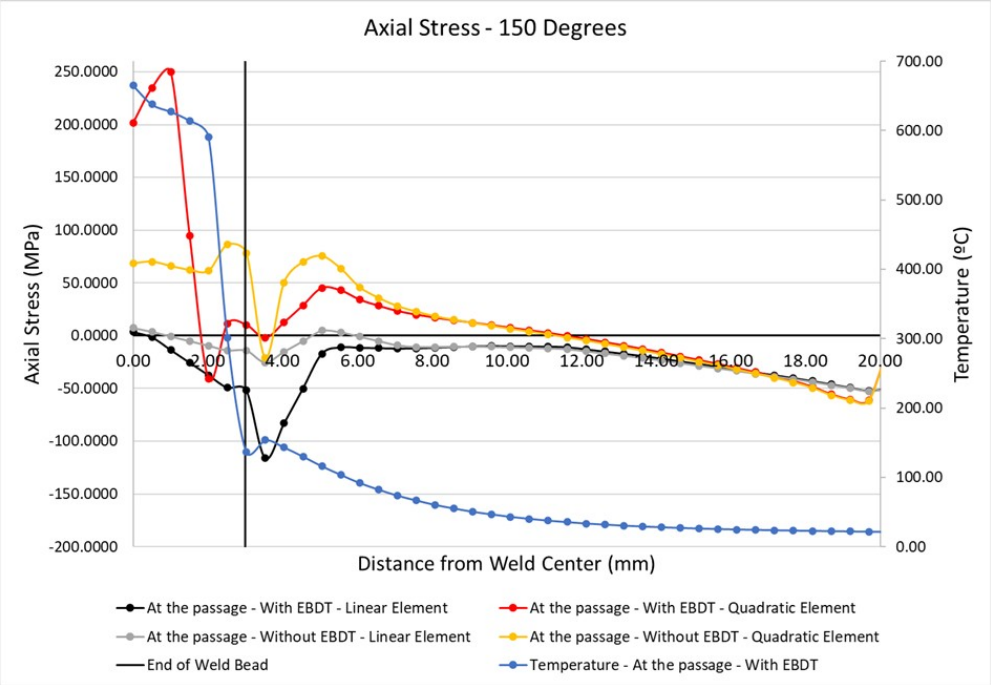

Source: Prepared by the author.

Figure 48 – Axial stresses calculated on the external surface at 150º after 6 seconds the passage of the heat source.

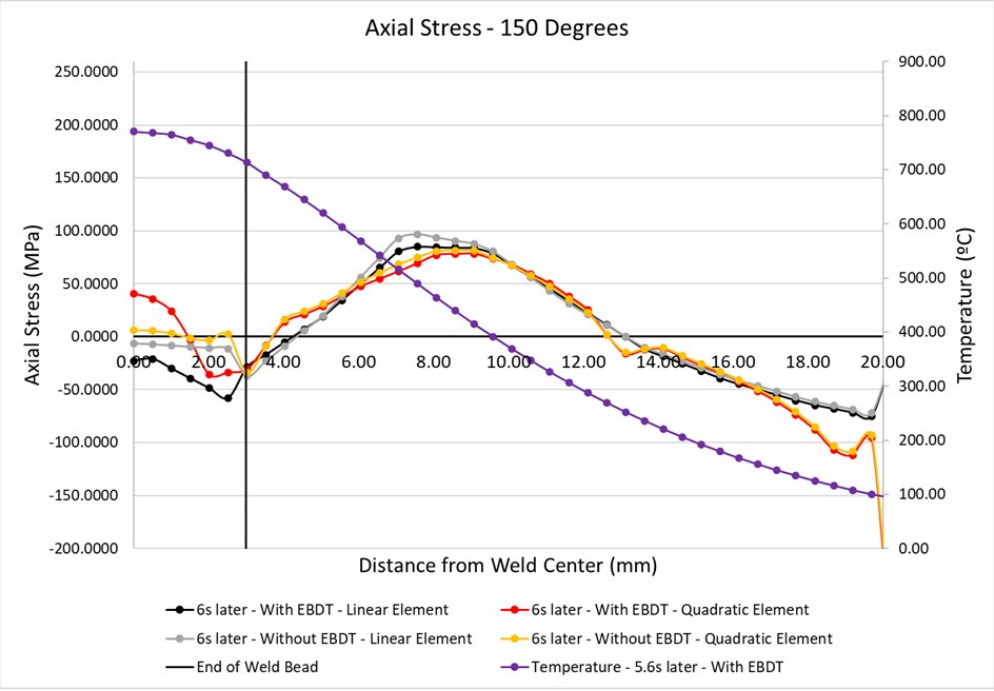

Source: Prepared by the author.

Figure 49 - Axial stresses calculated on the external surface at 150º after 24 seconds the passage of the heat source.

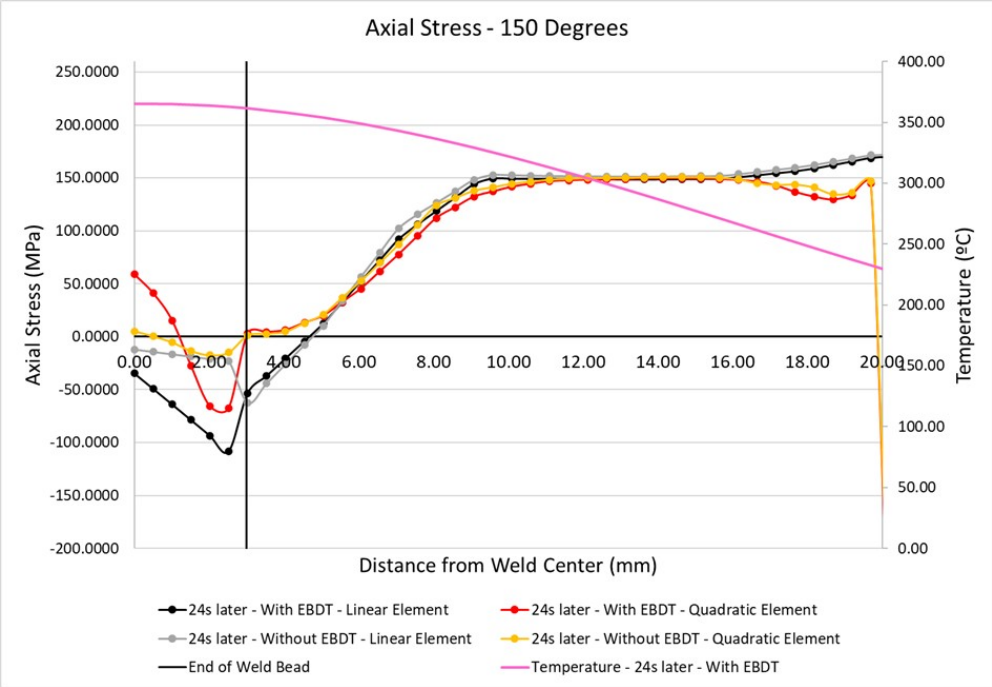

Source: Prepared by the author.

Figure 50 - Axial stresses calculated on the external surface at 150º after 60 seconds the 0passage of the heat source.

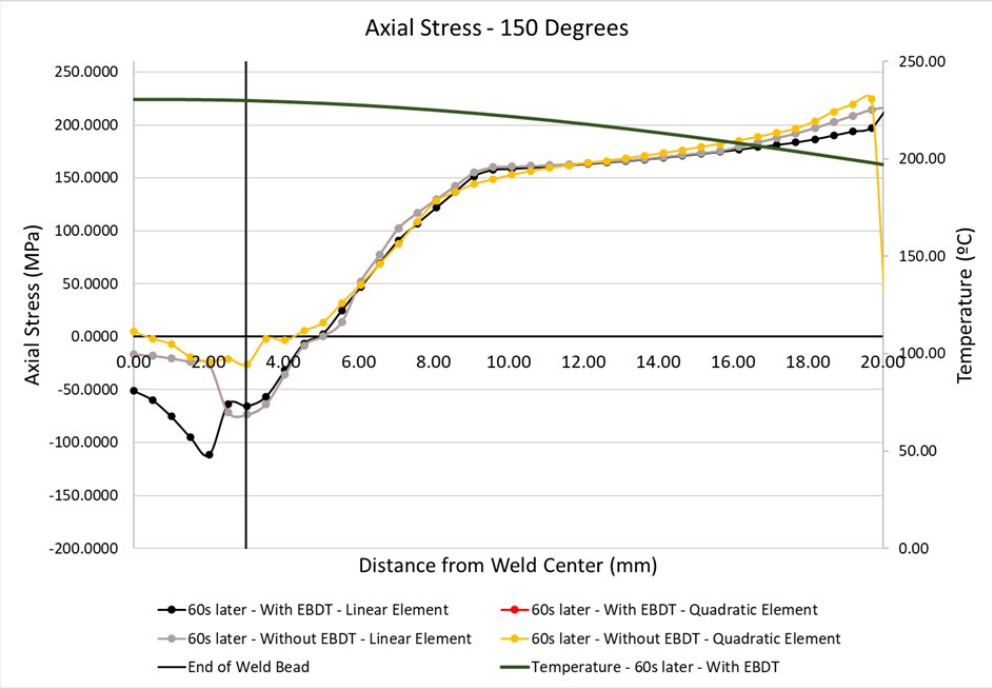

Source: Prepared by the author.

Figure 51 - Axial stresses calculated on the external surface at 150º at the end of the test (120s).

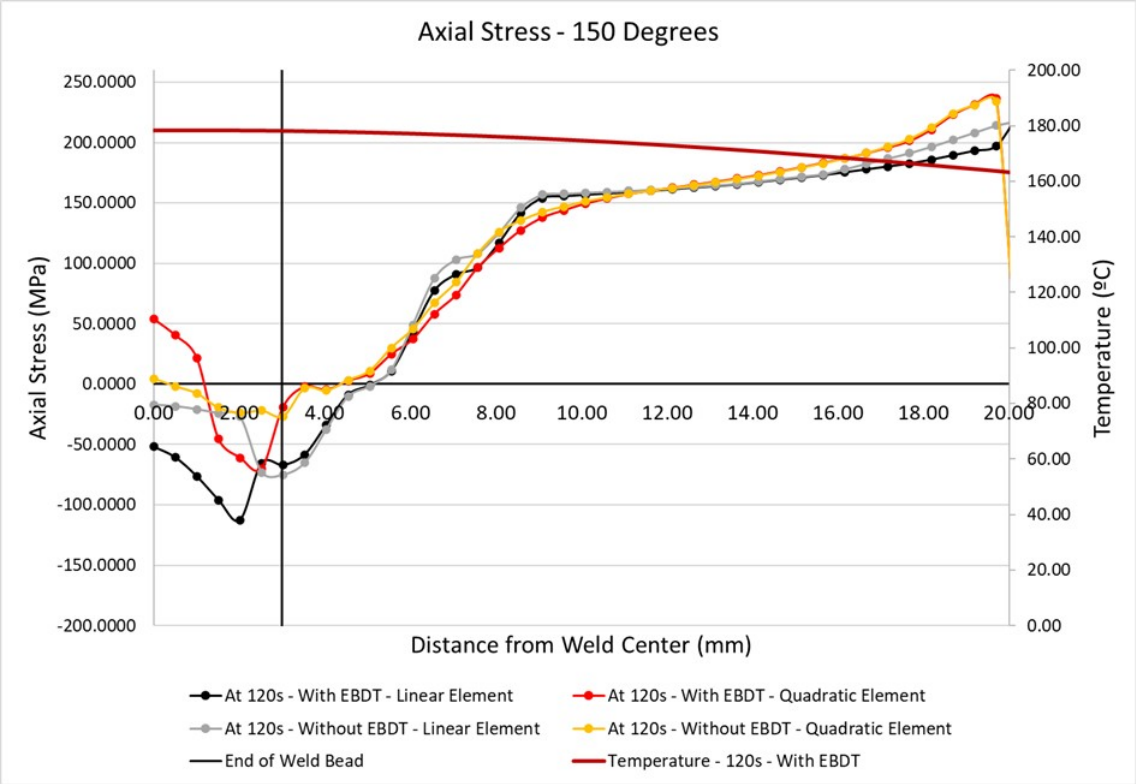

Source: Prepared by the author.

Regarding the methods used, Figures 47 to 51 show good agreement in the results for the axial stresses for all the methods used. In the weld bead region, at the moment of heat source application, a considerable variation in the observed stresses can be noted, indicating lower result accuracy at very high temperatures. After the weld bead cools, the axial stress profiles in this region are similar, displaying initial compressive stresses and tensile stresses throughout the heat-affected zone (HAZ).

For the 0° angle, the behavior of axial stresses differs. In Figures 52 to 56, the values obtained at various intervals after the heat source passage are also presented. The 0° location represents the starting and ending point of the welding process. It is observed that the residual stress curve at this position differs from the residual stresses at a 150° angle. Additionally, the magnitude of the residual stresses at the starting position is lower than in other regions.

The reduction in residual stresses at this specific point is due to reheating when the heat source finishes at this location, occurring at t = 60 seconds. In Figure 46, at 60 seconds after the start of heat source application, and during the final heating of the region as

the process concludes, it is observed that, except for the curve representing a quadratic element without EBDT, there was a characteristic contraction of stresses in the HAZ. For other analyzed angles, this configuration does not occur, requiring further investigation of axial stresses in the HAZ for multipass welds.

Figure 52 - Axial stresses calculated on the external surface at 0° at the passage of the heat source.

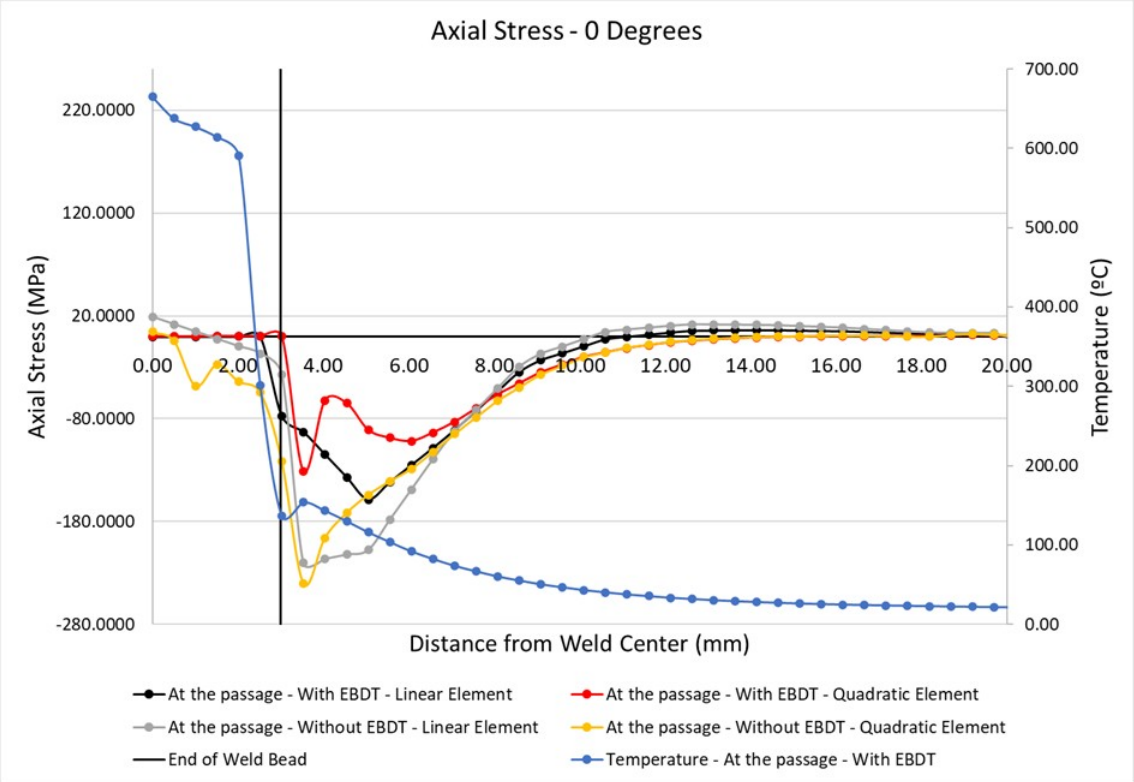

Source: Prepared by the author.

Figure 53 - Axial stresses calculated on the external surface at 0° after 6 seconds the passage of the heat source.

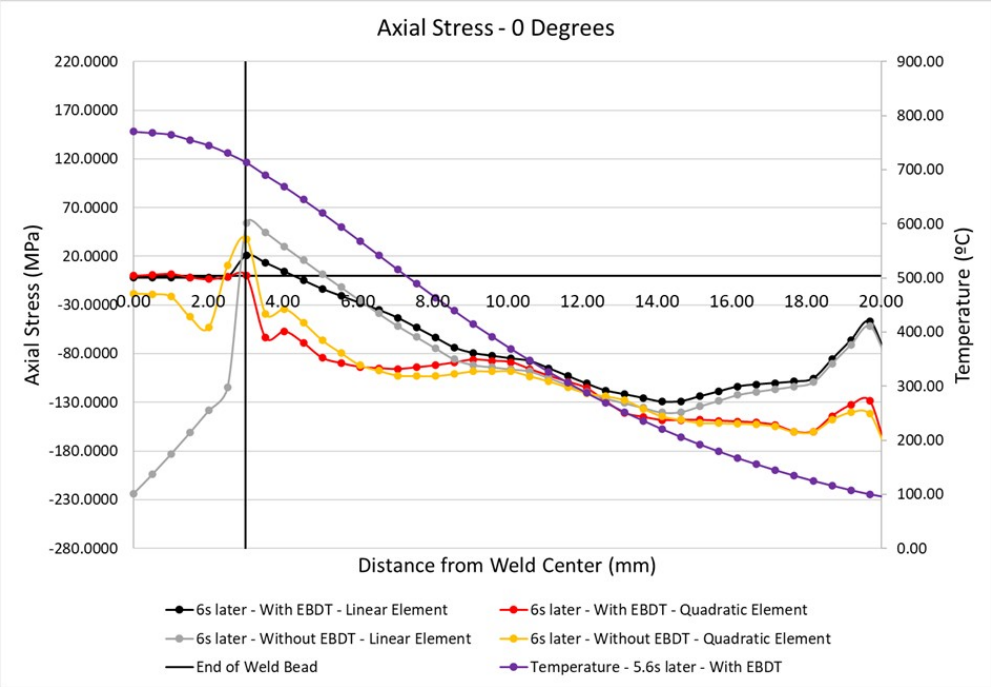

Source: Prepared by the author.

Figure 54 - Axial stresses calculated on the external surface at 0° after 24 seconds the passage of the heat source.

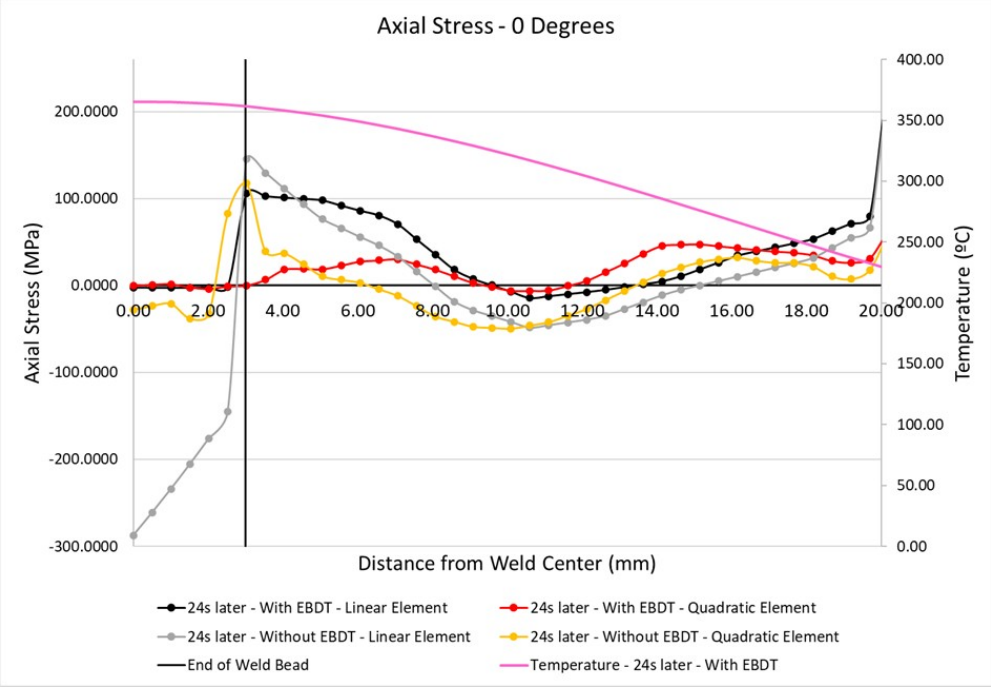

Source: Prepared by the author.

Figure 55 – Axial stresses calculated on the external surface at 0º after 60 seconds the first passage and right after the second passage of the heat source.

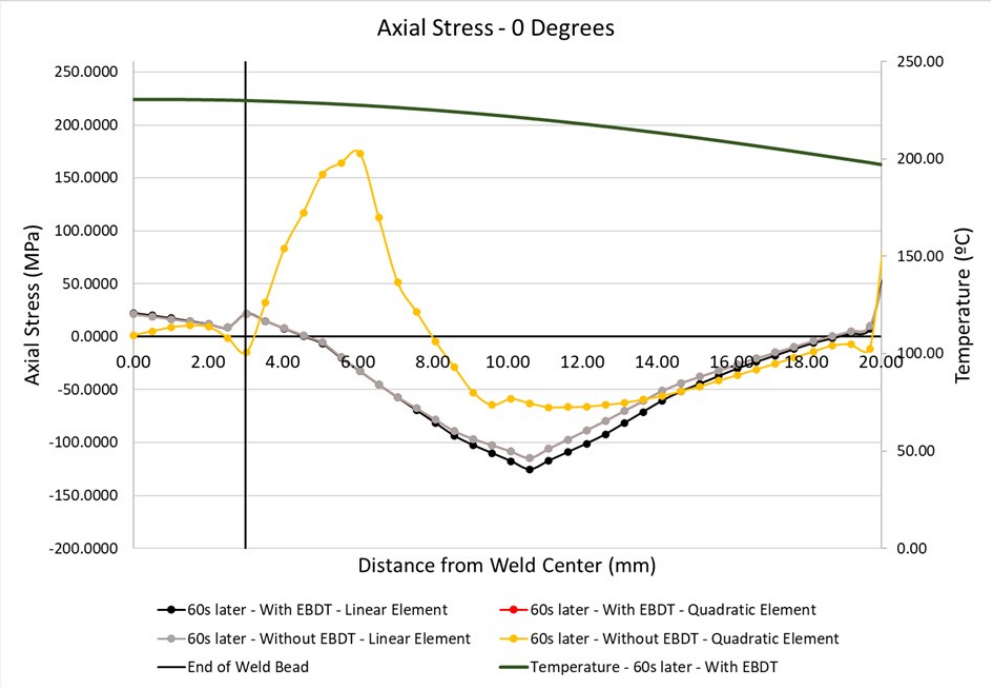

Source: Prepared by the author.

Figure 56 - Axial stresses calculated on the external surface at 0º at the end of the test (120s).

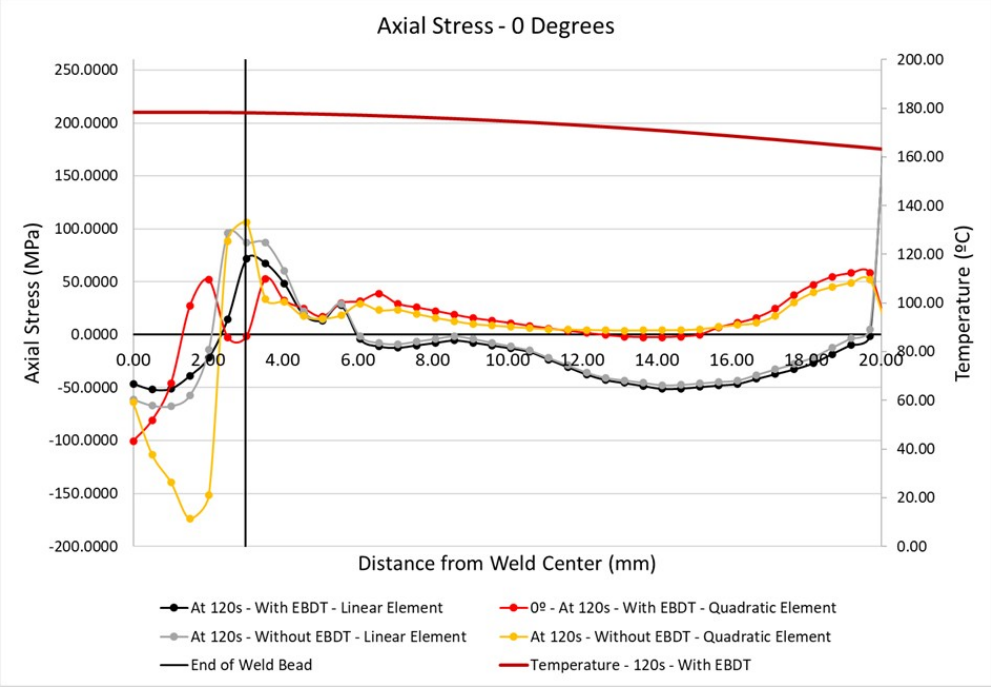

Source: Prepared by the author.

A similar distribution of residual stresses can be observed in other regions along the circumferential direction of the tube. Figure 57 presents the residual stresses obtained for different positions around the tube. Notably, only at the 0° angle, which undergoes reheating from the heat source, are lower residual stresses observed compared to other positions. Therefore, the axial distribution of tensile stresses in the weld bead region and the heat-affected zone (HAZ), particularly at the 90°, 180°, and 270° angles, is governed by the yield stress, which in turn depends on the temperature and the thermal history of the welding process.

Figure 57 – Residual stresses obtained on the external surface of the tube at 0°, 90°, 180°, and 270° positions, with EBDT and the second order elements.

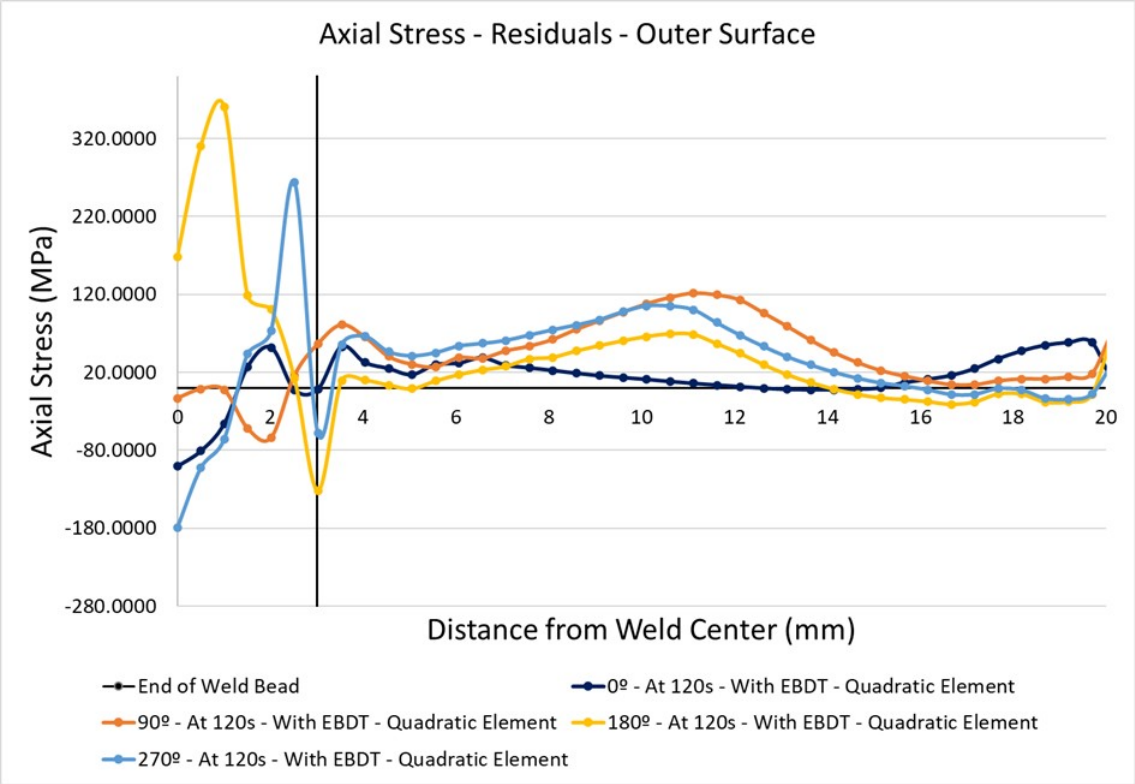

Source: Prepared by the author.

Xia (2018) conducted similar analyses on tubes composed of cast steel and hot-rolled steel tubular components, obtaining results that corroborate the findings of this study. The author emphasizes that compressive axial stresses predominate in the welded region and its vicinity, transitioning to tensile stresses at greater distances due to local bending.

Deng (2006) performed an analysis on a SUS304 stainless steel tube with thinner walls and greater length, and his results also align with the present study. According to Deng, the axial stresses obtained at the 0° angle differ when compared to other regions, highlighting a relatively homogeneous stress distribution across most of the tube's circumferential profile.

4.2.2.3 Computational analysis of the conducted tests

After discussing the results obtained from the thermomechanical analysis, it is crucial also to evaluate the computational times required for executing all tests, as one of the primary challenges in computational simulations is the execution time demanded by the tests.

Initially, Table 4 presents the computational times for the thermal and mechanical analyses using linear order elements, with variations in the application of the element birth and death technique (EBDT). An increase of approximately 16.5% in the total test time is observed when EBDT is employed, comprising a 20% increase in the thermal analysis time and a 13% increase in the mechanical analysis time.

Table 4 – Thermomechanical tests varying only the application of the element birth and death technique.

Analysis Type	Mesh Element Order	With EBDT	Without EBDT	Increase (in %)
Thermal	Linear Element (h)	17.5	14.6	**19.8%**
Mechanical	Linear Element (h)	15.2	13.4	**13.0%**
	Total (in hours)	**32.7**	**28.1**	**16.5%**

Source: Prepared by the author.

In Table 5, the computational times for the following tests were analyzed: thermal analysis using linear order elements and mechanical analysis with quadratic order elements. For this scenario, the structural analysis showed a smaller increase of approximately 6% when the EBDT was applied. Despite using a coarser mesh for quadratic order elements, similar results were achieved with reduced computational effort.

Table 5 – Thermomechanical tests varying the application of the element order mesh and element birth and death technique.

Analysis Type	Mesh Element Order	With EBDT	Without EBDT	Increase (in %)
Thermal	Linear Element (h)	17.5	14.6	**19.8%**
Mechanical	Quadratic Element (h)	8.0	7.5	**6.2%**
	Total (in hours)	**25.5**	**22.2**	**15.1%**

Source: Prepared by the author.

Assessing the computational time in the mechanical analysis for the configuration with EBDT and comparing linear and quadratic order elements, a reduction of approximately 90% in the structural testing time is observed for the quadratic order elements mesh, decreasing from 15.2 hours to 8 hours. This reduction is primarily attributed to the influence of a coarser mesh in the weld bead and heat-affected zone (HAZ), with additional nodes between the vertices of each element, compared to a more refined mesh in the same region.

Finally, a similar analysis was conducted to evaluate the variation in element order mesh in the structural analysis without applying the EBDT. As shown in Table 4 and Table 5, there is also a significant 78% increase in the execution time of the mechanical test when a more refined linear element mesh is used, decreasing from 13.4 hours to 7.5 hours, despite the absence of element addition during the heat source passage.

Therefore, based on the results presented, it is evident that the choice of element order mesh has a significant impact on the computational times of thermomechanical analyses. The use of linear elements, even in more refined meshes, leads to a substantial increase in execution time, as demonstrated by an approximate 90% increase in the analysis with the Element Birth and Death Technique (EBDT) and a 78% increase in the analysis without EBDT.

This increase is attributed to the higher density of elements and the refinement required in the heat-affected zone (HAZ) and the weld bead, which demand more computational resources. On the other hand, meshes with quadratic elements, even at lower densities, can achieve satisfactory results with less impact on computational times, proving to be an efficient alternative for optimizing the balance between accuracy and computational cost. It is important to note that for meshes with linear elements, a total of 73,058 elements were used, whereas for quadratic-order elements, only 11,355 elements were utilized, representing a reduction of approximately 85% in the total number of elements while maintaining results similar to those of a more refined mesh.

Thus, the choice between linear and quadratic order elements must be carefully evaluated, considering the type of analysis, the available computational resources, and the level of detail required in the model.

5 CONCLUSIONS

This study presented a detailed analysis of the thermomechanical behavior in the arc welding process using the Finite Element Method (FEM) in ANSYS software, with emphasis on the application of the Element Birth and Death Technique (EBDT). Additionally, the variation in the order of mesh elements for structural analysis was addressed. The primary objective was to investigate how these variables influence temperature distributions, residual stresses, displacements, and the computational times required for efficient simulations.

The results demonstrated that the choice of element order mesh has a direct and significant impact on both the accuracy and computational performance of the analyses. Quadratic-order elements proved to be particularly efficient, achieving precise results with lower mesh density and substantially reducing processing times. Moreover, the application of the Element Birth and Death Technique provided a more realistic representation of material behavior during welding, from the point of view of material insertion during the test, especially in modeling the progressive addition of material to the weld bead and the heat-affected zone (HAZ). As for the test data, more tests should be carried out, including experimental tests, to validate the results obtained.

The results also demonstrated that the use of the Element Birth and Death Technique (EBDT) led to an approximate 16.5% increase in the total test duration, with a 20% increase in the thermal analysis time and a 13% increase in the mechanical analysis time. Overall, the results were similar for both the thermal and mechanical parts, with a noticeable difference during the heat source passage. Under this condition, there was a temperature difference of approximately 315°C (ranging from 665°C with EBDT to 348°C without EBDT). Additionally, the high thermal gradient in the weld bead region caused discrepancies in axial stresses within the same area when comparing cases with and without EBDT, as observed in the analysis at 150° from the start of the weld bead application. Thus, if the focus of the analysis is on the thermal and mechanical behavior in the heat-affected zone (HAZ), performing the test without EBDT may suffice. However, if the focus is on analyzing the weld bead, additional tests should be conducted to validate this technique.

Although single-pass welding was the focus of this study in both cases (metallic plate and tube), the results suggest that the reheating of adjacent regions caused by the heat source passage induces stress redistributions, which may be more pronounced in multi-pass welding. These observations highlight the importance of studying multi-pass welding, where

the accumulation of residual stresses and thermomechanical interactions between passes can lead to significantly different outcomes.

Additionally, the results demonstrate that the choice of element order mesh significantly influences the computational time of thermomechanical analysis. Linear elements, even in refined meshes, substantially increase execution time, with an approximately 90% rise in the analysis using EBDT and 78% without EBDT. This increase is primarily due to the higher element density and refinement required in the heat-affected zone (HAZ) and weld bead, which demand greater computational resources.

Conversely, quadratic elements offer a more efficient alternative, achieving comparable accuracy with considerably fewer elements and reduced computational cost. In this study, an 85% reduction in the total number of elements was achieved while maintaining results similar to those of a more refined mesh. These findings highlight the advantage of using quadratic elements to optimize the balance between accuracy and computational efficiency in thermomechanical simulations.

Finally, this study contributes not only to the understanding of the thermomechanical phenomena involved in the welding process but also to the advancement of simulation techniques. It demonstrates that combining the Element Birth and Death Technique with quadratic elements can provide an optimized balance between accuracy and computational cost. The results presented here validate the methodology and open avenues for future investigations, both academic and industrial, particularly in manufacturing processes.

5.1 Future work

Based on the limitations and findings of this study, several opportunities for further research have been identified to enhance the understanding of thermomechanical behavior in welding processes. The main suggestions for future work include:

- Expanding the study to analyze thermomechanical behavior in multi-pass welding, considering the cumulative effects of residual stresses, deformations, and thermal variations;
- Conducting a detailed investigation of the impact of reheating previously welded regions in multi-pass processes;
- Broadening the scope of simulations to include other metallic materials, such as aluminum alloys, titanium, and stainless steels – especially

austenitic stainless-steel alloys with a face-centered cubic (FCC) crystal structure - and examining the effects of different thermal and mechanical properties on the welding process. Additionally, analyzing various weld bead geometries and component shapes to understand variations in thermal and structural behavior;

- Performing physical experiments to validate the results of computational simulations;
- Investigating the impact of repetitive thermal cycles in multi-pass welding, focusing on how continuous heat exposure affects the microstructure and mechanical properties of the material, especially in the heat-affected zone (HAZ);
- Incorporating fracture and fatigue prediction models in welding analyses to evaluate the service life of welded components under varying load conditions and operational environments, with an emphasis on industrial applications.

REFERENCES

ANSYS Inc. **Academic Research Mechanical**. Versão 18.1. [S. l.]: ANSYS Inc., 2017.

ANSYS Inc. **ANSYS 12.0 reference manual**. Canonsburg, PA: ANSYS Inc., 2009.

ANSYS Inc. **Chapter 8: Element Birth and Death**. 2024. Disponível em: https://ansyshelp.ansys.com/public/account/secured?returnurl=/Views/Secured/corp/v242/en/ans_adv/Hlp_G_ADV6.html?q=element%20birth%20and%20death. Acesso em: 12 dez. 2024.

ANSYS Inc. **Element Order**. 2024. Disponível em: https://ansyshelp.ansys.com/public/account/secured?returnurl=/Views/Secured/corp/v242/en/wb_msh/ds_solid_element_midside_nodes.html?q=element%20order. Acesso em: 12 dez. 2024.

ANSYS Inc. **Structures with material nonlinearities**. 2024. Disponível em: https://ansyshelp.ansys.com/public/account/secured?returnurl=/Views/Secured/corp/v242/en/ans_thry/thymatlnonlin.html?q=Structures%20with%20Material%20Nonlinearities. Acesso em: 12 dez. 2024.

BRACARENSE, Alexandre Queiroz. **Gas Metal Arc Welding**. 2003. Disponível em: https://infosolda.com.br/wp-content/uploads/Downloads/Artigos/processos_solda/gas-metal-arc-welding.pdf. Acesso em: 20 nov. 2023.

CHEN, Bai-Qiao. **Prediction of Heating Induced Temperature Fields and Distortions in Steel Plates**. 2011. 75 f. Dissertação (Mestrado em Engenharia) – Universidade Técnica de Lisboa, Lisboa, 2011.

CHEN, B. Q.; ADAK, M.; SOARES, C. Guedes. Thermo-Mechanical Analysis Of The Effects Of Weld Parameters In Ship Plates During Welding Process. **ICSOT**: Technological Innovations in Shipbuilding, v. 8, n. 9, p. 23-30, 2011.

CHO, Dae-Won *et al.* Molten pool behavior in the tandem submerged arc welding process. **Journal of Materials Processing Technology**, Amsterdã, v. 214, n. 11, p. 2233-2247, nov. 2014. Disponível em: https://doi.org/10.1016/j.jmatprotec.2014.04.032. Acesso em: 20 nov. 2023.

DEBROY, T.; DAVID, S. A. Physical processes in fusion welding. **Reviews of Modern Physics**, College Park, v. 67, n. 1, p. 85-112, 1 jan. 1995. Disponível em: https://doi.org/10.1103/revmodphys.67.85. Acesso em: 20 nov. 2024.

DENG, Dean; MURAKAWA, Hidekazu. Numerical simulation of temperature field and residual stress in multi-pass welds in stainless steel pipe and comparison with experimental measurements. **Computational Materials Science**, Amsterdã, v. 37, n. 3, p. 269-277, set. 2006. Disponível em: https://doi.org/10.1016/j.commatsci.2005.07.007. Acesso em: 12 nov. 2024.

DURGUTLU, Ahmet. Experimental investigation of the effect of hydrogen in argon as a shielding gas on TIG welding of austenitic stainless steel. **Materials & Design**, Amsterdã, v. 25, n. 1, p. 19-23, fev. 2004. Disponível em: https://doi.org/10.1016/j.matdes.2003.07.004. Acesso em: 10 nov. 2024.

EREN, Ilker; TOLUN, Fatmagul. Evaluation the effect of welding residual stress to structural properties of vehicle chassis frame. **TTEM: Technics Technologies Education Management**, Sarajevo, v. 9, n. 2, p. 265-270, 2014. Disponível em: https://ttem.ba/2014/06/01/volume-9-number-2. Acesso em: 15 dez. 2024.

FACHINOTTI, Víctor D.; ANCA, Andrés Amílcar; CARDONA, Alberto. Analytical solutions of the thermal field induced by moving double-ellipsoidal and double-elliptical heat sources in a semi-infinite body. **International Journal for Numerical Methods in Biomedical Engineering**, Chichester, v. 27, n. 4, p. 595-607, 24 mar. 2011. Disponível em: https://doi.org/10.1002/cnm.1324. Acesso em: 11 out. 2023.

FALLAHI, A.; JAFARPUR, K.; NAMI, M. R. An investigation of the effect of coolants on residual stresses in weldments based on entropy generation. *In:* 18th Annual International Conference on Mechanical Engineering, ISME, 2010, Teerã, Irã. *Anais...* Teerã: ISME, 2010. p. 1-6. Disponível em: https://doi.org/10.13140/2.1.1329.4729. Acesso em: 17 dez. 2024.

FARIAS, R. M.; TEIXEIRA, P. R. F.; VILARINHO, L. O. Variable profile heat source models for numerical simulations of arc welding processes. **International Journal of Thermal Sciences**, Amsterdã, v. 179, p. 107593, set. 2022. Disponível em: https://doi.org/10.1016/j.ijthermalsci.2022.107593. Acesso em: 20 mar. 2024.

FLINT, T. F. *et al.* Extension of the double-ellipsoidal heat source model to narrow-groove and keyhole weld configurations. **Journal of Materials Processing Technology**, Amsterdã, v. 246, p. 123-135, ago. 2017. Disponível em: https://doi.org/10.1016/j.jmatprotec.2017.02.002. Acesso em: 25 out. 2024.

FRIEDMAN, E. Analysis of weld puddle distortion and its effect on penetration. **Welding journal**, Miami, v. 57, n. 6, p. 161, 1978.

GANESH, K. C. *et al.* Thermo-mechanical Analysis of TIG Welding of AISI 316LN Stainless Steel. **Materials and Manufacturing Processes**, Londres, v. 29, n. 8, p. 903-909, 18 jul. 2014. Disponível em: https://doi.org/10.1080/10426914.2013.872266. Acesso em: 25 jul. 2024.

GOLDAK, John; CHAKRAVARTI, Aditya; BIBBY, Malcolm. A new finite element model for welding heat sources. **Metallurgical Transactions B**, Nova York, v. 15, n. 2, p. 299-305, jun. 1984. Disponível em: https://doi.org/10.1007/bf02667333. Acesso em: 26 mar. 2024.

HIBBELER, Russell Charles. **Mechanics of Materials**. 8. ed. Boston: Pearson Prentice Hall, 2010. 885 p. ISBN 0-13-602230-8.

JEYAPRAKASH, N.; HAILE, Adisu; ARUNPRASATH, M. The parameters and equipments used in TIG welding: A review. **The International Journal of Engineering and Science (IJES)**, Irbid, v. 4, n. 2, p. 11-20, 2015. Disponível em: https://www.theijes.com/papers/v4-i2/Version-2/C042011020.pdf. Acesso em: 15 dez. 2024.

JIANG, Ping *et al.* Optimization of laser welding process parameters of stainless steel 316L using FEM, Kriging and NSGA-II. **Advances in Engineering Software**, Amsterdã, v. 99, p. 147-160, set. 2016. Disponível em: https://doi.org/10.1016/j.advengsoft.2016.06.006. Acesso em: 07 set. 2024.

KAH, P.; MARTIKAINEN, J. Influence of shielding gases in the welding of metals. **The International Journal of Advanced Manufacturing Technology**, Londres, v. 64, n. 9-12, p. 1411-1421, 12 abr. 2012. Disponível em: https://doi.org/10.1007/s00170-012-4111-6. Acesso em: 03 mar. 2024.

KALITA, Kanak *et al.* Finite Element Modelling, Predictive Modelling and Optimization of Metal Inert Gas, Tungsten Inert Gas and Friction Stir Welding Processes: A Comprehensive Review. **Archives of Computational Methods in Engineering**, Barcelona, 10 ago. 2022. Disponível em: https://doi.org/10.1007/s11831-022-09797-6. Acesso em: 28 jan. 2025.

KARLSSON, R. I.; JOSEFSON, B. L. Three-Dimensional Finite Element Analysis of Temperatures and Stresses in a Single-Pass Butt-Welded Pipe. **Journal of Pressure Vessel Technology**, Nova York, v. 112, n. 1, p. 76-84, 1 fev. 1990. Disponível em: https://doi.org/10.1115/1.2928591. Acesso em: 01 dez. 2023.

KARPAGARAJ, A.; SIVA SHANMUGAM, N.; SANKARANARAYANASAMY, K. Some studies on mechanical properties and microstructural characterization of automated TIG welding of thin commercially pure titanium sheets. **Materials Science and Engineering**: A, Amsterdã, v. 640, p. 180-189, jul. 2015. Disponível em: https://doi.org/10.1016/j.msea.2015.05.056. Acesso em: 12 out. 2024.

KEIVANI, R. *et al.* Predicting residual stresses and distortion during multisequence welding of large size structures using FEM. **The International Journal of Advanced Manufacturing Technology**, Londres, v. 73, n. 1-4, p. 409-419, 22 abr. 2014. Disponível em: https://doi.org/10.1007/s00170-014-5833-4. Acesso em: 15 set. 2024.

KHARE, Sumit; MITTAL, N. D. Three-Dimensional Free Vibration Analysis of Thick Laminated Composite Circular Plates with Simply-Supported Boundary Conditions. **Materials Today: Proceedings**, Amsterdã, v. 4, n. 9, p. 10054-10061, 2017. Disponível em: https://doi.org/10.1016/j.matpr.2017.06.320. Acesso em: 15 nov. 2024.

KIK, Tomasz. Heat Source Models in Numerical Simulations of Laser Welding. **Materials**, Basel, v. 13, n. 11, p. 2653, 10 jun. 2020. Disponível em: https://doi.org/10.3390/ma13112653. Acesso em: 16 ago. 2024.

KIM, Nam-Ho. **Introduction to Nonlinear Finite Element Analysis**. New York, NY: Springer US, 2015. *E-book*. ISBN 9781441917454. Disponível em: https://doi.org/10.1007/978-1-4419-1746-1. Acesso em: 03 dez. 2023.

KOHNKE, Peter. **ANSYS Theory Reference**: Release 5.6. 11. ed. Canonsburg: ANSYS Inc., 1999. 1286 p.

KOU, Sindo; SUN, D. K. Fluid flow and weld penetration in stationary arc welds. **Metallurgical Transactions A**, Nova York, v. 16, n. 1, p. 203-213, jan. 1985. Disponível em: https://doi.org/10.1007/bf02815302. Acesso em: 20 mar. 2025.

KRISHNA, D. Venkata et al. Numerical analysis on the effect of welding parameters in TIG welding for INCONEL 625 alloy. **International Journal of Engineering and Techniques**, Chennai, v. 2, n. 5, p. 39-46, set.-out. 2016. Disponível em: https://oaji.net/articles/2017/1992-1514563168.pdf. Acesso em: 15 dez. 2024.

KUMAR, Kamlesh *et al.* A review on TIG welding technology variants and its effect on weld geometry. **Materials Today: Proceedings**, Amsterdã, v. 50, part. 5, p. 999-1004, jul. 2021. Disponível em: https://doi.org/10.1016/j.matpr.2021.07.308. Acesso em: 12 fev. 2024.

LI, Qiaochu; CHEN, Junhua. Research On Effect Factors Of Mechanical Response Of Pe Gas Pipeline In Karst Area Based On Element Birth And Death Technique. **Journal of Pressure Vessel Technology**, Nova York, p. 1-21, 20 jul. 2023. Disponível em: https://doi.org/10.1115/1.4062972. Acesso em: 10 abr. 2024.

LIMA, Arthur V. N. A.; MARCONDES, Francisco; SOUSA, José R. de. Simulação numérica do comportamento térmico na soldagem TIG em aços inoxidáveis austeníticos utilizando o EbFVM. *In*: CONGRESSO BRASILEIRO EM ENGENHARIA E CIÊNCIAS DE MATERIAIS, 2022, Águas de Lindoia. **Congresso Brasileiro em Engenharia e Ciências de Materiais**. Águas de Lindoia: Associação Brasileira de Polímeros, 2022. p. 1-6. Disponível em: https://www.metallum.com.br/24cbecimat/anais/PDF/IIIs40-003.pdf. Acesso em: 14 set. 2024.

MANURUNG, Yupiter H. P. *et al.* Welding distortion analysis of multipass joint combination with different sequences using 3D FEM and experiment. **International Journal of Pressure Vessels and Piping**, Amsterdã, v. 111-112, p. 89-98, nov. 2013. Disponível em: https://doi.org/10.1016/j.ijpvp.2013.05.002. Acesso em: 08 mai. 2024.

MARQUES, Eva S. V.; SILVA, Francisco J. G.; PEREIRA, António B. Comparison of Finite Element Methods in Fusion Welding Processes—A Review. **Metals**, Basel, v. 10, n. 1, p. 75, 2 jan. 2020. Disponível em: https://doi.org/10.3390/met10010075. Acesso em: 15 set. 2024.

MOAVENI, Saeed. **Finite Element Analysis**: Theory and Application with ANSYS. [*S. l.*]: Prentice Hall, 1999. *E-book* (512 p.). ISBN 9780137850983. Disponível em: http://ftp.demec.ufpr.br/disciplinas/TM738/Livros/Finite%20Element%20Analysis,%20Theory%20and%20application%20with%20ANSYS,%20.pdf. Acesso em: 12 dez. 2024.

MODENESI, Paulo J.; APOLINÁRIO, Eustáquio R.; PEREIRA, Iaci M. TIG welding with single-component fluxes. **Journal of Materials Processing Technology**, Amsterdã, v. 99, n. 1-3, p. 260-265, mar. 2000. Disponível em: https://doi.org/10.1016/s0924-0136(99)00435-5. Acesso em: 02 mar. 2024.

MODENESI, P. J. **Descontinuidades e inspeção em juntas soldadas**. Belo Horizonte: Universidade Federal de Minas Gerais, 2001.

MODENESI, Paulo J.. **Introdução à Física do Arco Elétrico**: Soldagem I. Belo Horizonte: Universidade Federal de Minas Gerais, 2012. 41 p.

MVOLA, Belinga; KAH, Paul. Effects of shielding gas control: welded joint properties in GMAW process optimization. **The International Journal of Advanced Manufacturing Technology**, Londres, v. 88, n. 9-12, p. 2369-2387, 1 jun. 2016. Disponível em: https://doi.org/10.1007/s00170-016-8936-2. Acesso em: 07 fev. 2024.

NEZAMDOST, M. R. *et al.* Investigation of temperature and residual stresses field of submerged arc welding by finite element method and experiments. **The International Journal of Advanced Manufacturing Technology**, Londres, v. 87, n. 1-4, p. 615-624, 27 fev. 2016. Disponível em: https://doi.org/10.1007/s00170-016-8509-4. Acesso em: 09 nov. 2024.

OLSON, D. L. *et al.* **ASM Handbook Volume 6**: Welding, Brazing, and Soldering. 6. ed. [*S. l.*]: ASM International, 1993. 1299 p. ISBN 978-0-87170-382-8.

PANWISAWAS, Chinnapat *et al.* Modelling of thermal fluid dynamics for fusion welding. **Journal of Materials Processing Technology**, Amsterdã, v. 252, p. 176-182, fev. 2018. Disponível em: https://doi.org/10.1016/j.jmatprotec.2017.09.019. Acesso em: 01 set. 2024.

PERIC, Djordje; SOUZA NETO, Eduardo A. de; OWEN, David R. J. **Computational Methods for Plasticity**: Theory and Applications. [*S. l.*]: Wiley & Sons, Incorporated, John, 2011. 814 p. ISBN 9781119964537.

ROBERTS, I. A. *et al.* A three-dimensional finite element analysis of the temperature field during laser melting of metal powders in additive layer manufacturing. **International Journal of Machine Tools and Manufacture**, Amsterdã, v. 49, n. 12-13, p. 916-923, out. 2009. Disponível em: https://doi.org/10.1016/j.ijmachtools.2009.07.004. Acesso em: 02 jul. 2024.

ROCHA, José Renê de Sousa. **Thermomechanical analisys of in-service welding pipelines using the element-based finite volume method**. 2022. 158 p. Tese (Doutorado em Engenharia Mecânica) – Universidade Federal do Ceará, Fortaleza, 2022. Disponível em: http://www.repositorio.ufc.br/handle/riufc/70575. Acesso em: 2 nov. 2023.

ROSENTHAL, Daniel. Mathematical theory of heat distribution during welding and cutting. **Welding journal**, Miami, v. 20, n. 5, p. 220s-234s, 1941.

ROSENTHAL, D. The Theory of Moving Sources of Heat and Its Application to Metal Treatments. **Journal of Fluids Engineering**, Nova York, v. 68, n. 8, p. 849-865, 1 nov. 1946. Disponível em: https://doi.org/10.1115/1.4018624. Acesso em: 15 jan. 2024.

SCHWEDERSKY, Mateus Barancelli et al. Soldagem TIG de elevada produtividade: influência dos gases de proteção na velocidade limite para formação de defeitos. **Soldagem & Inspeção**, Belo Horizonte, v. 16, p. 333-340, 2011. Disponível em: https://doi.org/10.1590/S0104-92242011000400004. Acesso em: 15 dez. 2024.

TCHUINDJANG, Jérôme Tchoufang *et al.* A New Concept for Modeling Phase Transformations in Ti6Al4V Alloy Manufactured by Directed Energy Deposition. **Materials**, Basel, v. 14, n. 11, p. 2985, 31 maio 2021. Disponível em: https://doi.org/10.3390/ma14112985. Acesso em: 24 nov. 2024.

TESFAYE, Fasil Kebede; GETANEH, Ayitenew Mogninet. The Grey-Based Taguchi Method was used to enhance the TIG-MIG hybrid welding process parameters for mild steel. **Invention Disclosure**, Amsterdã, p. 100016, out. 2023. Disponível em: https://doi.org/10.1016/j.inv.2023.100016. Acesso em: 20 nov. 2024.

TÜMER, M.; SCHNEIDER-BRÖSKAMP, C.; ENZINGER, N. Fusion welding of ultra-high strength structural steels – A review. **Journal of Manufacturing Processes**, Amsterdã, v. 82, p. 203-229, out. 2022. Disponível em: https://doi.org/10.1016/j.jmapro.2022.07.049. Acesso em: 20 abr. 2024.

VEMANABOINA, Harinadh; AKELLA, Suresh; BUDDU, Ramesh Kumar. Welding Process Simulation Model for Temperature and Residual Stress Analysis. **Procedia Materials Science**, Amsterdã, v. 6, p. 1539-1546, 2014. Disponível em: https://doi.org/10.1016/j.mspro.2014.07.135. Acesso em: 23 mar. 2024.

VERSTEEG, H.; MALALASEKRA, W. **Introduction to Computational Fluid Dynamics, an**: The Finite Volume Method. [*S. l.*]: Pearson Education, Limited, 2007. 520 p. ISBN 9781281156792.

WU, C. S. *et al.* Plasma arc welding: Process, sensing, control and modeling. **Journal of Manufacturing Processes**, Amsterdã, v. 16, n. 1, p. 74-85, jan. 2014. Disponível em: https://doi.org/10.1016/j.jmapro.2013.06.004. Acesso em: 03 jun. 2024.

XIA, Jie; JIN, Hui. Analysis of residual stresses and variation mechanism in dissimilar girth welded joints between tubular structures and steel castings. **International Journal of Pressure Vessels and Piping**, Amsterdã, v. 165, p. 104-113, ago. 2018. Disponível em: https://doi.org/10.1016/j.ijpvp.2018.06.003. Acesso em: 14 mar. 2024.

YAN, Jun; GAO, Ming; ZENG, Xiaoyan. Study on microstructure and mechanical properties of 304 stainless steel joints by TIG, laser and laser-TIG hybrid welding. **Optics and Lasers in Engineering**, Amsterdã, v. 48, n. 4, p. 512-517, abr. 2010. Disponível em: https://doi.org/10.1016/j.optlaseng.2009.08.009. Acesso em: 02 abr. 2024.

APPENDIX A – ALGORITHM FOR GOLDAK DOUBLE-ELLIPSOIDAL HEAT SOURCE IN PLATES

```
CMSEL, ALL,
*GET, EMAX, ELEM, NUM, MAX
*GET, EMIN, ELEM, NUM, MIN
ALLSEL
AUTOTS, ON

TIME_WELD=20
DT=0.05
A = 0.010
B = 0.002
C1 = 0.015
C2 = 0.015
FF = 1
FR = 1

Q=5083
VEL=0.005
TAU=(C1/VEL)

TIME_STEP=TIME_WELD/DT

NROPT, FULL

*DO, i,1, TIME_STEP,1
WTIME=(i*DT)
TIME, WTIME

HCENTER=VEL*WTIME

*DO, jj, EMIN, EMAX, 1

X = CENTRX(jj)
Y = CENTRY(jj)
Z = CENTRZ(jj)

CSI=Y+VEL*(TAU-WTIME)

*IF, Y, GT, HCENTER, THEN

C=C1
F=FF

*ELSE

C=C2
F=FR
```

```
*ENDIF

PART1=(6*(3**0.5)*Q*F) / (A*B*C*3.14*(3.14**0.5))
PART2=(EXP(-3*(X/A)**2)) * (EXP(-3*(Z/B)**2)) * (EXP(-3*((CSI/C)**2)))
QF=PART1*PART2
BFE, jj, HGEN,, QF

*ENDDO
SOLVE
*ENDDO

CMSEL, ALL
BFEDELE, ALL, ALL
ALLSEL
```

APPENDIX B – ALGORITHM FOR GOLDAK'S DOUBLE-ELLIPSOIDAL HEAT SOURCE IN CYLINDRICAL TUBES

```
Q = 3780*0.9
pi=3.141592654

Velocidade de soldagem em m/s

VEL=0.006

Ângulo do cordão de solda

alfa = 0

Posição da solda no início do cordão

dx = 0
dy = 0.05715
dz = 0

Raio de soldagem

R = 0.05715

Sempre observar os eixos de movimento da solda

a = 0.0035 !0.00447 !sqrt(0.008) !largura
b = 0.006 !sqrt(0.008)/2 ! profundidade
c = 0.005 !2*sqrt(0.008) !comprimento 2*largura

time_weld=120

CMSEL,S,load
*GET,EMAX,ELEM,,NUM,MAX
*GET,EMIN,ELEM,,NUM,MIN
ALLSEL

ENORM,
NEQIT,26
!AUTOTS,ON
!DELTIM,0.01,0.01,120,ON

time_inc=0.1
time_step=time_weld/time_inc
!NROPT,FULL

*DO,i,1,time_step,1
        WTIME=(i*time_inc)
        TIME,WTIME
```

```
*DO,jj,EMIN,EMAX,1
        X=CENTRX(jj)
        Y=CENTRY(jj)
        Z=CENTRZ(jj)

        beta=(VEL*WTIME)/R

        x1 = X - dx
        y1 = Y - dy
        z1 = Z - dz

        x2 = -(x1 + R*sin(beta))
        y2 = -(y1 + R*(1-cos(beta)))
        z2 = z1

        Linha 1 - Matriz de Rotação 1
        a11 = cos(beta)
        a12 = sin(beta)
        a13 = 0

        Linha 2 - Matriz de Rotação 1
        a21 = -sin(beta)
        a22 = cos(beta)
        a23 = 0

        Linha 3 - Matriz de Rotação 1
        a31 = 0
        a32 = 0
        a33 = 1

        Multiplicação

        x3 = a11*x2 + a12*y2 + a13*z2
        y3 = a21*x2 + a22*y2 + a23*z2
        z3 = a31*x2 + a32*y2 + a33*z2

        t1 = Q*6*sqrt(3)
        t2 = (a*b*c*pi*sqrt(pi))
        t3 = exp(-3*(x3**2/c**2))
        t4 = exp(-3*(y3**2/b**2))
        t5 = exp(-3*(z3**2/a**2))

        QLB = (t1/t2)*t3*t4*t5

        QLB2 = (t1/t2)*exp(-3)

        *IF,WTIME,GT,60,THEN
                QLB = 0
        *ENDIF
```

```
            *IF,QLB,GE,QLB2,THEN
                EALIVE,JJ
            *ENDIF

            BFE,jj,HGEN,,QLB

        *ENDDO

        SOLVE

*ENDDO
```

APPENDIX C – TEMPERATURE PROFILES OF THE TUBE'S EXTERNAL SURFACE AT VARIOUS ANGLES

Figure 58 - Temperature profiles of the tube's external surface at various angles.

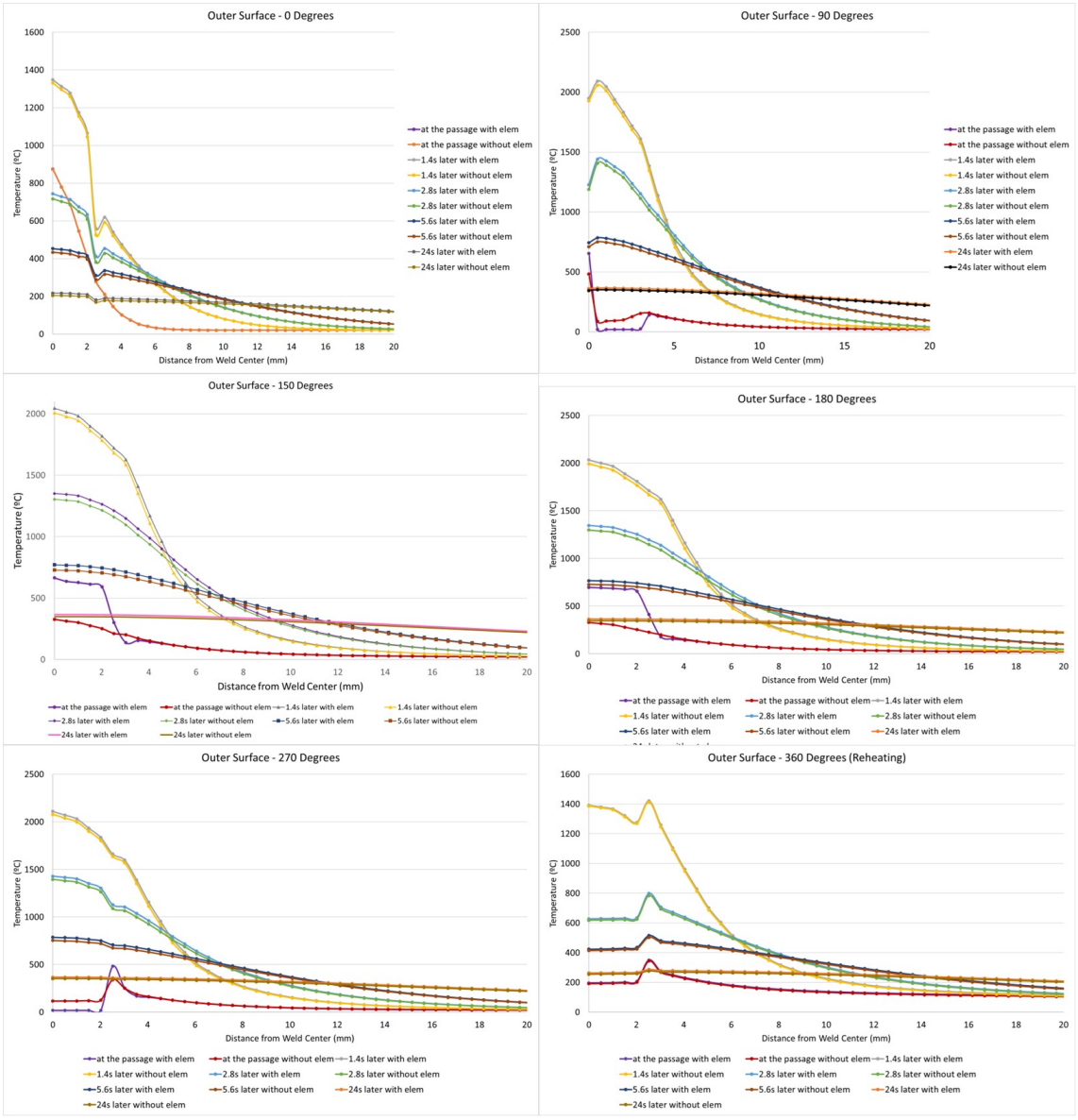

Source: Prepared by the author.